A model system for carbohydrates interactions on single-crystalline Ru surfaces

Dissertation

zur Erlangung des naturwissenschaftlichen Doktorgrades

der Julius - Maximilians - Universität Würzburg

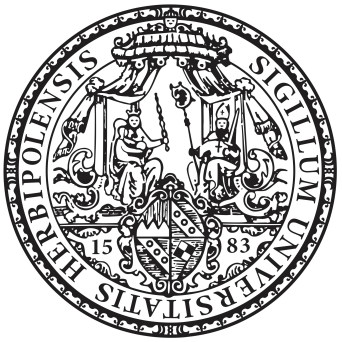

Vorgelegt von

Thanh Nam NGUYEN

Aus Thanhhoa, Vietnam

Würzburg, 2015

Eingereicht am: .....
bei der Fakultät für Physik und Astronomie

1. Gutachter: .....
2. Gutachter: .....
3. Gutachter: .....
der Dissertation

Vorsitzende(r).....

1. Prüfer:.....
2. Prüfer:.....
3. Prüfer:.....
im Promotionskolloquiums

Tag des Promotionskolloquiums: .....
Doktorurkunde ausgehändigt am:.....

"Learning to be, learning to live together, learning to know and learning to do"

UNESCO

Abstract

In this thesis, I present a model system for carbohydrate interactions with single-crystalline Ru surfaces. Geometric and electronic properties of copper phthalocyanine (CuPc) on top of graphene on hexagonal Ru(0001), rectangular Ru(10$\bar{1}$0) and vicinal Ru(1,1,$\bar{2}$,10) surfaces have been studied. First, the Fermi surfaces and band structures of the three Ru surfaces were investigated by high-resolution angle-resolved photoemission spectroscopy. The experimental data and theoretical calculations allow to derive detailed information about the momentum-resolved electronic structure. The results can be used as a reference to understand the chemical and catalytic properties of Ru surfaces. Second, graphene layers were prepared on the three different Ru surfaces. Using low-energy electron diffraction and scanning tunneling microscopy, it was found that graphene can be grown in well-ordered structures on all three surfaces, hexagonal Ru(0001), rectangular Ru(10$\bar{1}$0) and vicinal Ru(1,1,$\bar{2}$,10), although they have different surface symmetries. Evidence for a strong interaction between graphene and Ru surfaces is a 1.3–1.7 eV increase in the graphene π-bands binding energy with respect to free-standing graphene sheets. This energy variation is due to the hybridization between the graphene π bands and the Ru 4*d* electrons, while the lattice mismatch does not play an important role in the bonding between graphene and Ru surfaces. Finally, the geometric and electronic structures of CuPc on Ru(10$\bar{1}$0), graphene/Ru(10$\bar{1}$0), and graphene/Ru(0001) have been studied in detail. CuPc molecules can be grown well-ordered on Ru(10$\bar{1}$0) but not on Ru(0001). The growth of CuPc on graphene/Ru(10$\bar{1}$0) and Ru(0001) is dominated by the Moiré pattern of graphene. CuPc molecules form well-ordered structures with rectangular unit cells on graphene/Ru(10$\bar{1}$0) and Ru(0001). The distance of adjacent CuPc molecules is 15 $\pm$ 0.5 Å and 13 $\pm$ 0.5 Å on graphene/Ru(0001) and 15.4 $\pm$ 0.5 Å and 13.7 $\pm$ 0.5 Å on graphene/Ru(10$\bar{1}$0). This indicates that the molecule-substrate interaction dominates over the intermolecular interaction for CuPc molecules on graphene/Ru(10$\bar{1}$0) and graphene/Ru(0001).

Zusammenfassung

In dieser Arbeit stelle ich ein Modellsystem für die Wechselwirkungen von Kohlenwasserstoffen mit ein kristallinen Rutheniumoberflächen vor. Die geometrischen und elektronischen Eigenschaften von Kupfer-Phthalocyanin (CuPc) als Deckschicht über Graphen auf hexagonalen Ru(0001)-, rechteckigen Ru(10$\bar{1}$0)- und vicinalen Ru(1,1,$\bar{2}$,10)-Oberflächen wurden untersucht. Zunächst wurden die Fermioberflächen und Bandstrukturen der drei Rutheniumoberflächen mittels hochauflösender winkelaufgelöster Photoemissionsspektroskopie ermittelt. Die experimentellen Daten und theoretischen Berechnungen erlauben es, detaillierte Informationen zur impulsaufgelösten elektronischen Struktur abzuleiten. Die Ergebnisse können als Referenz für ein besseres Verständnis der chemischen und katalytischen Eigenschaften von Rutheniumoberflächen dienen. Als nächstes wurden Graphenschichten auf den drei verschiedenen Rutheniumoberflächen hergestellt. Bei Messungen der Beugung niederenergetischer Elektronen an den Oberflächen sowie mittels Rastertunnelmikroskopie stellte sich heraus, dass Graphen hoch geordnete Strukturen auf allen drei Oberflächen, hexagonalem Ru(0001), rechteckigem Ru(10$\bar{1}$0) und vicinalem Ru(1,1,$\bar{2}$,10), bildet, obwohl diese unterschiedliche Symmetrien aufweisen. Ein Hinweis auf eine starke Wechselwirkung zwischen Graphen und den Rutheniumoberflächen ist der Anstieg der Bindungsenergie der Graphen-π-Bänder um 1.3–1.7 eV im Vergleich zu freistehenden Graphenschichten. Diese Änderung der Energie beruht auf der Hybridisierung zwischen den Graphen-π-Bändern und den 4*d*-Elektronen des Rutheniums, wohingegen der Gitterversatz keine große Rolle bei der Bindung zwischen Graphen und Rutheniumoberflächen spielt. Abschließend wurden die geometrischen und elektronischen Strukturen von CuPc auf Ru(10$\bar{1}$0), Graphen/Ru(10$\bar{1}$0) und Graphen-/Ru(0001) im Detail untersucht. CuPc-Moleküle konnten mit hoher Ordnung auf-Ru(10$\bar{1}$0) abgelagert werden, nicht jedoch auf Ru(0001). Das Wachstum von CuPc auf Graphen/Ru(10$\bar{1}$0) und Ru(0001) wird durch die Moiréstruktur des Graphens bestimmt. CuPc-Moleküle bilden hoch geordnete Strukturen mit rechteckigen Elementarzellen auf Graphen/Ru(10$\bar{1}$0) und Ru(0001). Der Abstand benachbarter CuPc-Moleküle beträgt 15 ± 0.5 Å und 13 ± 0.5 Å auf Graphen/Ru(0001) sowie 15.4 ± 0.5 Å und 13.7 ± 0.5 Å auf Graphen/Ru(10$\bar{1}$0). Dies weist darauf hin, dass die Molekül-Substrat-Wechselwirkung bei CuPc-Molekülen auf Graphen/Ru(10$\bar{1}$0) und Graphen/Ru(0001) stärker ist als die intermolekulare Wechselwirkung zwischen den CuPc-Molekülen.

Contents

Chapter 1

Introduction

The rare transition metal, Ruthenium, has attracted a lot of attention due to a wide range of possible applications, among which is the use in extreme ultraviolet lithography (EUVL), a leading candidate for next-generation lithography methods [1]. Current lithographic techniques employ wavelengths of 248 nm or 193 nm, using deep-ultraviolet light sources. EUVL uses 13.5 nm (92.5 eV) wavelength radiation and is able to produce features as small as 20 nm [2].

Since all materials absorb extreme-ultraviolet radiation it is required to use reflective optics (multilayer Mo/Si mirrors) in EUVL. The exposure tool and the associated components also must be kept under vacuum. Surface contamination by water and hydrocarbons together with the extreme-ultraviolet radiation drastically reduces the reflectivity of the mirror used in EUVL over time, thus hampering its application [3]. Ru is an excellent candidate as a capping layer for multilayer Mo/Si mirrors, because it has a high transmission coefficient at 13.5 nm (98.4 % for a 1 nm layer), high chemical resistance in many corrosive environments, and is able to form flat and dense layers (1–2 nm) [4].

Moreover, Ru(0001) has been found to be a substrate for growing graphene, a two-dimensional one-atom thick sheet of sp^2-bonded carbon atoms arranged in a honeycomb lattice with unique and fascinating properties [5–7]. It has been shown that large single-layer or bilayer epitaxial graphene sheets with a width of 500 μm can be produced on Ru(0001) [8, 9]. Graphene is air-stable, has a very high conductivity, and only adsorbs 2.3 % of the light intensity of infrared to visible light [10]. Therefore, graphene might also be used as a capping for mirrors in EUVL [11] and for transparent conductive electrodes for engineering flexible-panel displays [12].

In spite of the great potential for applications in industry, there is limited experimental insight into the detailed electronic properties of single-crystalline Ru surfaces and the

interactions of single-crystalline Ru surfaces with hydrocarbon contaminations. Therefore, it is very important to investigate in detail the electronic structure of clean Ru and hydrocarbons on Ru surfaces for a deeper understanding of the fundamental properties of the interactions of hydrocarbons with Ru surfaces.

This work focused on ideal, i.e. single-crystal, surfaces of Ru as a model system for hydrocarbon contaminations on relevant surfaces. Three differently orientated single-crystal Ru surfaces were studied: hexagonal-surface Ru(0001), rectangular-surface Ru(10$\bar{1}$0), and stepped-surface or defect-surface Ru(1,1,$\bar{2}$,10). Several groups have measured the band structure of Ru by angle-resolved photoemission spectroscopy (ARPES) [13–15], focusing only on Ru(0001) with limited resolution but not on Ru(10$\bar{1}$0) or on Ru(1,1,$\bar{2}$,10) which are similar to real surfaces for applications [16].

For hydrocarbons, graphene and copper phthalocyanine (CuPc) molecules were used. The detailed interaction mechanisms of graphene with metal surfaces was still unclear [17]. For example, an interesting question related to the interaction mechanisms of graphene with metal surfaces is the effect of the lattice mismatch on the bonding of graphene to transition metal surfaces. Copper phthalocyanine is a common organic semiconductor [18] which is investigated frequently due to a wide range of possible applications in solar cells [19], molecular optoelectronics [20, 21], and transparent-electrode applications [22, 23]. A fundamental understanding of organic semiconductors/graphene interfaces is crucial for these applications. Moreover, the interaction of Metal phthalocyanine (MePc) molecules with metal-supported graphene was also still controversial [24]. For instance, an effect of the metal atom in the MePc was not found on graphene-/Ru(0001) [25] but was found on graphene/Ni(111) [24]. In addition, depending on the metal substrate used, graphene can feature rather different geometric structures and it will be interesting to see if this affects the arrangement of adsorbed MePc molecules.

The thesis is organized as follows:

– Chapters 2 and 3 present the background theory and the experimental techniques.

– In chapters 4, 5 and 6 the main results of the thesis are given. Chapter 4 shows the detailed electronic properties of clean Ru(0001) and, for the first time, Ru(10$\bar{1}$0) and Ru(1,1,$\bar{2}$,10). These results play an important role not only in this thesis but can also be used as a reference to facilitate subsequent studies of Ru surfaces in multilayer mirrors for application in EUVL and in the catalysis of organic molecules on ruthenium.

– In chapter 5 the interactions of graphene with three different Ru surfaces are described. It is interesting to know that graphene can be grown well-ordered not only on Ru(0001) surfaces but also on the other two surfaces, Ru(10$\bar{1}$0) and Ru(1,1,$\bar{2}$,10).

– Geometric and electronic properties of CuPc on Ru surfaces and graphene/Ru surfaces are presented in chapter 6. These will lead to a better understanding of the fundamental properties of the interaction of molecules with graphene.

– Chapter 7 presents the main discussion.

– Finally, chapter 8 gives the conclusion of my thesis and a short outlook on further topics of investigation.

Chapter 2

Background theory

2.1 Elemental and molecular properties

In this section, some basic properties of ruthenium, graphene and CuPc molecules are presented. The following description can be used as a reference for subsequent studies.

2.1.1 Hexagonal surface: Ru(0001)

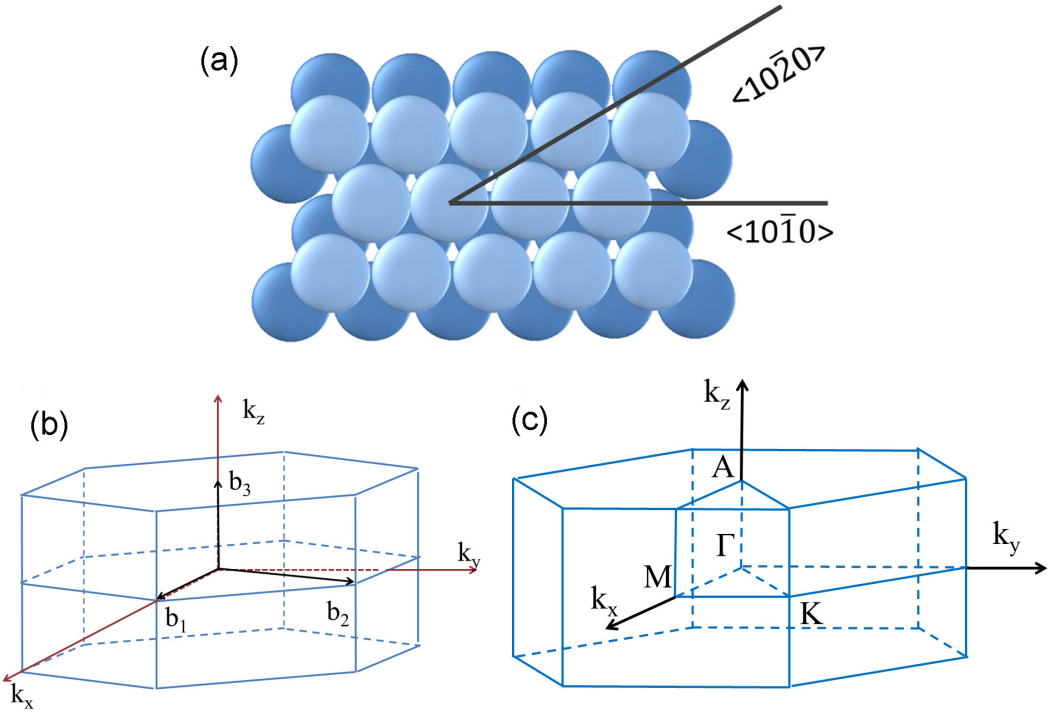

FIGURE 2.1: Ru(0001) crystal structure in real and reciprocal spaces: (a) the Ru(0001) surface in real space, (b) the reciprocal lattice of hexagonal-lattice Ru, and (c) its Brillouin zone with the critical points $\bar{\Gamma}$, $\bar{K}$ and $\bar{M}$ labeled [16].

The surface structure of Ru(0001) is hexagonally closed packed (hcp) which has the highest density of surface atoms [26]. The basic properties are:

Atomic number	44
Electronic configuration	$[Kr]4d^7 5s^1$
Lattice constant	$a_{Ru} = 2.706$ Å $c_{Ru} = 4.282$ Å
Melting point	2607 K
Work function Ru(0001)	5.52 eV [27]

Shown in Fig. 2.1 is the Ru(0001) crystal structure in real and reciprocal spaces and its Brillouin zone with the critical points $\bar{\Gamma}$, $\bar{\mathrm{K}}$ and $\bar{\mathrm{M}}$ labeled. The primitive vectors of the reciprocal lattice are:

$$\mathbf{b}_1 = \frac{4\pi}{\sqrt{3}a}\mathbf{x}, \quad \mathbf{b}_2 = \frac{2\pi}{\sqrt{3}a}\mathbf{x} + \frac{2\pi}{a}\mathbf{y}, \quad \mathbf{b}_3 = \frac{2\pi}{c}\mathbf{y} \tag{2.1}$$

and the distances between the critical points are: $\Gamma\mathrm{A} = 0.73$ Å, $\Gamma\mathrm{M} = 1.34$ Å, $\Gamma\mathrm{K} = 1.55$ Å and $\mathrm{MK} = 0.77$ Å.

2.1.2 Rectangular surface: Ru(10$\bar{1}$0)

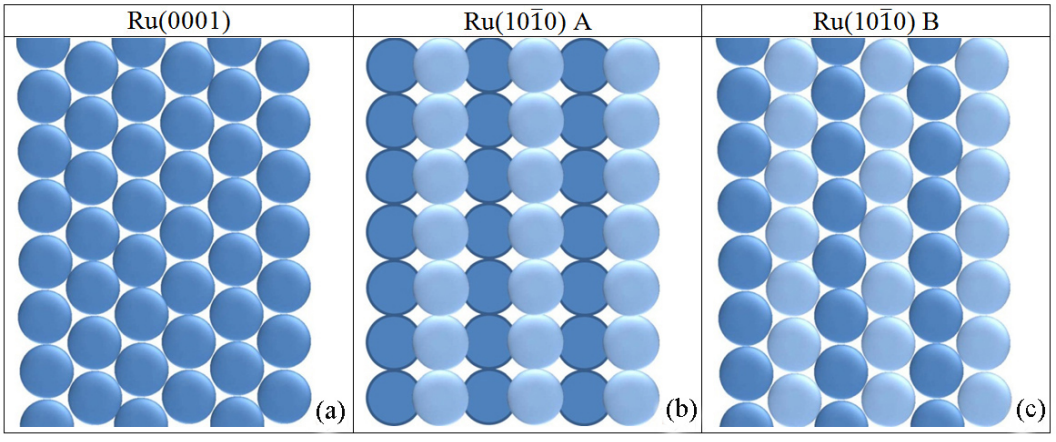

FIGURE 2.2: Atomic structures of ideal, planar hcp Ru(0001) and Ru(10$\bar{1}$0) as viewed from above (adapted from Ref. 4). (a) Ru(0001) in real space, (b) and (c) Ru(10$\bar{1}$0) in real space. Due to the ABAB... stacking sequence in the hcp structure, Ru(10$\bar{1}$0) has two different atomic arrangements which coexist.

Fig. 2.2 shows the ideal atomic structures of Ru(0001) and Ru(10$\bar{1}$0) surfaces. There are two different atomic arrangements at Ru(10$\bar{1}$0) surfaces which coexist and have the same unit-cell size due to the ABAB... stacking sequence in the hcp structure, as shown in Fig. 2.2(b) and (c) [4].

2.1.3 Vicinal surface: Ru(1,1,$\bar{2}$,10)

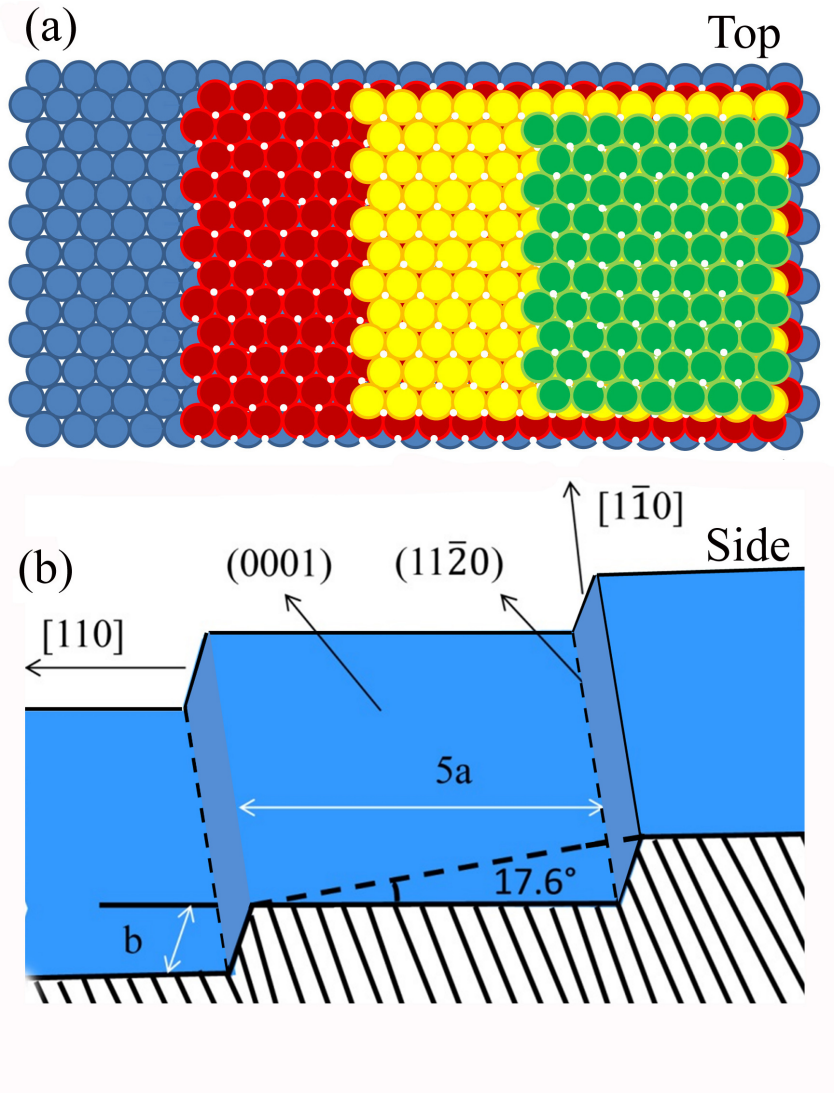

FIGURE 2.3: Atomic structures of ideal Ru(1,1,$\bar{2}$,10) as viewed from above (a) and side (b). The Ru(1,1,$\bar{2}$,10) surface has (0001) terraces which are five atoms wide and separated by (11$\bar{2}$0) steps. The angle between the vicinal and terrace surfaces is 17.6°.

Vicinal or stepped surfaces with regular step arrays have attracted much interest due to their tailored electronic properties and potential applications in electronic nanoscale devices [28]. Vicinal surfaces have an additional periodicity in one dimension, meaning that the electrons are periodically perturbed which may affect the electronic properties [29–31]. Such surfaces can be used as model systems in heterogeneous catalysis and as functional substrates for growing low-dimensional nanostructures [32, 33]. The vicinal or stepped surface Ru(1,1,$\bar{2}$,10) is slightly tilted relative to the low-index single-crystal surface Ru(0001). Fig. 2.3 shows atomic structures of ideal Ru(1,1,$\bar{2}$,10) as viewed from the top (a) and side (b). The Ru(1,1,$\bar{2}$,10) surface has (0001) terraces which are five atoms wide and separated by (11$\bar{2}$0) steps.

2.1.4 Graphene

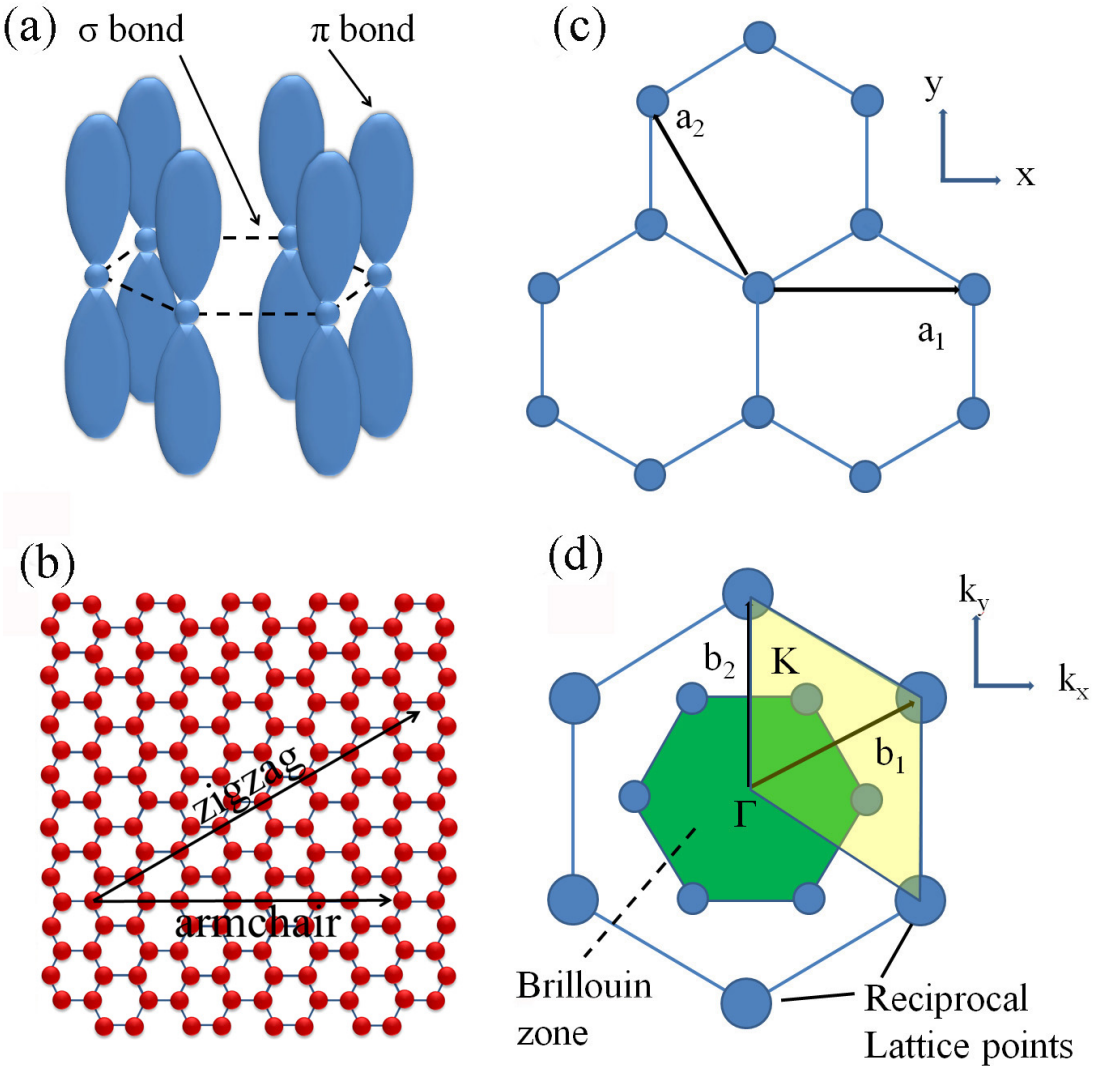

FIGURE 2.4: (a) The σ and π bonds in graphene. (b) Perspective view of a hexagonal lattice. Armchair and zigzag directions are denoted. (c) Construction of the lattice in real space. (d) The reciprocal lattice with the corresponding lattice vectors. The inner hexagon is the first Brillouin zone. The yellow parallelogram highlights a unit cell [34].

Graphene is a sheet of carbon atoms arranged in hexagonal cells only a single atom thick. Although graphene is the thinnest known material, it is stronger than diamond [34]. The basic properties are:

Atomic number	6
Electronic configuration	$1s^2 2s^2 2p^2$
Lattice constant	a = 2.464 Å
Interlayer distance	$\frac{c_{graphite}}{2}$ = 3.355 Å
C–C distance	$a_o = \frac{\sqrt{3}}{3}$a = 1.422 Å

Carbon has four valence electrons, three of which form the σ-bonds in graphene with an angle of 120° between then and defining the plane of the molecule. A schema of this hybridization is presented in Fig. 2.4(a). The two main directions in the two-dimensional lattice are called zigzag and armchair and are marked with arrows in Fig. 2.4(b). The lattice in real space is shown in Fig. 2.4(c) with the basis vectors:

$$\mathbf{a}_1 = a(1,0), \quad \mathbf{a}_2 = a(\frac{-1}{2}, \frac{\sqrt{3}}{2}) \tag{2.2}$$

In Fig. 2.4(d) the corresponding reciprocal lattice with the first Brillouin zone, the reciprocal unit cell (highlighted in yellow) and the reciprocal basis vectors is depicted.

2.1.5 Copper phthalocyanine

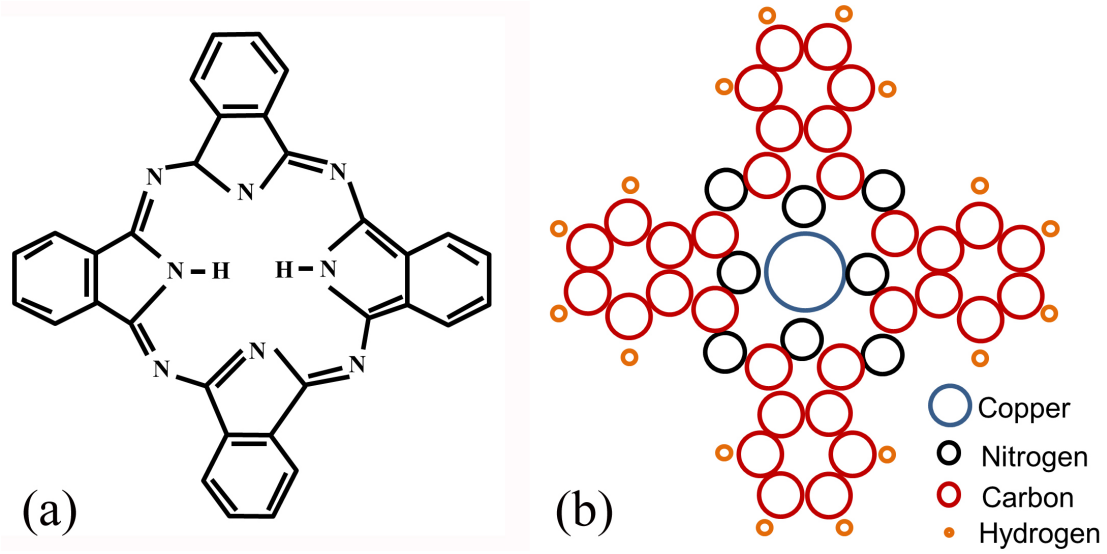

FIGURE 2.5: (a) A schematic representation of the metal-free phthalocyanine molecule and (b) the molecular structure of copper phthalocyanine (adapted from Ref. 35).

Metal phthalocyanines are common organic semiconductors which have high thermal stability, high molecular symmetry, and form crystalline solids [19]. A schematic diagram of the metal-free phthalocyanine molecule (H_2Pc) is shown in Fig. 2.5(a). A metal phthalocyanine molecule is obtained by replacing the central H atoms by a suitable metal e.g. Cu, Zn, Co, etc [36]. Copper phthalocyanine (CuPc molecular formula: $C_{32}H_{16}N_8Cu$) is a complex of copper with phthalocyanine as shown in Fig. 2.5(b) [35].

2.2 Low-energy electron diffraction

A detailed discussion of the theory can be found elsewhere [37–40]. Here, I only summarize the main points of the discussion as presented in the book of Yip-wah Chung

[37] to provide a basis for understanding the fundamental phenomena and theories of the investigations in the next chapters.

Low-energy electron diffraction has been used to investigate the periodic structure of solid surfaces [41]. According to de Broglie, the wavelength λ of an electron beam of energy $E = eU$ is given by:

$$\lambda = \frac{h}{\sqrt{2mE}} \tag{2.3}$$

where U is the accelerating voltage, h is Planck's constant, and m is the electron mass. For voltages between 20 and 600 V the wavelength is in the range of 3 to 0.5 Å which is in the order of atomic distances. Therefore, we can use low-energy electrons to obtain the two-dimensional surface structure of a sample.

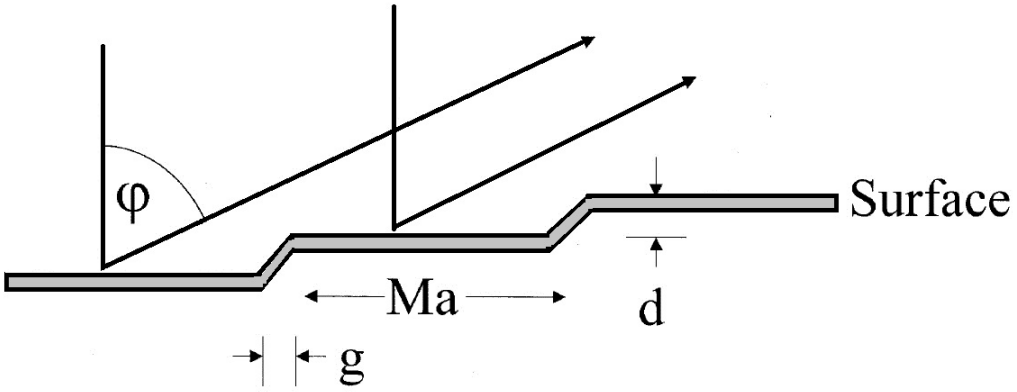

FIGURE 2.6: Diffraction at a stepped surface with the electron beam at normal incidence. The stepped surface has the lattice spacing a, the step height d, the horizontal step displacement g, and the number of atomic rows on the terrace $M + 1$

Fig. 2.6 shows the diffraction at a stepped surface with the electron beam at normal incidence. The stepped surface has the lattice spacing a, the step height d, the horizontal step displacement g, and the number of atomic rows on the terrace $M + 1$. The interference function $J(\varphi)$ at the angle φ is as follows:

$$J = \frac{\sin^2\left[\frac{M+1}{2}(ka\sin\varphi)\right]}{\sin^2\left(\frac{1}{2}(ka\sin\varphi)\right)} \times \sum_{\infty} \delta\left[\frac{1}{2}k(Ma+g)\sin\varphi + \frac{1}{2}kd(1+\cos\varphi) - m\pi\right] \tag{2.4}$$

$$J = J_o \times J_s \tag{2.5}$$

J_o is the interference function of atoms in a terrace. J_s gives rise to a splitting of the diffraction spot because it has δ functions which are zero excepting their arguments are equal to zero. The terrace width of stepped surfaces can be directly estimated by measuring the splitting. The quantitative evaluation is given by the equation:

$$\frac{\Delta K}{K_{10}} = \frac{a_o}{D} \tag{2.6}$$

where ΔK is a distance in the pattern measured in K-space, K_{10} is the distance of two normal spots in the diffraction pattern, a_o is the lattice constant of the substrate giving rise to the normal spot distance K_{10}. D is the terrace width, which correlates with the width or distance ΔK.

2.3 Scanning tunneling microscopy

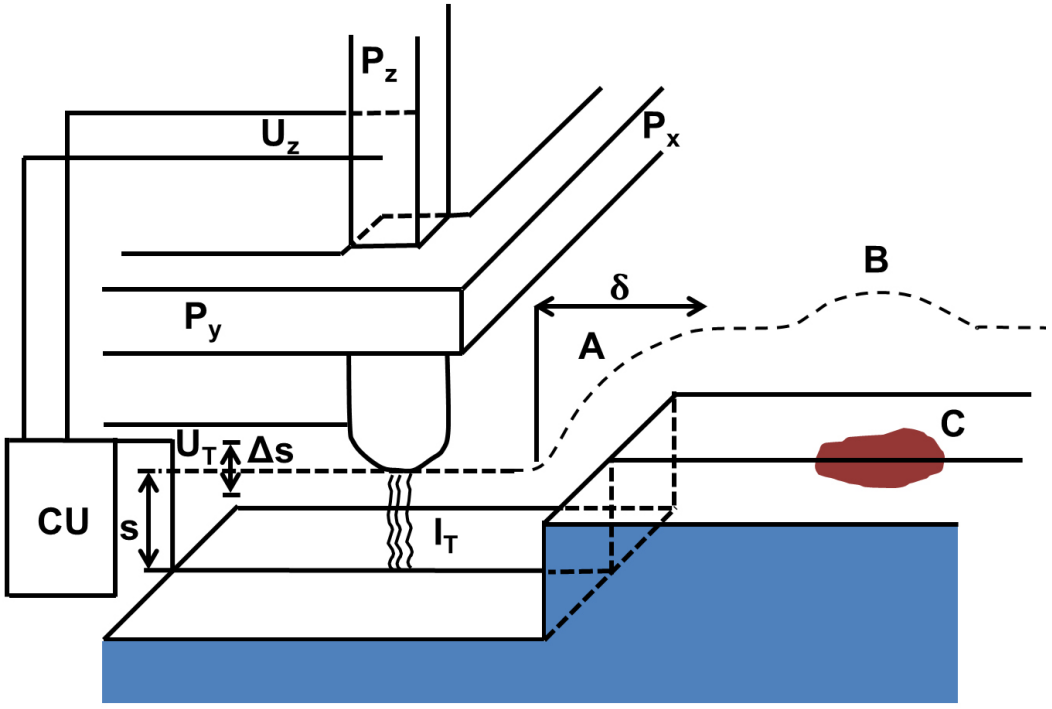

FIGURE 2.7: Principle of operation of the STM. The tunneling current I_T is kept constant while the tip is moved by three piezo drives. The appropriate voltage U_T between the tip and the sample is applied by the control unit, CU (adapted from Ref. 42).

In this section, the concepts of scanning tunneling microscopy (STM) are presented. The STM was invented in 1982 by Heinrich Rohrer and Gerd Binnig of IBM' Research Laboratory in Zürich, Switzerland [44, 45]. The principle of operation of the STM is shown in Fig. 2.7. A bias voltage is applied between the tip and the sample. A metal tip scans across a conducting surface. Due to the quantum mechanical tunneling effect a tunneling current occurs between the tip and the sample if the tip-sample surface separation is in within a few Ångström. Fig. 2.8 shows the energy level diagram of a tunneling junction. Even though the bias voltage is smaller than the energy barrier between the two metals, there is still a tunneling current. This tunneling current [42] is defined by:

$$I_T = V_T exp(A\Phi^{1/2}s) \tag{2.7}$$

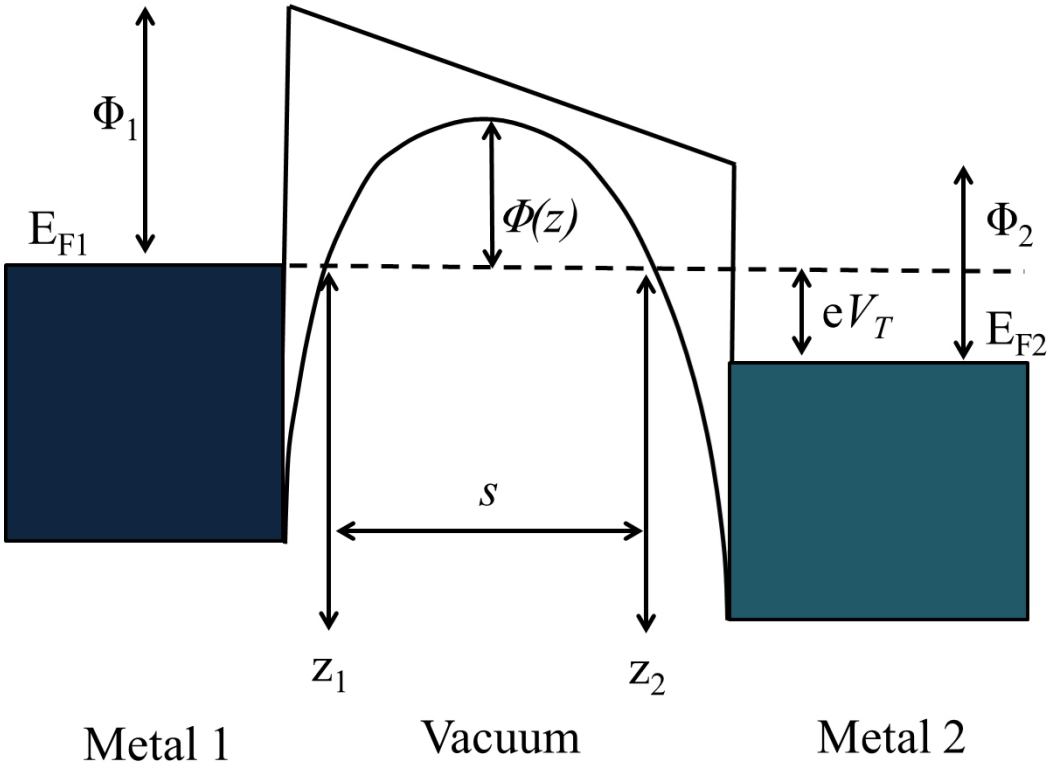

FIGURE 2.8: Energy level diagram of a tunneling junction (adapted from Ref. 43). The separation between two metals or between the tip and sample is denoted by s, V_T is the applied voltage. As a result, the Fermi levels E_F are shifted against each other by an energy eV_T.

where V_T is the bias voltage, s is the separation between the tip and sample, and A is a constant given by $A = 2((2m_2)^{1/2})/h$. There are two modes in STM measurement, the constant current mode and the constant height mode [46].

- The constant current mode can be used for large and rough samples without destroying the tip. In this mode, the current and the voltage are kept constant by adjusting the tip-surface separation. So it needs time to enable the feedback system to respond to this change and, therefore, the scan rates are comparatively low.

- With the constant height mode, the current is changed to keep the vertical position of the tip constant. The scan rates can be comparatively high which is advantageous for eliminating thermal drift but large scan sizes should be avoided to protect the tip.

2.4 Photoelectron spectroscopy

Photoelectron spectroscopy is the most important technique to measure the electronic structure of materials [47]. There is a large number of review books and papers available about photoelectron spectroscopy [47–51]. Here the basic description of photoemission is presented.

The photoelectron spectroscopy is a technique based on the photoelectric effect [48] which was first observed by Hertz in 1887 [52]. In 1905, Einstein [53] explained it as a manifestation of the quantum nature of light. Fig. 2.9 shows the energetics of the photoemission process in an ARPES experiment. As shown in Fig. 2.10, The kinetic energy and the emission angle of the electrons are collected by the detector. Using the total energy and the laws of momentum conservation, the kinetic energy of the ejected electrons escaping from the sample into the vacuum can be determined:

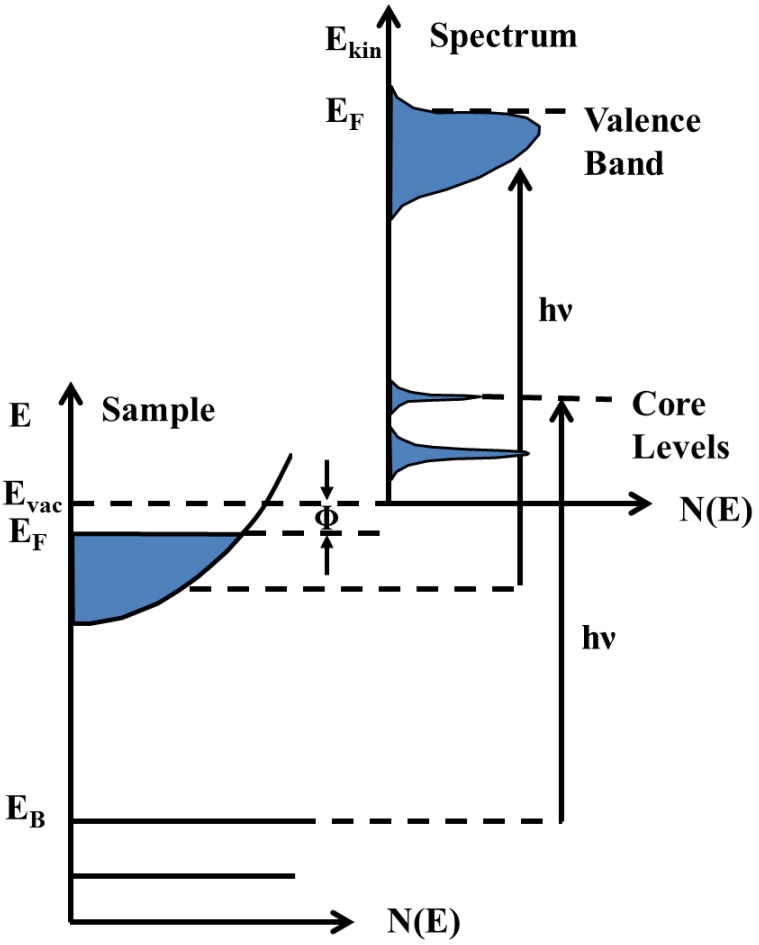

FIGURE 2.9: Energetics of the photoemission process (adapted from ref. 48). The energy of the incident photon is $h\nu$ and E_B is the binding energy of the electrons which is referred to the Fermi level in solids and to the vacuum level in free atoms or molecules.

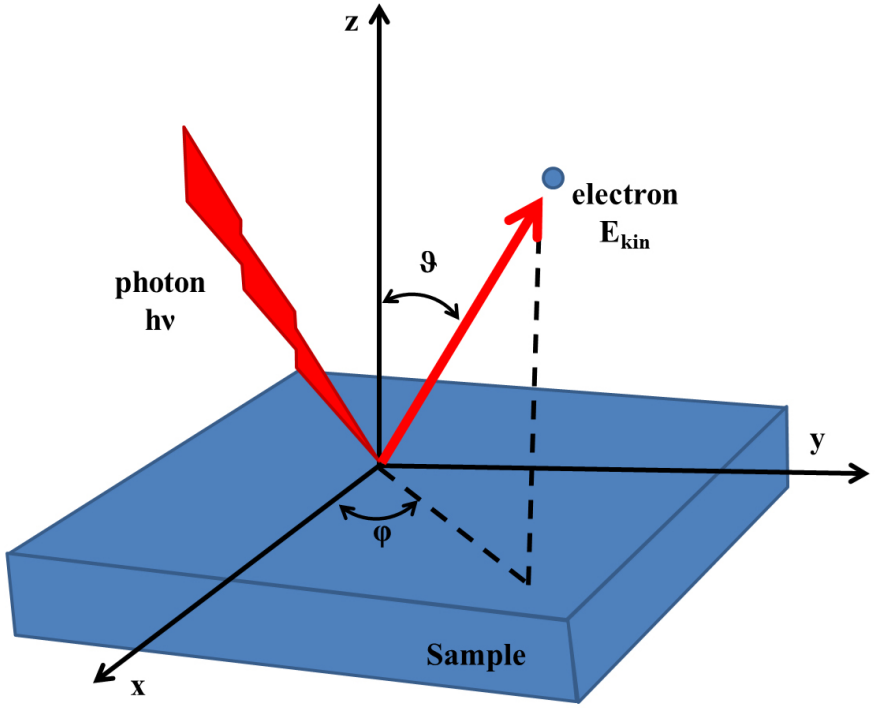

FIGURE 2.10: The geometry of an ARPES experiment in which the emission direction of the photoelectron is specified by the polar (ϑ) and azimuthal (φ) angles (adapted from Ref. 54).

$$E_{kin} = h\nu - \phi - |E_B| \tag{2.8}$$

$$\mathbf{p}_{||} = \hbar\mathbf{k}_{||} = \sqrt{2mE_{kin}} \cdot \sin\vartheta \tag{2.9}$$

The photon momentum can be neglected due to being low in ARPES experiments. In the equations, $h\nu$ is the energy of the incident photon, E_B is the binding energy which is referred to the Fermi level in solids and to the vacuum level in free atoms or molecules, $\hbar\mathbf{k}_{||}$ is the parallel electron crystal momentum in the extended zone scheme, ϕ is the work function of the material, ϑ is the polar emission angle which is shown in Fig. 2.10. From the ARPES measurement the perpendicular electron crystal momentum, $k_\perp$, cannot be determined directly. If the emitted electrons are assumed to be in a free-electron final state, the perpendicular momentum [55] is given by:

$$k_\perp = \frac{\sqrt{2m}}{\hbar}\sqrt{2mE_{kin}\cos^2\vartheta + V_0} \tag{2.10}$$

Once the value of $k_\perp$ is known it is possible to determine the value of the inner potential V_0.

Chapter 3

Experimental

This work was done in three different UHV chambers with a basis pressure as low as $1 \cdot 10^{-10}$ mbar which were denoted as chamber A, B, and C. Most of the data presented in chapter 4 was measured in chamber A which has a high-resolution photoelectron analyzer (Scienta R4000) using a monochromatized helium lamp for He I_α and He II_α radiation ($h\nu = 21.2$ eV and 40.8 eV, respectively) and a monochromatized X-ray gun. The lowest measurement temperature is about 5 K. The angle-resolved mode of the analyzer covers a parallel detection range of about $\pm 15°$ with an angular resolution of 0.5°. Additional rotation of the sample was used to allow two-dimensional k-space mapping. The total energy resolution was $\Delta E = 6$ meV, measured from the Fermi level of a polycrystalline tantalum foil in thermal and electrical contact with the sample.

UHV chamber B features a photoelectron analyzer (Scienta SES 200). It is equipped with a home-made Knudsen cell for evaporating CuPc molecules, a LEED apparatus (ErLEED) and a rotatable manipulator with liquid Helium cooling attaining a lowest measurement temperature of about 50 K. The surface structures and electronic properties of graphene and CuPc on Ru surfaces presented in chapters 5 and 6 were mostly measured in chamber B at room temperature. The angle-resolved mode of the analyzer covers a parallel detection range of about $\pm 10°$ with an angular resolution of 0.5°. The sample was rotated in steps of 2° from $-10°$ to 60° to map the band structure. The UV radiation source used in chamber B was He I_α radiation from a monochromatized helium lamp. The surface structures of the graphene and CuPc on Ru surfaces were measured with scanning tunneling microscopy (STM) in chamber C.

3.1 Clean single-crystal Ru surfaces

Clean, well-ordered ruthenium crystals (MaTeck GmbH, purity 99.99%) cut along the (0001), (10$\bar{1}$0) and (1,1,$\bar{2}$,10) planes were prepared in UHV. The cleaning procedure consisted of sputtering with Ar ions of 1 keV energy at an angle of $\pm 45°$ incidence on the surface with an ion current of about 5 μA for 60 minutes to remove carbon. If samples still contained carbon contaminations, oxygen dosing for 5 min at a pressure of $5 \cdot 10^{-7}$ mbar with the sample kept at a temperature of 1000 K was applied. The residual oxygen on the surface was desorbed at 1300 K. For annealing or heating samples to a high temperature the electron bombardment method was used with a high voltage (700–1000 V) applied between the sample and the preheated filament. The filament current was about 2–4 A. The emission current was about 50 mA. The cleanness and long-range order of the surface were verified by means of X-ray photoelectron spectroscopy (XPS), low-energy electron diffraction (LEED) and ultraviolet photoelectron spectroscopy (UPS), as described in chapter 4.

3.2 Preparation of Graphene

Graphene can be prepared on Ru surfaces by heating the sample within 90 s to around 1400 K and then slowly reducing the temperature within 10 min. Carbons from the Ru bulk segregate on the surfaces and form graphene [56]. The thickness of the graphene is checked by XPS (see chapter 4).

3.3 Preparation of CuPc

The CuPc monolayers were prepared by using organic-molecular beam deposition (OMBD). The CuPc molecules were evaporated from a Knudsen cell evaporator in UHV. The temperature used to evaporate the CuPc was 668 K. After depositing the film was annealed at 500 K to get well-defined CuPc organic films.

Chapter 4

Single-crystalline Ru surfaces*

4.1 Introduction

In order to understand the nature of the surface orbitals of clean Ru surfaces as well as their spatial orientation, it is very important to investigate in detail the electronic structure. Therefore, in this chapter experimental and theoretical investigations of the Fermi surface and the band structure of bare Ru surfaces will be reported. This work should prove useful as a reference for subsequent studies of organic molecules deposited on top of graphene on Ru surfaces.

In the literature, the band structure of Ru has been studied theoretically by several groups, such as Jepsen *et al.* [57] and Moruzzi *et al.* [58] using the linear muffin-tin-orbital model, Feibelman *et al.* [59] using self-consistent linear combinations of atomic orbitals (LCAO), Holzwarth *et al.* [60] and Chelikowsky *et al.* [61] using local-orbital ab-initio pseudopotentials, and Pelzer *et al.* [15] using relativistic Korringa-Kohn-Rostoker (KKR) methods. Overall, the calculated band structures are consistent among themselves. Feibelman *et al.* [59] showed that there is a well-defined surface state of Ru in the *s*-*d* gap at 5.3 eV below the Fermi energy at the Γ point. The existence of this surface state is also confirmed by Holzwarth *et al.* [60]. Beside that there are two other surface states, one at 1.5 eV below the Fermi energy near the Γ point, which would be difficult to detect experimentally due to small band gaps, and the other at the K point, at about 2 eV below the Fermi energy, which is expected to be more easily accessible [60]. Jepsen *et al.* [57] indicated that the spin-orbit coupling leads to a small splitting of the bands.

*Parts of this chapter were published in:
N. Nguyen, M. Mulazzi, F. Reinert, "Electronic structure and Fermi surface of Ru(0001) and Ru($10\bar{1}0$) measured with high resolution angle-resolved photoemission spectroscopy", Journal of Electron Spectroscopy and Related Phenomena, 27(7):191, 2013.

The band structure of Ru surfaces has been measured experimentally by several groups using angle-resolved photoemission spectroscopy (ARPES) [13–15]. But they focused on Ru(0001) with only limited resolution; the best resolution reported was about 350 meV [15]. There are some basic features of the electronic structure of Ru(0001) that have been detected, such as a peak within 0.5 eV below the Fermi energy representing the uppermost *d* band and a set of unresolved peaks at about 2.5 eV below the Fermi energy comprising the lower *d* and the upper *sp* bands [13]. Pelzer *et al.* [15] found that in measurements of the band structure of Ru with He I_α radiation an intense peak at 4.5 eV below the Fermi level is actually an Auger peak of 16.5 eV kinetic energy. It was not possible to observe all of the bands predicted by the theoretical calculations because of the limited energy resolution. Furthermore, so far the Fermi surface of Ruthenium has been measured only once with the ARPES method on the (0001) face [15] and once with the bulk-sensitive de Haas-van Alphen technique [57, 62]. The experimental and theoretical investigations of the Fermi surface and the band structure of Ru(0001) and, for the first time, Ru(10$\bar{1}$0) and Ru(1,1,$\bar{2}$,10) will be presented here. It was possible to observe the fine details of the Fermi surface due to the improved resolution and, thus, a quantitative comparison between the experimental and theoretical band structures was feasible. When the excitation energies were established, the band structure and Fermi surfaces were calculated for different orientations and for different values of the $k_\perp$ component of the photoelectron momentum. After detailed comparison, the experimental data and theoretical calculations were found to be in good agreement for a particular value of $k_\perp$.

4.2 Geometric properties of Ru surfaces

We can use LEED to determine the orientation and cleanness of samples. The LEED patterns presented in Fig. 4.1, of clean (a) Ru(10$\bar{1}$0), (b) Ru(0001) and (c) Ru(1,1,$\bar{2}$,10) were measured at room temperature with electron beam energies of 50 eV, 57 eV and 84 eV, respectively. We can see very sharp spots in the LEED patterns of the three Ru surfaces, indicating no contamination and high smooth surface crystallinity. Given the experimental setup, the orientation of the sample in-plane crystallographic axis is very important for the quality of the ARPES data. Therefore, I took special care to align the samples and to check them using the LEED patterns. From Fig. 4.1, the orientation of the crystal axis with respect to the detector acceptance window of the electron analyzer can be determined to be in the ΓA, ΓK and ΓK direction for (a) Ru(10$\bar{1}$0), (b) Ru(0001) and (c) Ru(1,1,$\bar{2}$,10), respectively. The misalignment of the crystal axis with respect to the detector acceptance window in Fig. 4.1(b) is about 4°. When the samples are

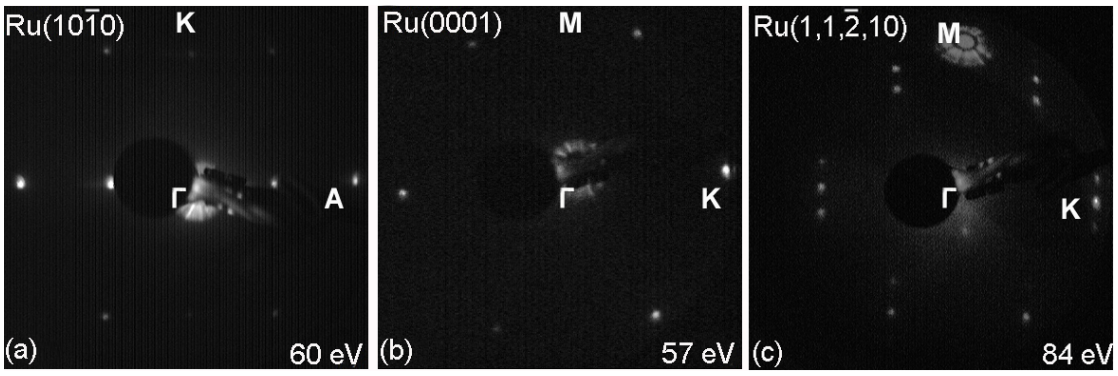

FIGURE 4.1: LEED patterns of Ru surfaces: (a) Ru(10$\bar{1}$0) recorded with electron beam energy $E_0 = 60$ eV, (b) Ru(0001) with $E_0 = 57$ eV, (c) Ru(1,1,$\bar{2}$,10) with $E_0 = 84$ eV, incidence normal to the terrace surface in all cases. LEED patterns show very sharp spots, indicating no contamination and high surface crystallinity of the three Ru surfaces. In (c), spot splitting due to regular arrays of steps can be observed. The orientation of the crystal axis with respect to the detector acceptance window of the electron analyzer is the ΓA, ΓK and ΓK direction for (a) Ru(10$\bar{1}$0), (b) Ru(0001) and (c) Ru(1,1,$\bar{2}$,10), respectively.

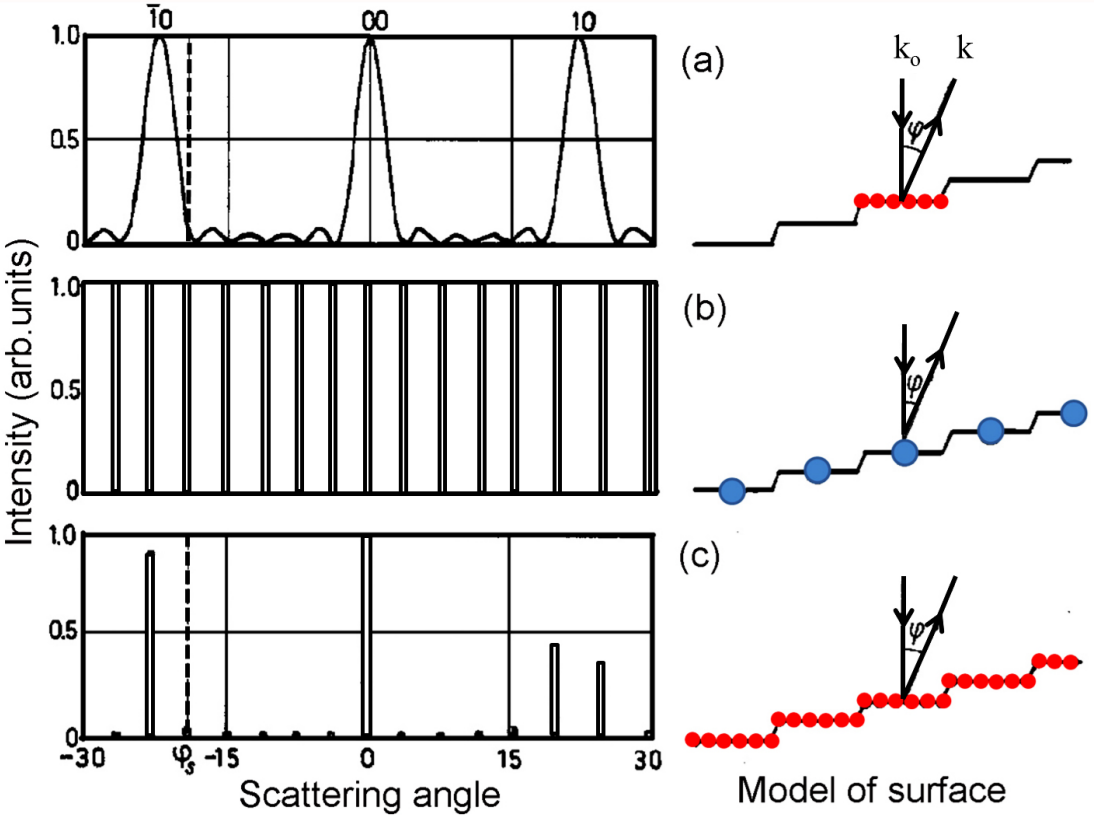

FIGURE 4.2: Diffraction profiles and atom positions for: (a) a single terrace, (b) a regular array of identical scatterers, and (c) a combination of (a) and (b) (adapted from Ref. 63). Depending on the different phases of the two diffraction functions, the spot splitting in the LEED patterns might be observable. If the two diffraction functions are in phase (the 00 beam), only single spots are present. If they are out of phase (the 10 beam), a splitting of the spots can be seen.

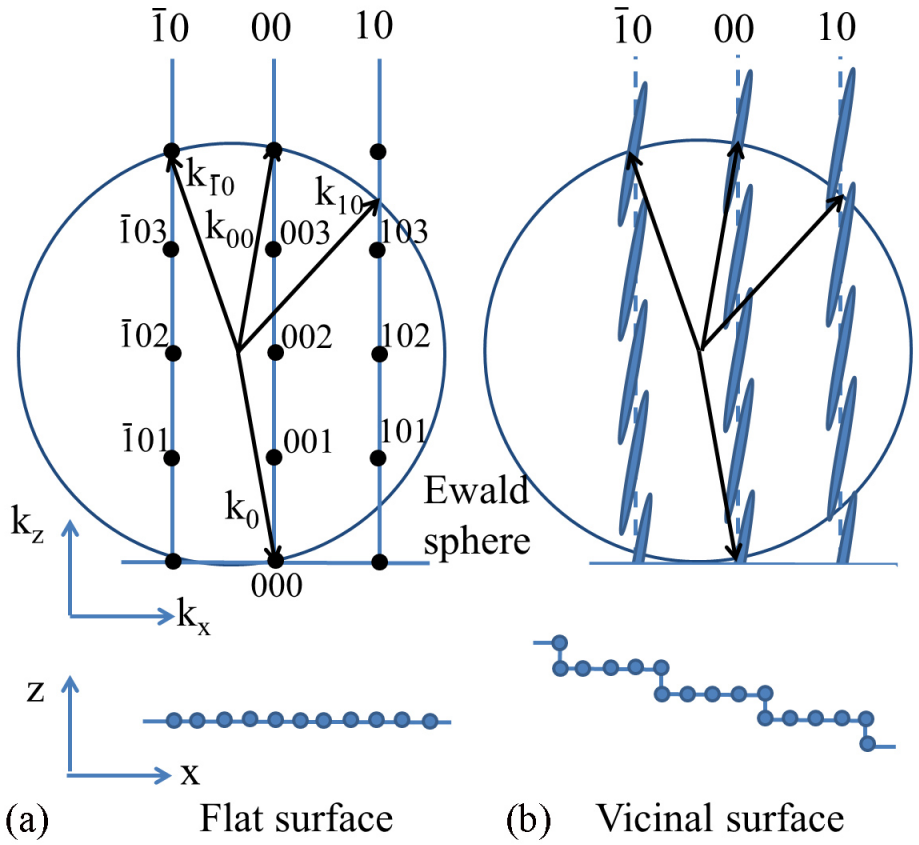

FIGURE 4.3: Ewald's construction of the LEED pattern for (a) a flat surface and (b) a vicinal surface (adapted from Ref. 63), where k_0 is the wave vector of the incident beam and k_{00}, k_{01} and $k_{\bar{1}0}$ are the wave vectors of the diffracted beams. The three-digit numbers are the three-dimensional reciprocal lattice points. See text for details.

rotated, the band structure of the Ru surface in the ΓK, ΓM and ΓM direction for (a) Ru(10$\bar{1}$0), (b) Ru(0001) and (c)Ru(1,1,$\bar{2}$,10), respectively, can be measured.

In Fig. 4.1(c), the spot splitting can be observed. This indicates that Ru(1,1,$\bar{2}$,10) has a very high surface crystallinity with large areas of regular arrays of steps. The diffraction pattern of the stepped-surface Ru(1,1,$\bar{2}$,10) is a combination of two diffraction functions, from a single terrace Fig. 4.2(a) and from a regular array of identical scatterers Fig. 4.2(b) [63]. Depending on the different phases of the two diffraction functions, the spot splitting in the LEED patterns might be observable. If the two diffraction functions are in phase (the 00 beam), only single spots are present. If they are out of phase (the 10 beam), a splitting of the spots can be seen. Fig. 4.3 presents Ewald's construction of the LEED pattern for (a) a flat surface and (b) a stepped surface (Ref. 63). Where k_0 is the wave vector of the incident beam and k_{00}, k_{01} and $k_{\bar{1}0}$ are the wave vectors of the diffracted beams. The three-digit numbers are the three-dimensional reciprocal lattice points. The reciprocal lattice points, in the reciprocal space, for a flat surface form continuous lines in the directions parallel to the surface. Therefore, the scattered beams

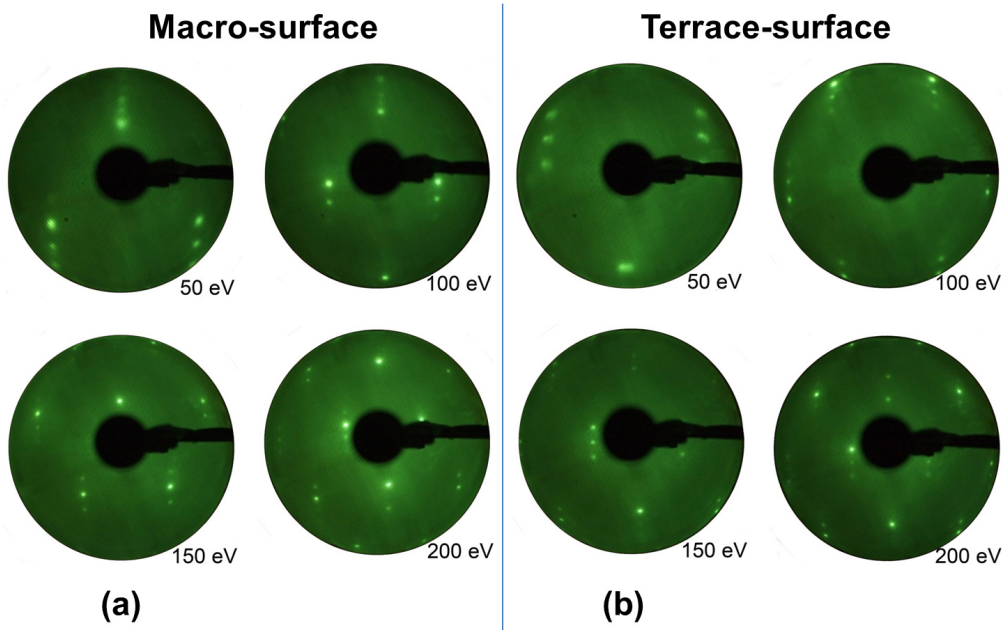

FIGURE 4.4: LEED patterns of Ru(1,1,$\bar{2}$,10) with different electron beam energy: 50 eV, 100 eV, 150 eV and 200 eV, respectively. (a) Normal incidence on the macrosurface and (b) normal incidence on the microsurface (terrace). The spot splitting is clearly visible. This indicates that the surface features very large areas of regular arrays of steps. Using the spot splitting in the LEED pattern, the terrace width and the step height of the vicinal surface can be determined.

in that direction can be observed at all voltages. In the case of the stepped surface, the reciprocal lattice consists of local sharp rods normal to the macrosurface and located at the three-dimensional reciprocal lattice points due to the structure of the flat terraces. If the Ewald construction intersects the reciprocal lattice spot, all atoms scatter in phase. In the case of e.g. the 00 beam in Fig. 4.3, we can observe sharp and single spots for both flat and stepped surfaces. On the other hand, if the Ewald construction intersects between the reciprocal lattice spots, e.g in the case of the 10 beam in Fig. 4.3, the scattering of subsequent terraces is out of phase. Therefore, we can see the splitting of the spots [63].

As shown in the previous chapter, using the spot splitting in the LEED pattern we can determine the terrace width and the step height of the vicinal surface Ru(1,1,$\bar{2}$,10). The detailed LEED patterns of Ru(1,1,$\bar{2}$,10) with different electron beam energy for normal incidence (a) on the macrosurface and (b) on the microsurface (terrace) are shown in Fig. 4.4. The angle, Θ, between the macrosurface and terrace is about $18° \pm 1°$. The the width or distance of stepped surfaces can be roughly estimated by measuring the splitting and using the Equ. 2.6. The periodicity of the step arrangement in the Ru(1,1,$\bar{2}$,10), D, is about 14.8 ± 1.1 Å. Ideal Ru(1,1,$\bar{2}$,10), therefore, has five-atom wide (0001) terraces and one-atom high steps.

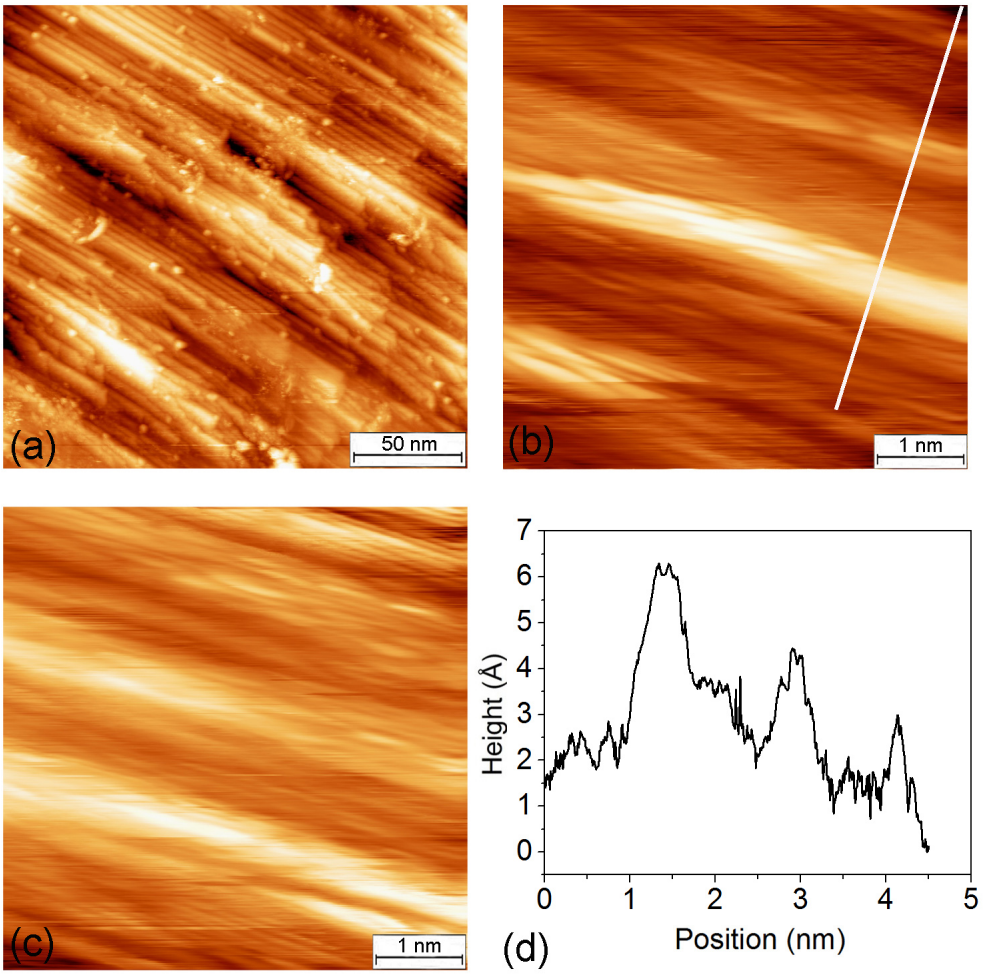

FIGURE 4.5: STM images of Ru(1,1,$\bar{2}$,10), measured at room temperature. Areas depicted are: (a) 200 nm x 200 nm, measured with $I = 1$ nA, $V_{bias} = 1$ V, (b) 20 nm x 20 nm, measured with $I = 1$ nA, $V_{bias} = 0.6$ V, and (c) 5 nm x 5 nm, measured with $I = 1$ nA, $V_{bias} = 50$ mV. (d) Height profile along the white line in (b).

The regular arrays of steps in Ru(1,1,$\bar{2}$,10) can be observed directly in the STM pictures in Fig. 4.5 with different area sizes of (a) 200 nm x 200 nm, (b) 20 nm x 20 nm and (c) 5 nm x 5 nm. The height profile along the white line in (b) is shown in (d). This confirms that the terraced surface Ru(1,1,$\bar{2}$,10) has a repetitive structure. The periodicity of the step, measured directly in the STM picture using the height profile in Fig. 4.5(d), is about 10–15 Å, which is in good agreement with the value estimated from the LEED patterns in Fig. 4.4.

4.3 Methods to determine the cleanness of Ru surfaces

The cleanness of Ru surfaces is very important because even a small amount of contamination can change the electronic properties and, therefore, the reactivity of the surface.

Normally, we use XPS to determine the cleanness of surfaces by measuring the spectra of C 1s and O 1s. Due to the overlap of the C 1s and Ru 3d peaks it is difficult to confirm the cleanness of Ru surfaces by the XPS method. In this work, I show an other method which is very easy and gives accurate results for the cleanness of Ru surfaces by using ARPES.

XPS methods: Peak ratio analysis and fit modeling

The XPS methods were used with peak ratio analysis and fit modeling to determine the cleanness of Ru surfaces. Fig. 4.6 shows XPS spectra of (a) clean Ru(10$\bar{1}$0), (b) graphene on Ru(10$\bar{1}$0) and (c) the comparison of the intensities of clean Ru(10$\bar{1}$0) and graphene/Ru(10$\bar{1}$0). The background was corrected by subtracting a Tougaard function. Shown in Fig. 4.6(a) is the XPS spectrum of clean Ru(10$\bar{1}$0) with the $3d_{5/2}$ and $3d_{3/2}$ doublet. The intensity ratio of the two lines as estimated by the occupation numbers of the emitting orbitals should be $(2 \times 5/2 + 1)/(2 \times 3/2 + 1) = 3/2$. The intensity ratio of $3d_{5/2}$ and $3d_{3/2}$ in the XPS spectrum of clean Ru(10$\bar{1}$0) is 61.3 $\pm$ 2.0 % and 38.7 $\pm$ 2.0 %, respectively. The XPS spectrum of graphene/Ru(10$\bar{1}$0) is fitted with the parameters of the clean Ru spectrum (branching ratio, energies and widths of the Ru 3d doublet peaks, and background kept fixed). There is an overlap of the C 1s and $3d_{3/2}$ peaks in the XPS spectrum. The binding energy of $3d_{5/2}$, $3d_{3/2}$ and C 1s is 280.25 eV, 284.42 eV and 284.90 eV, respectively. The intensity ratio of $3d_{5/2}$ and $3d_{3/2}$ and C 1s in the XPS spectrum of graphene/Ru(10$\bar{1}$0) is 60.8 $\pm$ 2.0 %, 38.0 $\pm$ 2.0 %, and 1.2 $\pm$ 2.0 %, respectively. Even though we chose a sample with a monolayer of carbon (3.3 Å) for analyzing, the amount of atomic carbon in the XPS spectrum is still smaller than the analysis error. Therefore, the peak ratio analysis and fit modeling cannot be used for very small quantities of carbon. The attenuation of photoelectrons originating from the Ru substrate by contaminating carbon films can still be used to determine the cleanness of Ru surfaces, as shown in Fig. 4.6(c). Assuming that the carbon film formed on the surface of Ru is smooth, continuous and uniform, the transmitted signal, I, from the substrate detected by the electron energy analyzer is given by the equation:

$$I = I_o \exp(-\frac{d_c}{\lambda(E)\cos\theta}) \tag{4.1}$$

Here, I_o is the signal of the clean Ru surface, θ is take-off angle of the photoelectrons, $\lambda(E) = 2.36$ nm is the effective attenuation length (EAL) of electrons in the carbon film [64]. The thickness of the carbon overlayer can be quantified be the equation:

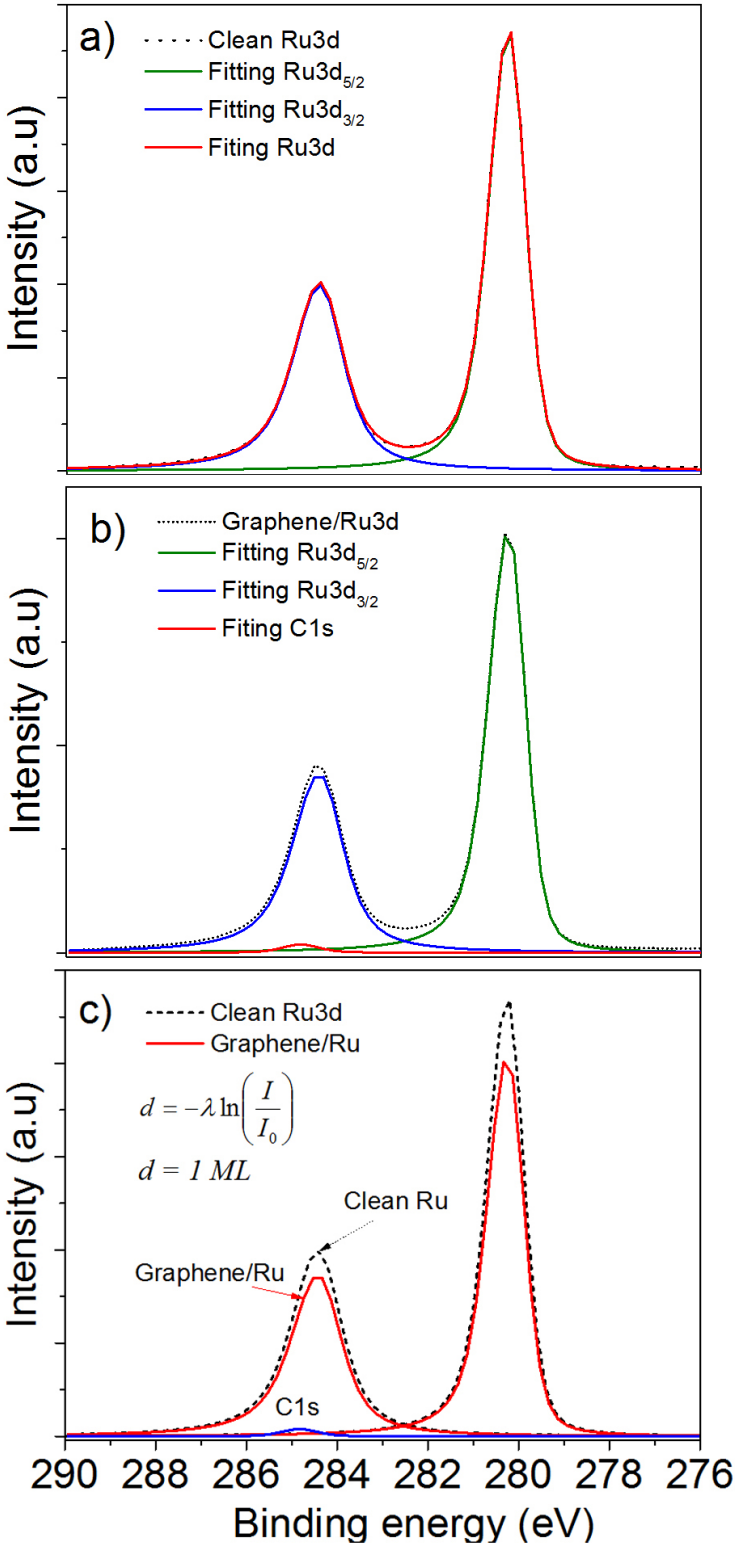

FIGURE 4.6: XPS spectra of (a) clean Ru(10$\bar{1}$0), (b) graphene on Ru(10$\bar{1}$0), and (c) comparison of the intensities of clean Ru(10$\bar{1}$0) and graphene/Ru(10$\bar{1}$0). Spectrum (b) is fitted with the parameters of the clean Ru spectrum (a) (branching ratio, energies and widths of the Ru 3d doublet peaks, and background kept fixed).

$$d_c = -\lambda(E)\cos\theta \ln(\frac{I}{I_o}) \tag{4.2}$$

The intensity was calculated from the area below the curve. Here we only use the intensity of the $3d_{5/2}$ peak because it does not overlap with C 1s peaks. From Fig. 4.6(c), the thickness of the carbon layer was calculated to be about 3.4 Å (1 monolayer (ML) of carbon or graphene).

In conclusion, if the thickness of the carbon layer on the Ru surface is less than 3.4 Å (1 ML of graphite) it is not suitable to use the XPS method for the quantification of carbon. The XPS methods is only useful if the thickness of the carbon layer is larger than 1 ML of graphene.

ARPES methods

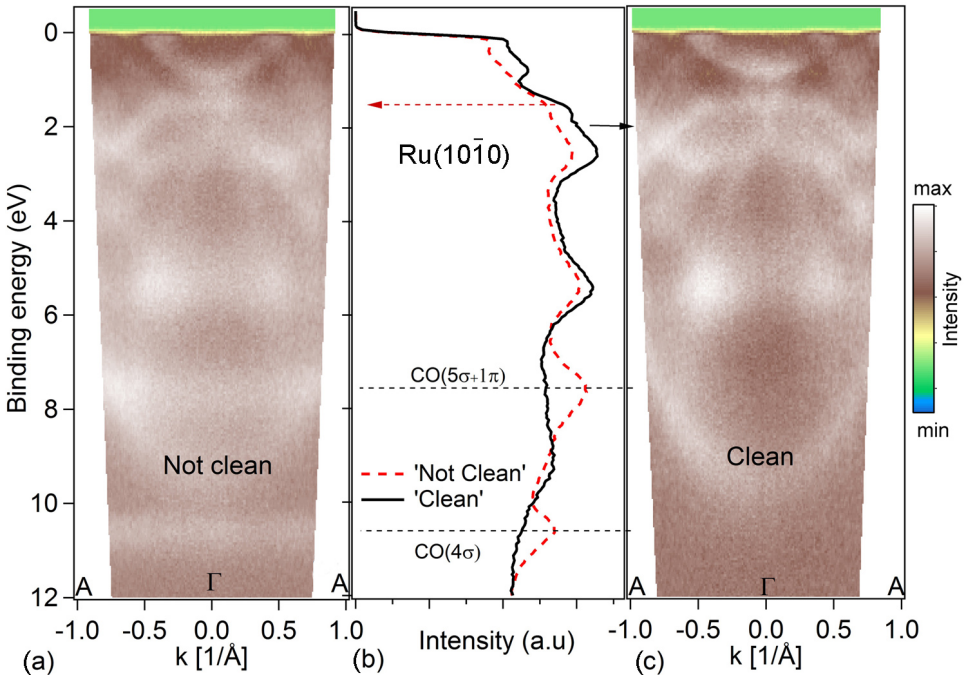

FIGURE 4.7: (a), (c) Band dispersion of the clean and not clean Ru(10$\bar{1}$0) surfaces measured at room temperature using helium II_α excitation, (b) angle-integrated valence band of the clean and not clean Ru(10$\bar{1}$0) surfaces. The black line shows the data measured on the clean surface while the red dashed line shows the Ruthenium surface contaminated with CO and Oxygen. The spectra are intensity-normalized to a common value at a binding energy of 13 eV.

Fig. 4.7 shows the band dispersions and the angle-integrated valence bands of clean and not clean Ru(10$\bar{1}$0) surfaces measured at room temperature using He II_α excitation. The effect of contamination is readily visible in the spectra in the high binding-energy (for $E_B > 4$ eV) and in the low binding-energy (for $E_B < 4$ eV) regions. In the low

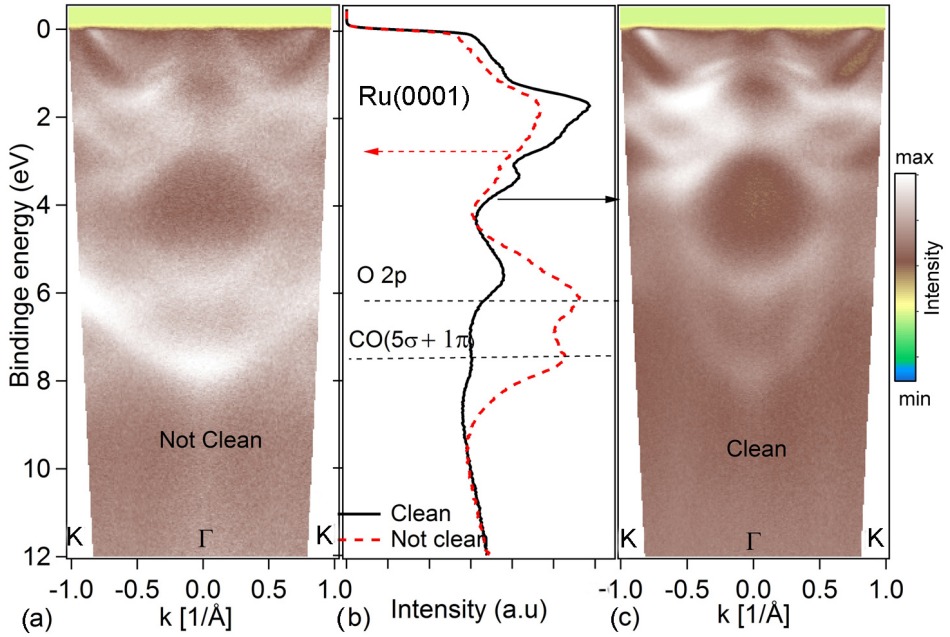

FIGURE 4.8: (a), (c) Band dispersion of the clean and not clean Ru(0001) surfaces measured at room temperature using helium II_α excitation, (b) angle-integrated valence band of the clean and not clean Ru(0001) surfaces. The black line shows the data measured on the clean surface while the red dashed line shows that of the Ruthenium surface contaminated with CO and Oxygen. The spectra are intensity-normalized to a common value at a binding energy of 13 eV.

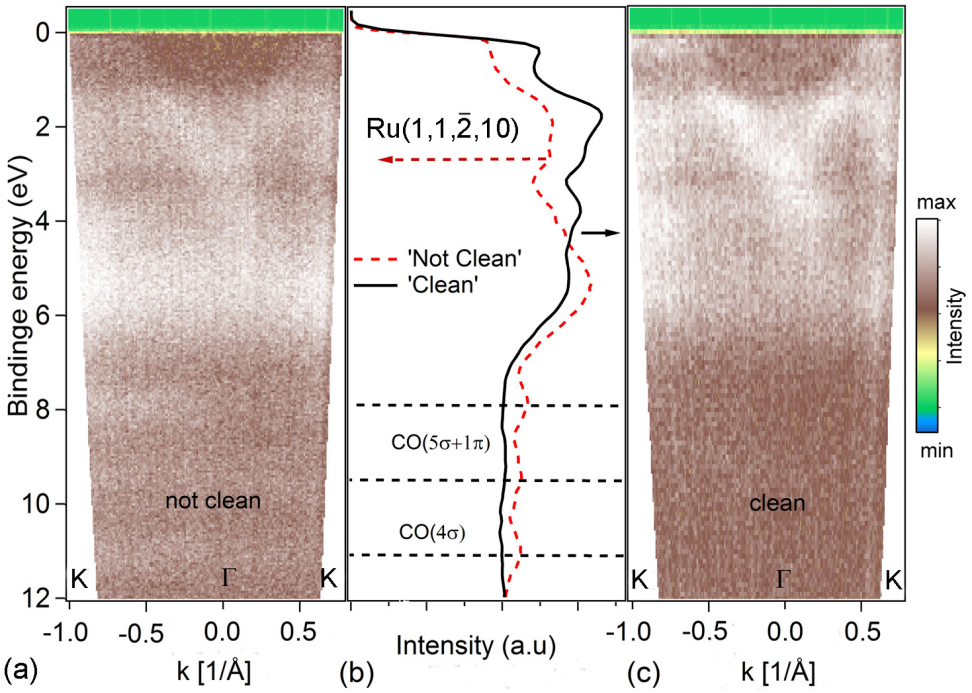

FIGURE 4.9: (a), (c) Band dispersion of the clean and not clean Ru(1,1,$\bar{2}$,10) surfaces measured at room temperature using helium II_α excitation, (b) angle-integrated valence band of the clean and not clean Ru(1,1,$\bar{2}$,10) surfaces. The black line shows the data measured on the clean surface while the red dashed line shows the Ruthenium surface contaminated with CO and Oxygen. The spectra are intensity-normalized to a common value at a binding energy of 13 eV.

binding-energy region, the peaks (originating from the ruthenium *4d* states) are weaker and broader in the contaminated surface compared with the data taken from the clean surface. Consistently, in the high binding-energy region, for the clean Ru(10$\bar{1}$0) surface around binding energies of 7.5 and 10.6 eV, there are *sp* dispersion bands of Ru and in the contaminated Ru surface there are two additional, dispersion-less bands which are originate from the presence of oxygen and carbon monoxide on the surface. This is also consistent with the angle-integrated valence bands of the clean and not clean Ru(10$\bar{1}$0). In the band of not clean Ru(10$\bar{1}$0), there are additional peaks at binding energies of 7.5 and 10.6 eV arising from oxygen and carbon monoxide on the surface. We attribute the peaks at 7.63 eV and 10.57 eV to carbon monoxide contamination. The studies of the adsorption of CO and oxygen on Ru(0001) by Fuggle *et al* [65] also show that the CO peaks at 7.5 and 10.6 eV can be assigned to the combined (5σ + 1π) and to the 4σ states, respectively.

There is a notable difference between the spectra of contaminated Ru(0001), Ru(1,1,$\bar{2}$,10) and Ru(10$\bar{1}$0). For Ru(10$\bar{1}$0), there are two contamination peaks are visible, one at about 7.5 eV and the other at about 10.6 eV. For Ru(0001) there are also two contamination peaks are visible, one at about 5.9 eV and the other at about 7.6 eV. In contrast, for Ru(1,1,$\bar{2}$,10) there are three contamination peaks are visible, one at about 7.9 eV, another at about 9.6 eV and the third at about 11 eV. The peak at about 5.9 eV in contaminated Ru(0001) is attributed to oxygen contamination [65]. The oxygen peak at 6.4 eV is believed to derive from the O 2p. The peak at about 9.6 eV in contaminated Ru(1,1,$\bar{2}$,10) is attributed to carbon contamination [65] and deriving from the π state of carbon. The peaks at 7.5 eV in contaminated Ru(10$\bar{1}$0), 7.6 eV in contaminated Ru(0001) and 7.9 eV in contaminated Ru(1,1,$\bar{2}$,10) are assigned to the combined (5σ + 1π) of CO [65]. Due to the differences in work function there are differences in the binding energy of CO(5σ + 1π) on the three Ru surfaces. In gas phase CO the difference in binding energy of CO(5σ) and CO(1π) is about 3 eV. Because CO is strongly chemisorbed on Ru surfaces, the binding occurs via the (5σ) orbital, lowering its energy approximately to the value of the (1π) orbital [48].

4.4 Calculated electronic structure of bulk Ruthenium

In this section, the additional calculated electronic structure of bulk Ruthenium will be presented. These theoretical calculations were done by Dr. Mulazzi (Ref. 16) and can be used as a reference to attain a better understanding of the experimental data. They also might be helpful for future projects.

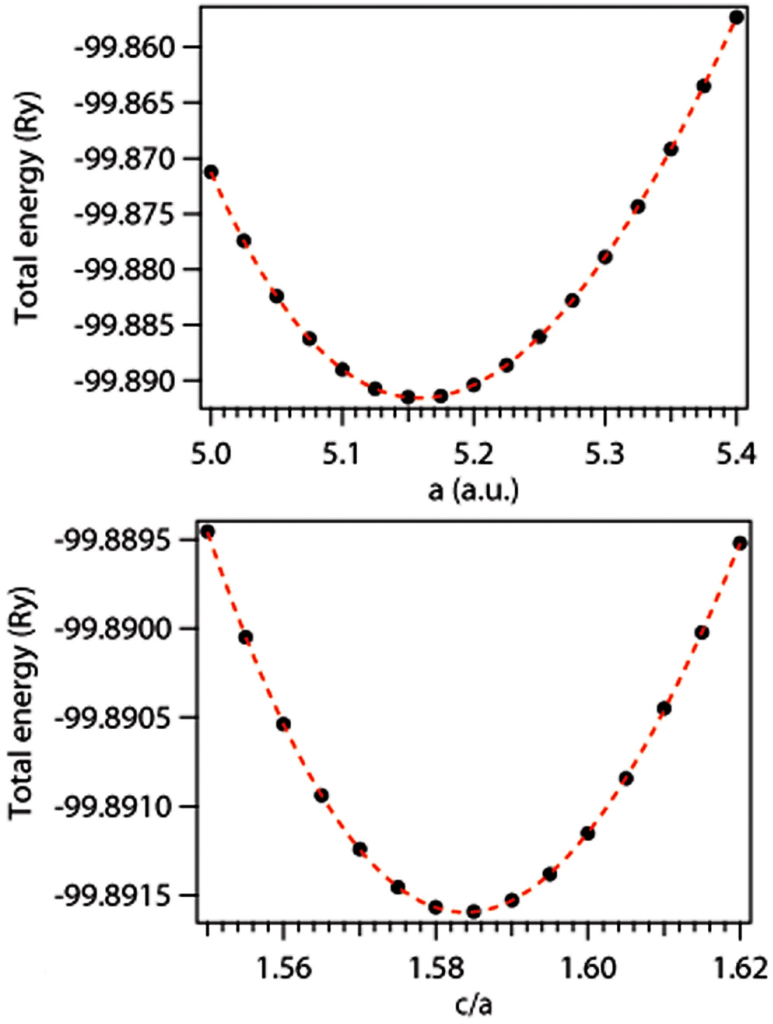

FIGURE 4.10: The calculated total energies are plotted as a function of the in-plane lattice parameter a (top) and as a function of the quotient of the out-of-plane lattice parameter c and a(bottom). The calculated total energy is indicated by the black dots, while the red dashed line is the result of a polynomial fit.

The band structure of bulk ruthenium was calculated by means of the density-functional theory (DFT) including spin-orbit interaction using a plane-wave-pseudopotential code [66] and a generalized-gradient approximation for the exchange and correlation functional. By varying the lattice parameters of the hexagonal-close-packed unit cell, the total energy was minimized, as shown in Fig. 4.10. The minimum total energy is located at $a = 5.15879$ a.u. and $c/a = 1.58376$, both being within 2 % from the experimental values [67]. In the self-consistent cycle, 252 k points of the irreducible wedge of the Brillouin zone were used. Using a $5s^1 4d^7$ configuration, the pseudo potential was generated; it was of the ultrasoft type. The energy cutoffs were 30 Ry and 360 Ry for the wave functions and the charge density, respectively.

When the photoelectron traverses to the surface, the value of the perpendicular momentum, $k_\perp$, is not conserved [47, 48]. But $k_\perp$ can be calculated by considering a

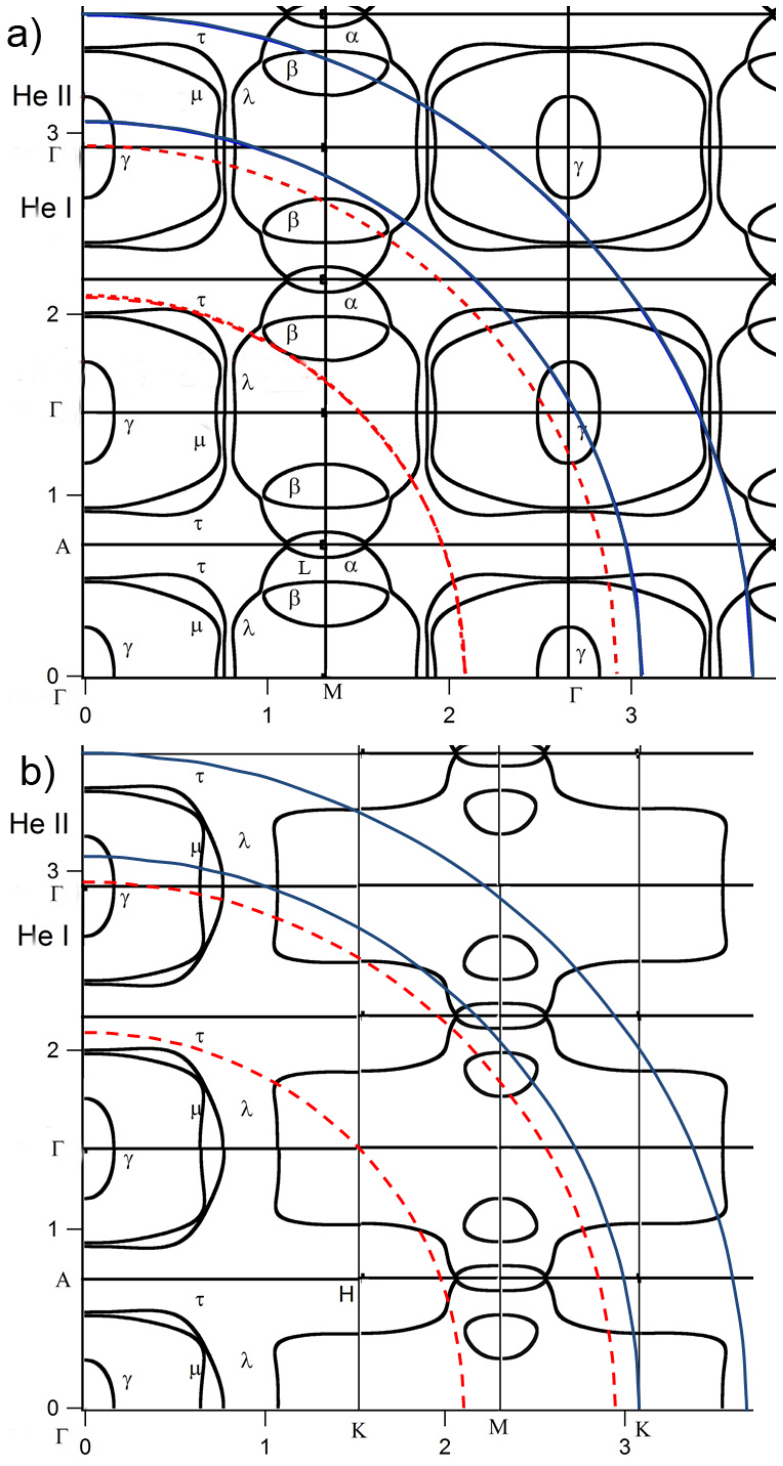

FIGURE 4.11: Calculation of the Fermi surface of bulk ruthenium in repeated Brillouin along the high-symmetry lines indicated in the figure, (a) in ΓA and ΓM direction and (b) in ΓA and ΓK direction. The radii of the red dashed and the blue solid lines indicate the constant-energy final-state sphere for excitation with the He I_α and He II_α excitation energies, respectively.

free-electron plane wave as the final state. In such a final state a constant kinetic energy, represented by a sphere in k-space, is proportional to the square of its momentum. The radius of this sphere is a function of the photoelectron kinetic energy, providing the reciprocal space points that are probed by a photoemission experiment, as indicated in Fig. 4.11 for different values of the inner potential and of the excitation energies, namely He I_α and He II_α.

The value of $k_\perp$ can be estimated by choosing the $k_\perp$ which provided the best agreement between the experimental and bulk calculations done for different values of $k_\perp$s of Fermi surfaces and band structures. It was then possible to determine the value of the inner potential by using the standard formula. The Fermi surface contours are shown in Fig. 4.12 in the ΓMK plane for different fractions of the ΓA vector which is considered as the unit of $k_\perp$ and which has to be compared with the ARPES data of Ru(0001). Similarly, the bulk Fermi surfaces plotted in the ΓAK plane for different values of the ΓM vector are shown in Fig. 4.13.

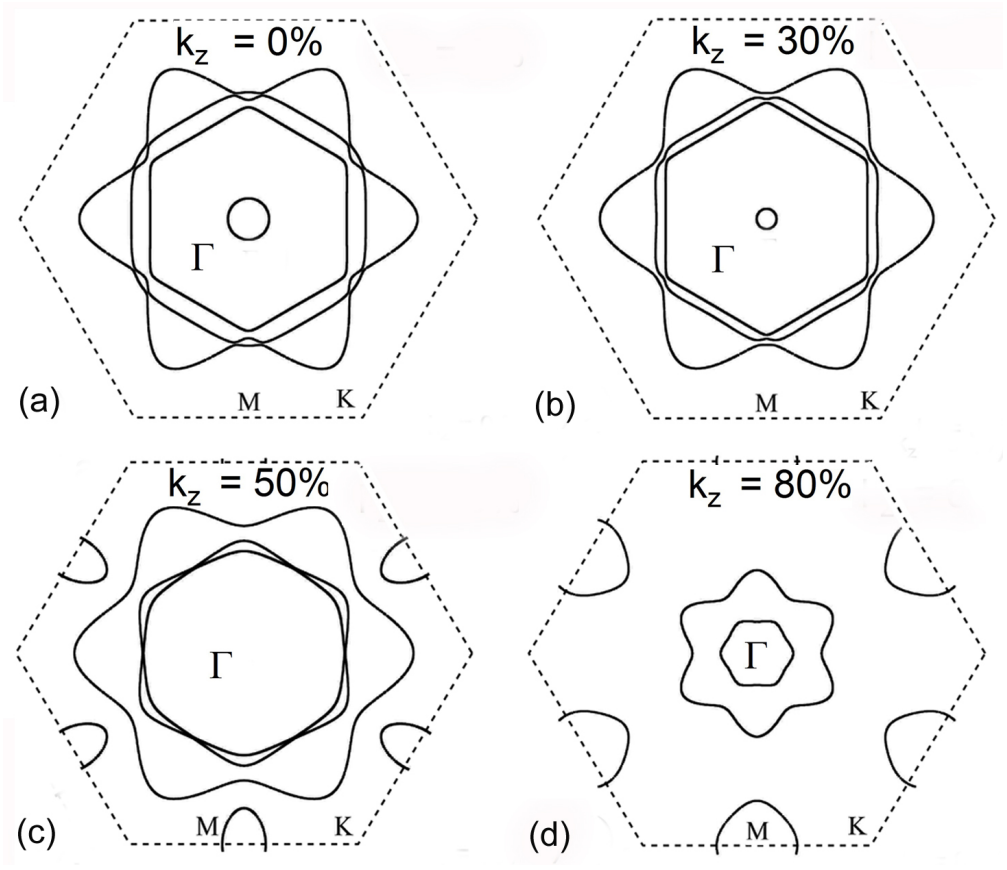

FIGURE 4.12: A selection of bulk Fermi surfaces calculated in the ΓMK plane for different $k_\perp$ which is parallel to the ΓA vector, given in fractions of the $\overline{\Gamma A}$ distance; 0 % corresponds to the Γ point and 100 % to the A point.

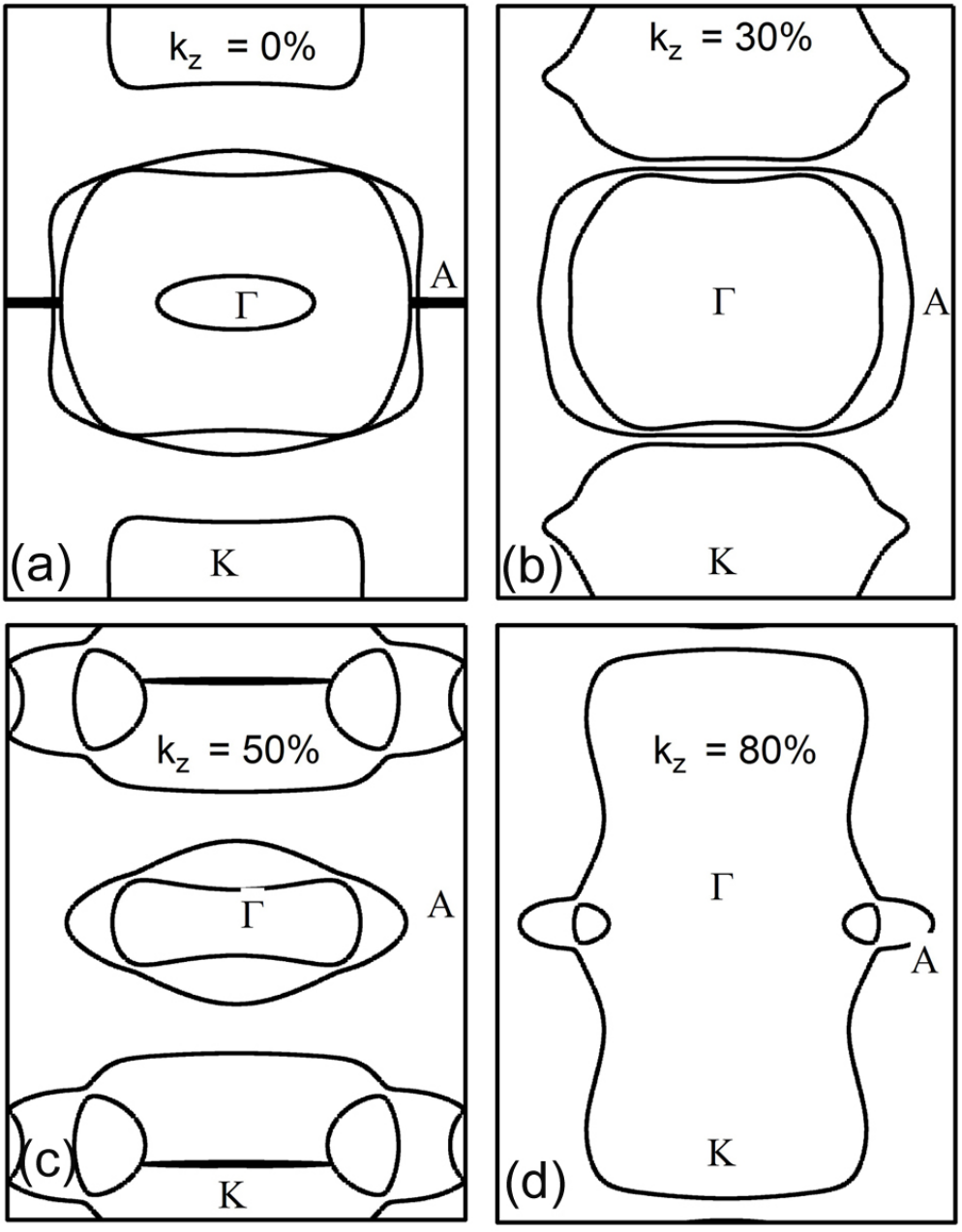

FIGURE 4.13: A selection of bulk Fermi surfaces calculated in the ΓAK plane for different $k_\perp$ which is parallel to the ΓM vector, given in fractions of the $\overline{\Gamma M}$ distance; 0 % corresponds to the Γ point and 100 % to the M point.

4.5 Fermi surface mapping of Ru surfaces

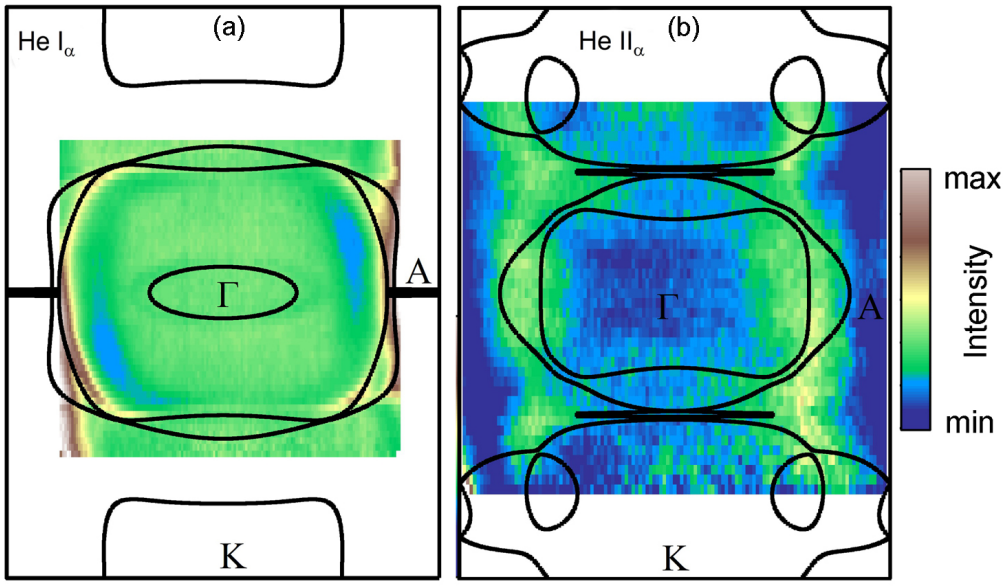

FIGURE 4.14: Experimental Fermi surfaces of Ru(10$\bar{1}$0) measured at 33 K using (a) He I$_\alpha$ and (b) He II$_\alpha$ excitation energies, respectively. The solid black lines are the calculated Fermi surfaces with $k_\perp$ equal to 0 % $\overline{\Gamma M}$ and 40 % $\overline{\Gamma M}$ for He I$_\alpha$ and He II$_\alpha$, respectively.

The experimental technique mainly used to measure bulk Fermi surfaces is the de Haas-van Alphen technique which was previously applied to ruthenium [57, 62]. Since it measures quantum oscillations in high magnetic fields, this technique has the disadvantage that the experiments have to be done with very pure crystals that need to be cooled to very low temperatures. In contrast, ARPES is a much more flexible technique providing valuable information about the surface electronic structure as a function of temperature and e.g. sample doping. Only one Fermi surface mapping experiment was done [15] for Ru(0001). The overall energy resolution was 350 meV and so far only one pattern with a sixfold symmetry was observed, while other features predicted by theory [57] and observed in the experimental de Haas-van Alphen bulk Fermi surface [62] were not be resolved. In our case, the overall energy resolution is 6 meV and the three surfaces Ru(0001), Ru(10$\bar{1}$0) and Ru(1,1,$\bar{2}$,10) were measured.

The solid black lines in 4.14 and Fig. 4.15 show the calculated Fermi surfaces. Fig. 4.14 presents the Fermi surface sections of Ru(10$\bar{1}$0) measured with He I$_\alpha$ and He II$_\alpha$ energies. In the Fermi surface data taken with He I$_\alpha$, an ellipse is located at the Γ point and two features of nearly rectangular shape are located between the center and the edges of the Brillouin zone. Due to the $k_\perp$ dispersion, these two features are also observable in the Fermi surface pattern measured with He II$_\alpha$ excitation energy, only with a different shape and size, while no ellipse around the Γ point can be found. Comparing these Fermi surfaces with the theoretical calculations, the best-fitting values of $k_\perp$ are 0 % and 40 %

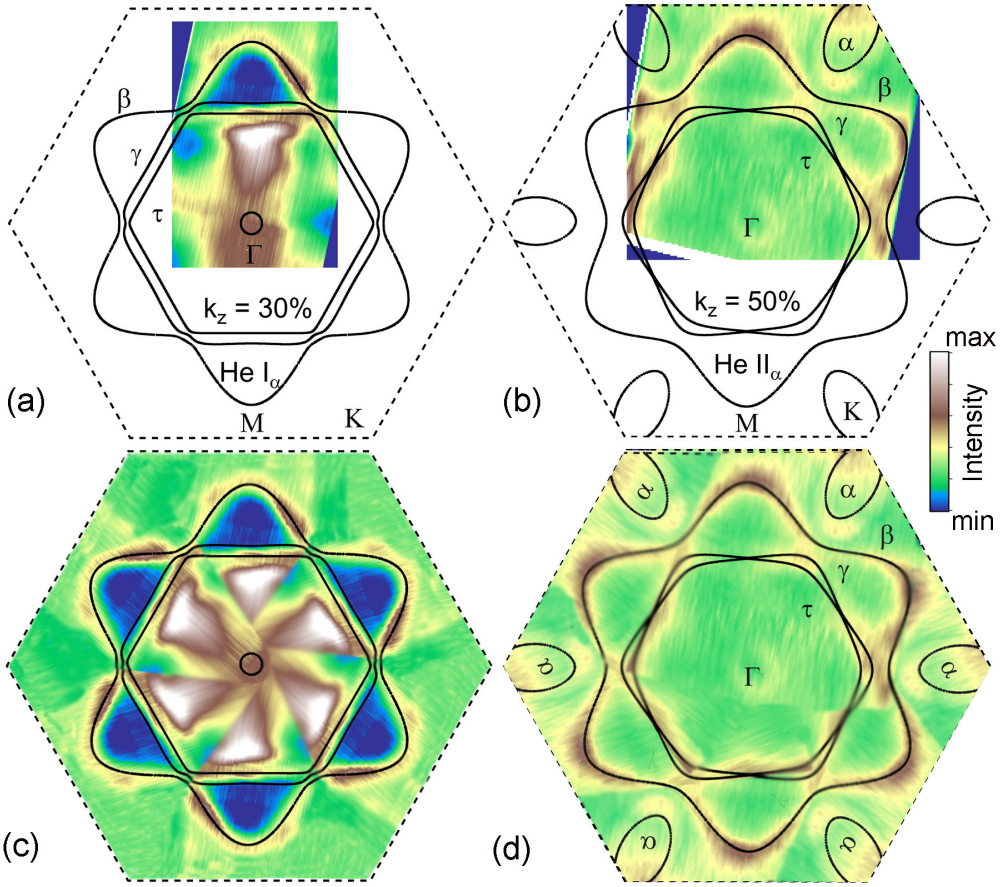

FIGURE 4.15: Experimental Fermi surfaces of Ru(0001) measured at 33 K using (a) He I_α and (b) He II_α excitation energies, respectively. The solid black lines indicate the calculated Fermi surfaces with $k_\perp$ equal to 30 % $\overline{\Gamma A}$ and 50 % $\overline{\Gamma A}$ for He I_α and He II_α, respectively. (c), (d) Symmetry images of (a) and (b), respectively.

of the ΓM reciprocal space vector, which corresponds to 2.68 ± 0.13 $Å^{-1}$ and 3.21 ± 0.13 $Å^{-1}$ for He I_α and He II_α, respectively. Assuming a free-electron final state, the inner potential V_0 can be determined by the equation 2.10. In our ARPES experiments, the photoelectron kinetic energies at the Fermi level are 16.77 eV and 36.33 eV for He I_α and He II_α excitation energies, respectively, yielding a value for the inner potential of 7 ± 3.5 eV.

The shape of the Ru(0001) Fermi surfaces measured with He I_α and He II_α shown in Fig. 4.15 are qualitatively similar, the main difference being a state around the M point detected only with He II_α excitation. Owing to the high energy resolution of our experiment, several features of the Fermi surface have been observed and labeled β, τ, γ and α, using the notation in Ref. [57]. The feature β corresponds to the sixfold flower-like pattern appearing in the experiment reported in [15]. The positions of the experimental bands are in quantitative agreement with the de Haas-van Alphen data and are, therefore, originating from bulk crystal properties. Consequently, the differences

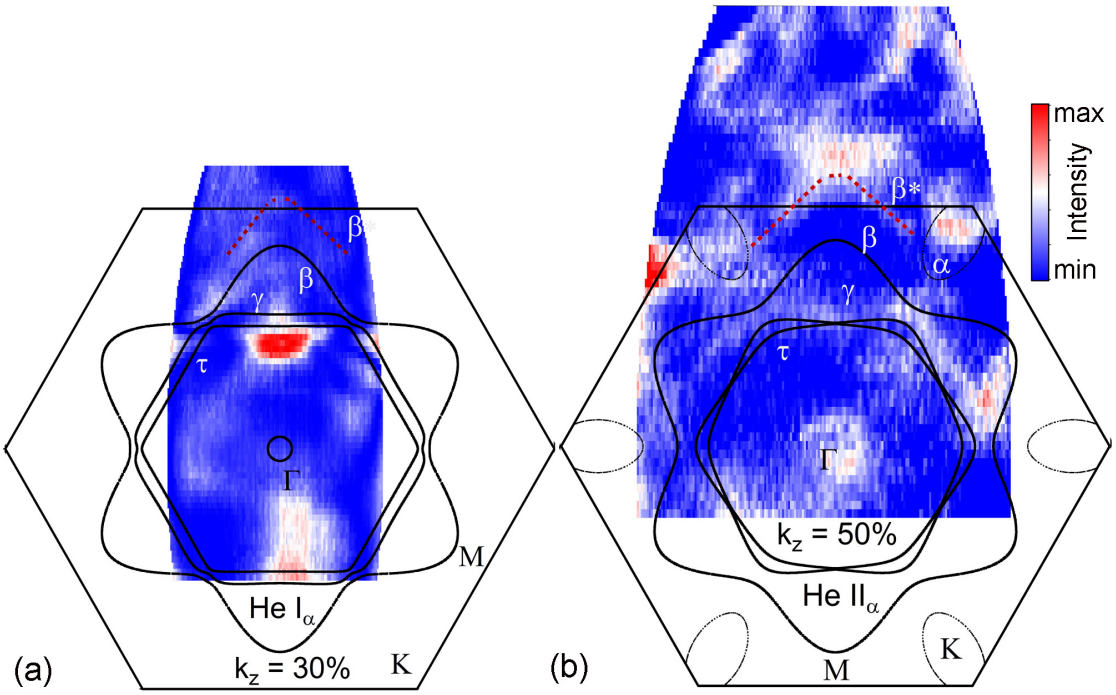

FIGURE 4.16: Experimental Fermi surfaces of Ru(1,1,$\bar{2}$,10) measured at 33 K using (a) He I$_\alpha$ and (b) He II$_\alpha$ excitation energies, respectively. The solid black lines indicate the calculated Fermi surfaces with $k_\perp$ equal to 30 % $\overline{\Gamma A}$ and 50 % $\overline{\Gamma A}$ for He I$_\alpha$ and He II$_\alpha$, respectively. The dashed red lines are additional states of Ru(1,1,$\bar{2}$,10) compared with Ru(0001).

between the data measured with He I$_\alpha$ and He II$_\alpha$ energies are assigned to the $k_\perp$ dispersion. The $k_\perp$ values that provide the best agreement between the theoretical and experimental data are 30 % for He I$_\alpha$ and 50 % for He II$_\alpha$) of the ΓA reciprocal space vector, corresponding to $k_\perp$(He I$_\alpha$) = 2.71 ± 0.07 Å^{-1} and $k_\perp$(He II$_\alpha$) = 3.31 ± 0.07 Å^{-1}, respectively, yielding an inner potential of 8.3 ± 2.9 eV.

For both surfaces that we examined the inner potential has been determined, but with an error bar of about 50%. The largest source of uncertainty in the values of the inner potential are certainly caused by the choice of $k_\perp$, which is obtained by the best fit of the theoretical band structure to the experimental data. Despite the good agreement between these two, there are discrepancies in the band dispersion and in the binding energies at the high-symmetry points. These discrepancies limit the accuracy to which $k_\perp$ can be determined to 10% of the distance between the Γ and A points for Ru(0001) and Γ and M points for Ru (10$\bar{1}$0).

Fig. 4.16 shows the Fermi surfaces of Ru(1,1,$\bar{2}$,10) measured at 33 K using He I$_\alpha$ and He II$_\alpha$ excitation energies. The solid black lines show the calculated Fermi surfaces with $k_\perp$ parallel to ΓA direction and equal to 30 % $\overline{\Gamma A}$ and 50 % $\overline{\Gamma A}$ for He I$_\alpha$ and He II$_\alpha$, respectively. It obvious that the Fermi surfaces of Ru(1,1,$\bar{2}$,10) are similar to

those of Ru(0001). All the features in the Fermi surface pattern of Ru(0001) can be observed in the Fermi surfaces of Ru(1,1,$\bar{2}$,10). In both Fermi surfaces of Ru(1,1,$\bar{2}$,10) an additional feature appeared which is denoted by $\beta*$. The feature $\beta*$ is only observed in ΓM direction in which the spot splitting appears in the LEED patterns shown in Fig. 4.4. The electronic properties of Ru(1,1,$\bar{2}$,10) will be discussed in more detail in the next section.

4.6 Electronic band structure of Ru surfaces

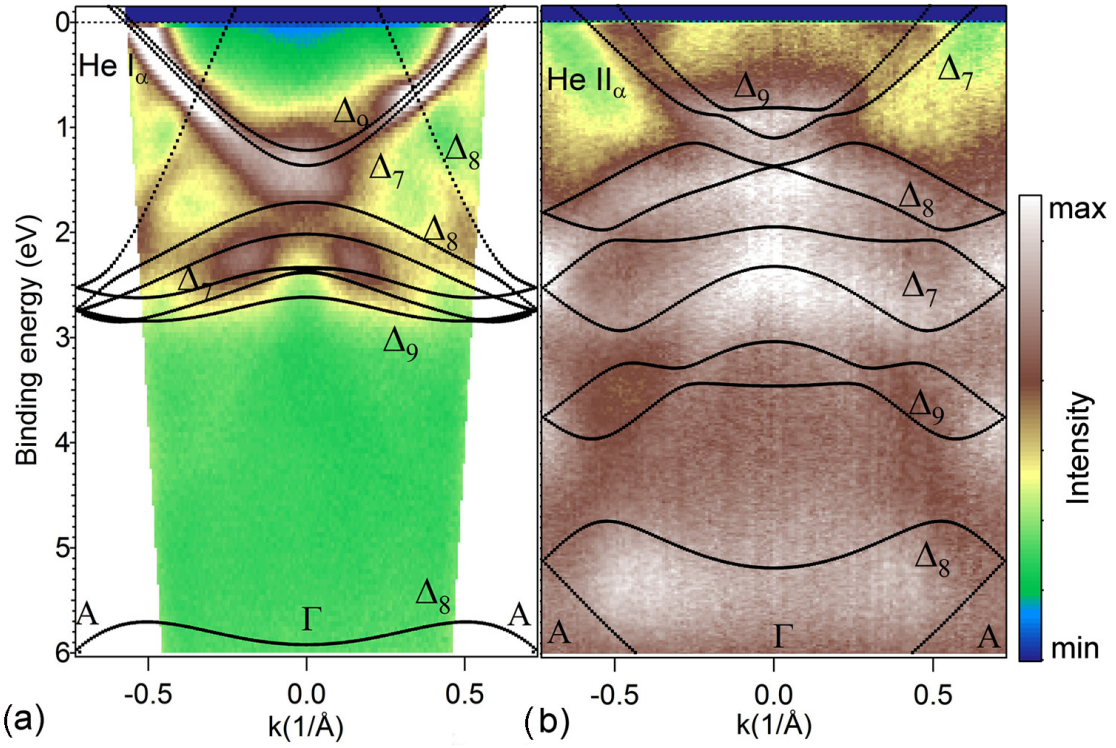

FIGURE 4.17: Band dispersion of the Ru(10$\bar{1}$0) surface measured at 33 K (a) using He I$_\alpha$ excitation and (b) using He II$_\alpha$ excitation. The dotted black lines are the calculated bands obtained for $k_\perp = 0$ % $\overline{\Gamma M}$ and 40 % $\overline{\Gamma M}$ for He I$_\alpha$ and He II$_\alpha$, respectively.

The experimental band dispersion of Ru(10$\bar{1}$0) is shown in Fig. 4.17 measured with He I$_\alpha$ and He II$_\alpha$ energies along with the bands calculated for $k_\perp = 0$ % and $k_\perp = 40$ %, respectively. The dotted black lines represent the calculated bulk band structure. In the He I$_\alpha$ data shown in Fig. 4.17(a) there are two electron-like bands at about $E_B = 1.2$ eV at the Γ point separated by about 0.2 eV and denoted by Δ_9 and Δ_7. The Δ_9 state is of *sp*-like character while the Δ_7 is *d*-like [57]. The experimental data are in very good agreement with our relativistic band structure calculations. The structure at 5.6 eV denoted by Δ_8 is associated with the flat *d*-like section of the lowest band [14].

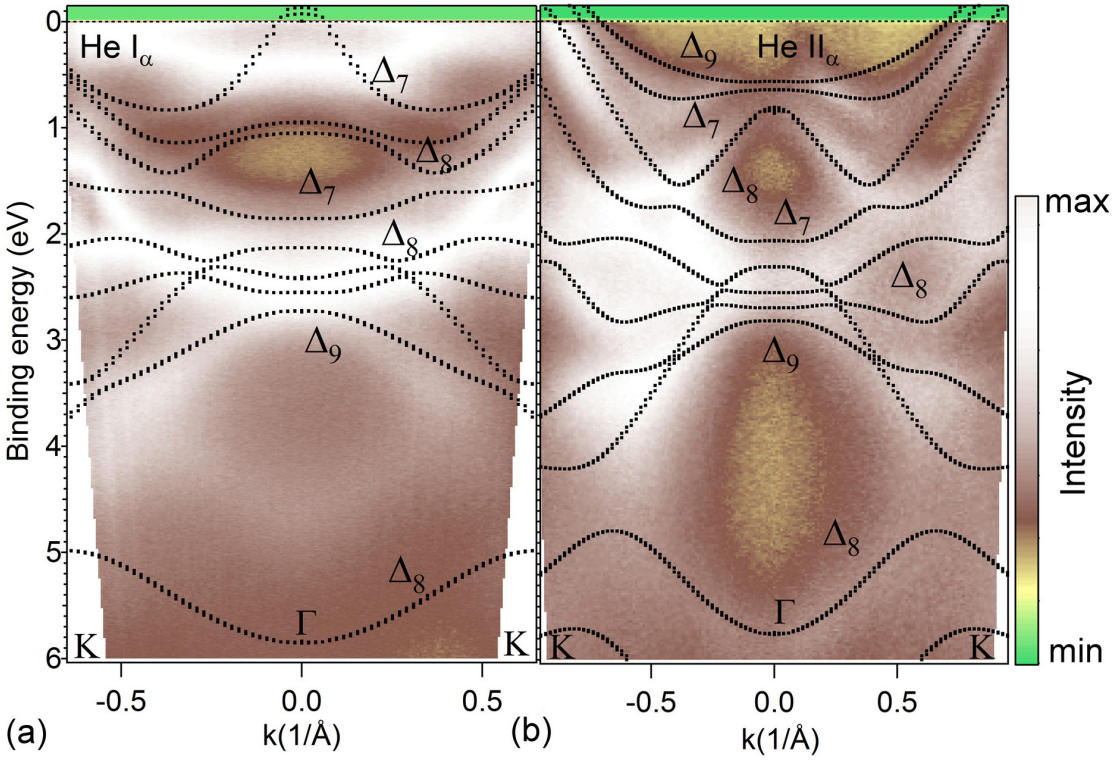

FIGURE 4.18: Band dispersion of the Ru(0001) surface measured at 33 K (a) using He I$_\alpha$ excitation and (b) using He II$_\alpha$ excitation. The dotted black lines are the calculated bands obtained for $k_\perp$ = 30 % $\overline{\Gamma A}$ and 50 % $\overline{\Gamma A}$ for He I$_\alpha$ and He II$_\alpha$, respectively.

The experimental band dispersion of Ru(0001) is displayed in Fig. 4.18 for the two excitation energies He I$_\alpha$ and He II$_\alpha$. The calculated bulk band structure is also shown in Fig. 4.18 by the dotted black lines. Overall, the experimental band dispersion of Ru(0001) is consistent with previous data [13–15] but due to the higher energy resolution new details of the dispersion were observed. We follow the notation used in Ref. [60] to label the bands. At the Γ point, about 0.5 eV below the Fermi energy in Fig. 4.18(a) and about 0.7 eV in Fig. 4.18(b), there is a very pronounced set of peaks that can be attributed to the three bands denoted by Δ_7, Δ_8 and Δ_9 which are states of *sp*- and *d*-like character. Having its maximum above the Fermi energy and dispersing into the occupied states, a hole-like surface state was predicted [60]. It should also contribute to the experimental photoemission intensity, but in our calculations it cannot be present [16]. To achieve the best agreement possible between theory and experiment, the experimental data were compared with the theoretical band structure obtained for fractions of 30 % and 50 % of the ΓA vector for He I$_\alpha$ and He II$_\alpha$ excitation energy, respectively. In Fig. 4.18(a), there is evidence of a rather weak but well distinguishable peak at a binding energy of 4.5 eV in the He I$_\alpha$ spectra. It clearly shows a dispersion in the experimental data, so it cannot be an Auger transition as attributed in previous works [14]. For this reason, the peak at 4.5 eV in the He I$_\alpha$ spectra is attributed to a surface state which is

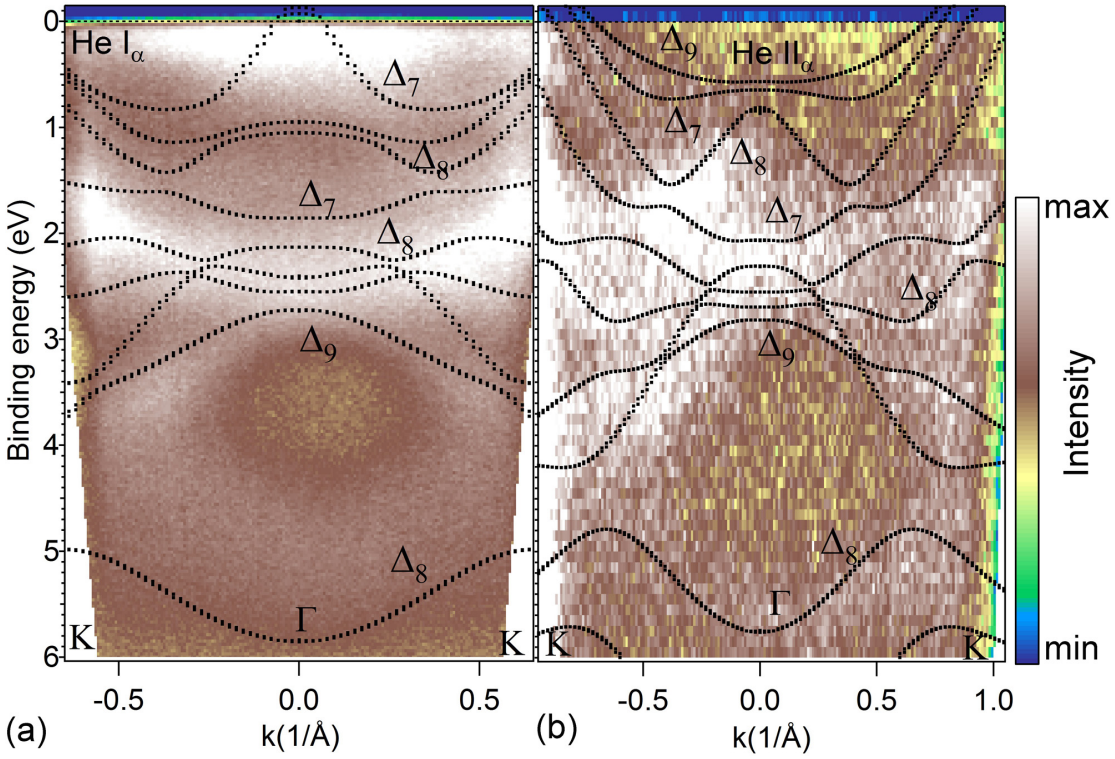

FIGURE 4.19: Band dispersion of the Ru(1,1,$\bar{2}$,10) surface measured at 33 K in the ΓK direction, i.e. parallel to the step edge, (a) using He I$_\alpha$ excitation and (b) using He II$_\alpha$ excitation. The dotted black lines are the calculated bands obtained for $k_\perp = 30$ % $\overline{\Gamma A}$ and 50 % $\overline{\Gamma A}$ for He I$_\alpha$ and He II$_\alpha$, respectively.

also an suggested by other theoretical works.

It can easily be seen that there is a better general agreement between theory and experiments if the comparison is limited to the Fermi surfaces. Although the experimental bands are in overall good agreement with the theoretical ones, there are inconsistencies as well. For instance, in Fig. 4.18(b), the experimental bands Δ_9 and Δ_7 near the Fermi energy along ΓK have a binding energy minimum at a k-vector that is not found by theory and the Δ_8 band in Fig. 4.18(a) has also a minimum with a k-vector position too small with respect to the theoretical value. These discrepancies cannot be attributed to a wrong choice of the lattice parameter, because the unit cell was relaxed and the experimental and theoretical values are in very good agreement. It also cannot be attributed to spin-orbit coupling since this is taken into account in the calculations. The discrepancies for these particular bands measured along the ΓM direction might be explained by a wrong choice of $k_\perp$ but a different choice would induce disagreements for other bands at other k-vectors. Another possible explanation is the neglect of the surface and of surface relaxations which could induce changes in the effective masses and, thus, in the dispersion law. However, no such effect has been reported in previous theoretical works which were dedicated to the existence of surface states and resonances in the bulk band gaps.

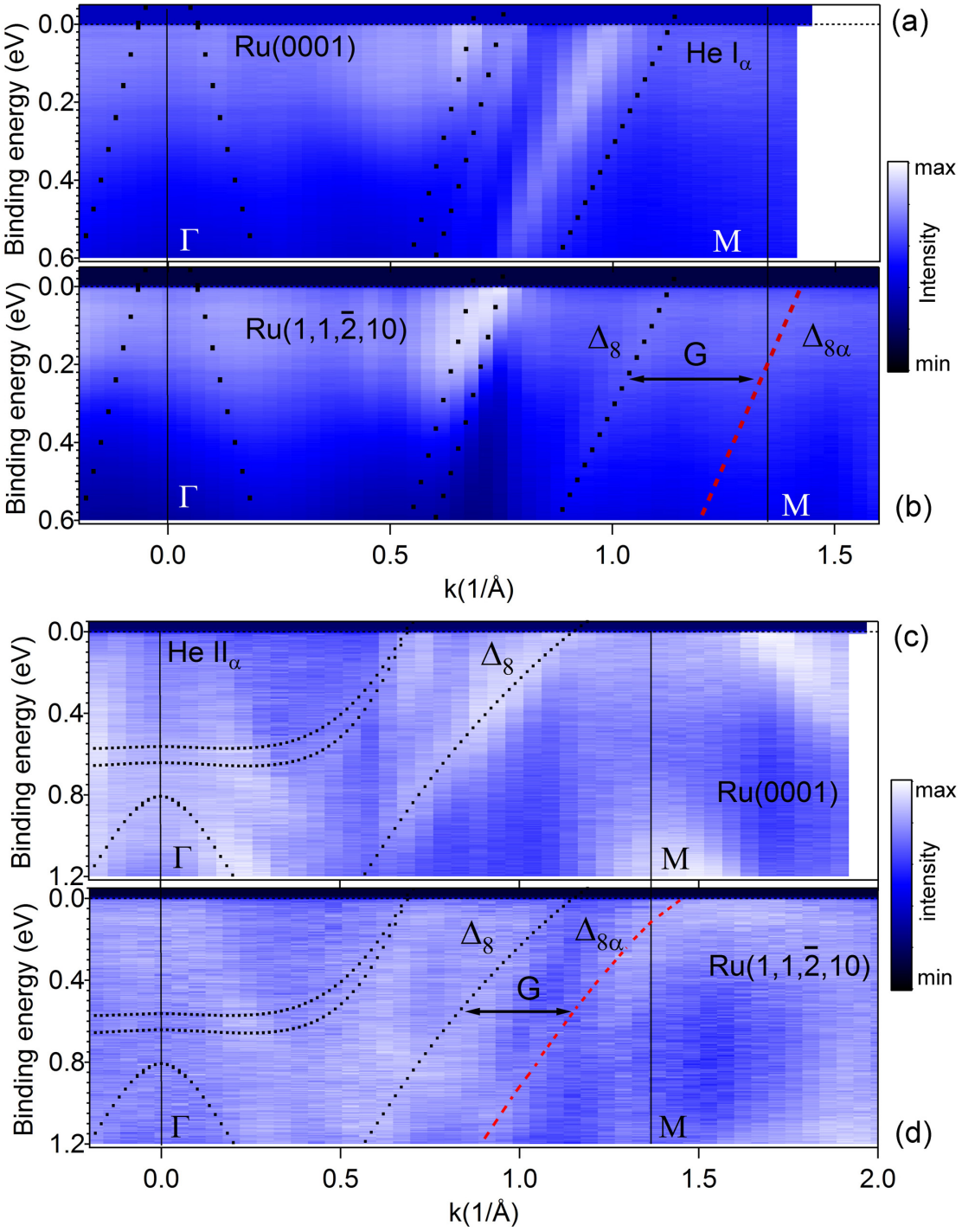

FIGURE 4.20: Band dispersion of Ru(0001) and Ru(1,1,$\bar{2}$,10) measured at 33 K in the ΓM direction, i.e. perpendicular to the step edge, (a) for Ru(0001) and (b) for Ru(1,1,$\bar{2}$,10) using He I$_\alpha$ excitation, and (c) for Ru(0001) and (d) for Ru(1,1,$\bar{2}$,10) using He II$_\alpha$ excitation. The dotted black lines are the calculated bands obtained for $k_\perp$ = 30 % $\overline{\Gamma A}$ and 50 % $\overline{\Gamma A}$ for He I$_\alpha$ and He II$_\alpha$, respectively

Band dispersions of Ru(1,1,$\bar{2}$,10) measured in the direction parallel to the step edge, i.e. the ΓK direction, are presented in Fig. 4.19 (a) using He I_α excitation and (b) using He II_α excitation. The dotted black lines show the calculated bands obtained for $k_\perp = 30$ % $\overline{\Gamma A}$ and 50 % $\overline{\Gamma A}$ for He I_α and He II_α, respectively. The band structure of Ru(1,1,$\bar{2}$,10) in ΓK direction is similar to that of Ru(0001). It is consistent with previous studies of the electronic properties of stepped surfaces [29, 30, 68–72]. Due to an additional periodicity in one dimension, the step array on vicinal surfaces induces an anisotropy of the electronic properties [29]. The wave functions in the direction parallel to the step edge show no influence of the step array while in the direction perpendicular to the step edge the wave functions represent a different electronic structure [70]. The band dispersion of Ru(0001) and Ru(1,1,$\bar{2}$,10) measured at 33 K in the direction perpendicular to the step edge, i.e. the ΓM direction, is shown in Fig. 4.20 (a) for Ru(0001) and (b) for Ru(1,1,$\bar{2}$,10) using He I_α excitation, and (c) for Ru(0001) and (d) for Ru(1,1,$\bar{2}$,10) using He II_α excitation. The dotted black lines show the calculated bands obtained for $k_\perp = 30$ % $\overline{\Gamma A}$ and 50 % $\overline{\Gamma A}$ for He I_α and He II_α, respectively. Comparing the band structure of Ru(0001) and Ru(1,1,$\bar{2}$,10) in the ΓM direction, we can see clearly that for Ru(1,1,$\bar{2}$,10) in both the He I_α excitation and the He II_α excitation an additional feature appears which is denoted by $\Delta_{8\alpha}$. It is a repeated Δ_8 band in Ru(0001). The distance, G, between the two bands $\Delta_{8\alpha}$ and Δ_8 is about 0.4 Å^{-1} or $G = 2\pi/D$., where D is the periodicity of the step arrangement in Ru(1,1,$\bar{2}$,10) and G indicates a reciprocal superlattice vector. The new feature in the band structure of Ru(1,1,$\bar{2}$,10) is in agreement with the Fermi surface in Fig. 4.16 and the LEED patterns in Fig. 4.4. It is also consistent with previous band structure measurements of stepped surfaces in the direction perpendicular to the step edge [29, 68, 69]. Depending on the terrace width, there are different types of dispersion for surface states in the direction perpendicular to the step edge. For wider terraces or small miscuts, the electron wave functions in the terraces can be considered as independent and interacting incoherently [68]. The surface state is observed as a single parabola centered around the normal of the microsurface [29] or the quantum-well states with no dispersion [70, 73]. For narrow terraces or large miscuts, the electron wave functions in the terraces can interact coherently, leading to a repeated band dispersion related to the step periodicity [69] or a single parabola arranged relative to the macrosurface [29, 68]. The repeated band dispersion of the Δ_8 in Ru(1,1,$\bar{2}$,10) is expected for a lateral surface superlattice by Umklapp processes due to a periodic modulation of the surface potential by the steps [69].

4.7 Summary

The details of the electronic structures of three ruthenium surfaces, Ru(0001), Ru $(10\bar{1}0)$ and Ru(1,1,$\bar{2}$,10), were investigated. I have shown an other method which is very easy and gives accurate results for the cleanness of Ru surfaces by using ARPES. Ru(1,1,$\bar{2}$,10) was estimated to have, as expected, five-atom wide (0001) terraces and one-atom high steps. In the band structure of Ru(1,1,$\bar{2}$,10), a repeated band is observed.

Chapter 5

Graphene on Ru surfaces

5.1 Introduction

The interaction of graphene with metal surfaces has been studied for about 50 years [74]. The extraordinary fundamental properties of a two-dimensional atomic sheet of sp^2-bonded carbon atoms arranged in a honeycomb lattice have been fully understood only after a single-layer free-standing sheets had been successfully prepared [5–7]. From the application point of view, metal surfaces can be used as growth templates for large mono- and bilayer sheets [22, 75] before transferring graphene onto an insulating or polymeric support. Graphene on metal surfaces also can be used as a transparent conductive electrode for the production of flexible-panel displays [12, 76] or as a capping layer material for mirror protection in extreme-ultraviolet lithography [27]. From the fundamental point of view, the interaction of graphene with metal surfaces is still not understood. The bonding of graphene with transition metal surfaces can be classified as either "strong" or "weak" [56]. "Strong" bonding metals, like Co(0001) [77], Ni(111) [78, 79], Ru(0001) [8], Rh(111) [80] and Re(0001) [81] show a modification of the electronic structure of the graphene due to charge transfer from the metal to the graphene sheet. As a result, the π-band of the graphene is shifted by about 2 eV to higher binding energy compared to free-standing graphene and the distance between graphene and metal surface is about 0.21 nm. In contrast, the "weak" bonding Ir(111) [82, 83], Pt(111) [83, 84], Pd(111) [85], Cu(111) [86, 87], Ag(111) [86, 88], Au(111) [86, 89] and Fe(111) [90], leave the electronic structure intact, i.e the graphene shows no significant binding energy shifts and its distance from the metal surface is larger than 0.30 nm.

Previous studies of graphene mostly focused on the metal surfaces with hexagonal closed packed (0001) or face-centered cubic (111) structures which provide a suitable symmetry match to the graphene lattice. Only a few groups investigated graphene on surfaces of

different symmetry, such as graphene on polycrystalline Cu [91–95], graphene on polycrystalline Ni [96, 97], and graphene on polycrystalline Ru [98]. However, they also only concentrated on the geometric structure of graphene on polycrystalline surfaces. Graphene on Ru(0001) has been studied in detail [9, 17, 98–109] because of the high-quality samples that can be obtained. It was shown that when annealing Ru(0001) at high temperatures (about 1400 K), the carbon atoms from the bulk segregate to the Ru(0001) surface and form graphene sheets [9, 100]. Sutter *et al.* [98] found that graphene can be grown continuously over many Ru grains with varying interfacial structure. Here I will show that graphene can be grown in a well-ordered structure on Ru(10$\bar{1}$0) which has a rectangular surface unit cell of different symmetry compared to Ru(0001) and all other surfaces previously studied. Graphene on Ru(0001) and on Ru(10$\bar{1}$0) has a different lattice mismatch and, therefore, studying the interaction of graphene with Ru(0001) and with Ru(10$\bar{1}$0) may give some clues about the effect of the lattice mismatch on the bonding of graphene with transition metals. Moreover, we also find that graphene can be grown in a well-ordered structure on Ru(1,1,$\bar{2}$,10).

5.2 Geometric properties of graphene on Ru surfaces

Fig. 5.1 shows the LEED patterns of (a) clean Ru(0001) with electron beam energy $E_o = 100$ eV, and (b), (c), (d) graphene on Ru(0001) with $E_o = 15$ eV, 100 eV and 150 eV, respectively. Clearly visible are the hexagonal pattern and the superstructure satellites around the substrate spots. The well-defined superstructure spots correspond to a Moiré pattern with an approximate periodicity of 12 graphene hexagons overlaid on 11 Ru atoms, which is a signature of the lattice mismatch between the graphene lattice constant (2.46 Å for bulk graphite) and that of Ru(0001) (2.71 Å). Fig. 5.2 presents atomic-resolution STM images of graphene on Ru(0001) measured at room temperature depicted on different lateral scales. The ordered hexagonal pattern in Fig. 5.2 has a lattice constant of about 30 Åwhich approximately corresponds to 12 carbon atoms (12 x 2.46 (Å) = 29.5 Å) overlaid on 11 Ru(0001) atoms (11 x 2.71 (Å) = 28.8 Å), consistent with the LEED patterns. Previous studies of graphene on Ru(0001) have found that there are two Moiré periodicities, one being a (10 x 10) Ru structure [99] with a compressive strain of 0.05 % and the other a (11 x 11) Ru structure [9] with a tensile strain of about 0.78 %. Recent LEED I(V) and SXRD studies indicated a (23 x 23) superstructure with (25 x 25) graphene unit cells lying on top of (23 x 23) Ru surface unit cells [100, 104]. This structure consists of four almost identical subunits, each of which has a (12.5 x 12.5) C / (11.5 x 11.5) Ru structure, therefore being defined as quasi-periodic [100, 104]. From theoretical calculations, two Moiré periodicities, one a (10 x 10) and the

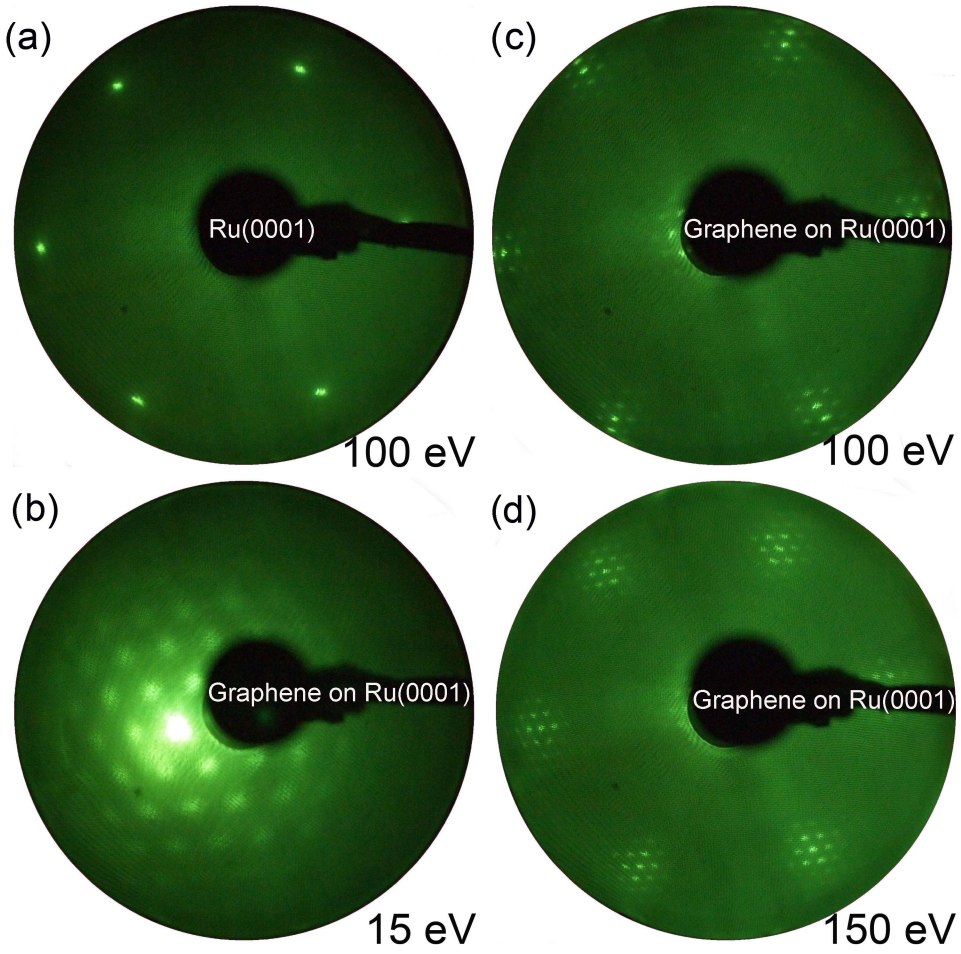

FIGURE 5.1: LEED patterns of (a) clean Ru(0001) measured at 100 eV and (b), (c), (d) graphene on Ru(0001) measured at 15 eV, 100 eV and 150 eV, respectively. The diffraction patterns in (b), (c) and (d) are caused by a Moiré structure with an approximate periodicity of 12 graphene hexagons overlaid on 11 Ru(0001) atoms.

other a (11 x 11) superstructure, have been studied by several groups [103, 106, 107, 110–114] who pointed out that due to the balance between strain and bonding the (11 x 11) superstructure is energetically more stable than the (10 x 10) superstructure which is, however, the one with the lower strain [110, 111].

Fig. 5.3 shows the LEED patterns of clean Ru(10$\bar{1}$0) and Ru(10$\bar{1}$0) covered with graphene obtained by heating the sample to 1400 K in 90 s, i.e. with the same procedure as used for the Ru(0001). Contrary to the Ru(0001) results, the superstructure diffraction spots are aligned in only one direction, as can be seen in Fig. 5.3(b), (c) and (d). Like in the Ru(0001) case, the distance between the (1 x 1) spots and the reconstruction-related ones which we measured corresponds to a periodicity of approximately 11 Ru lattice constants. Fig. 5.4 shows atomic-resolution STM images of Ru(10$\bar{1}$0) measured at room temperature. It is visible that there are two main components on two very different, characteristic scales: one on the atomic scale and being ascribable to the carbon

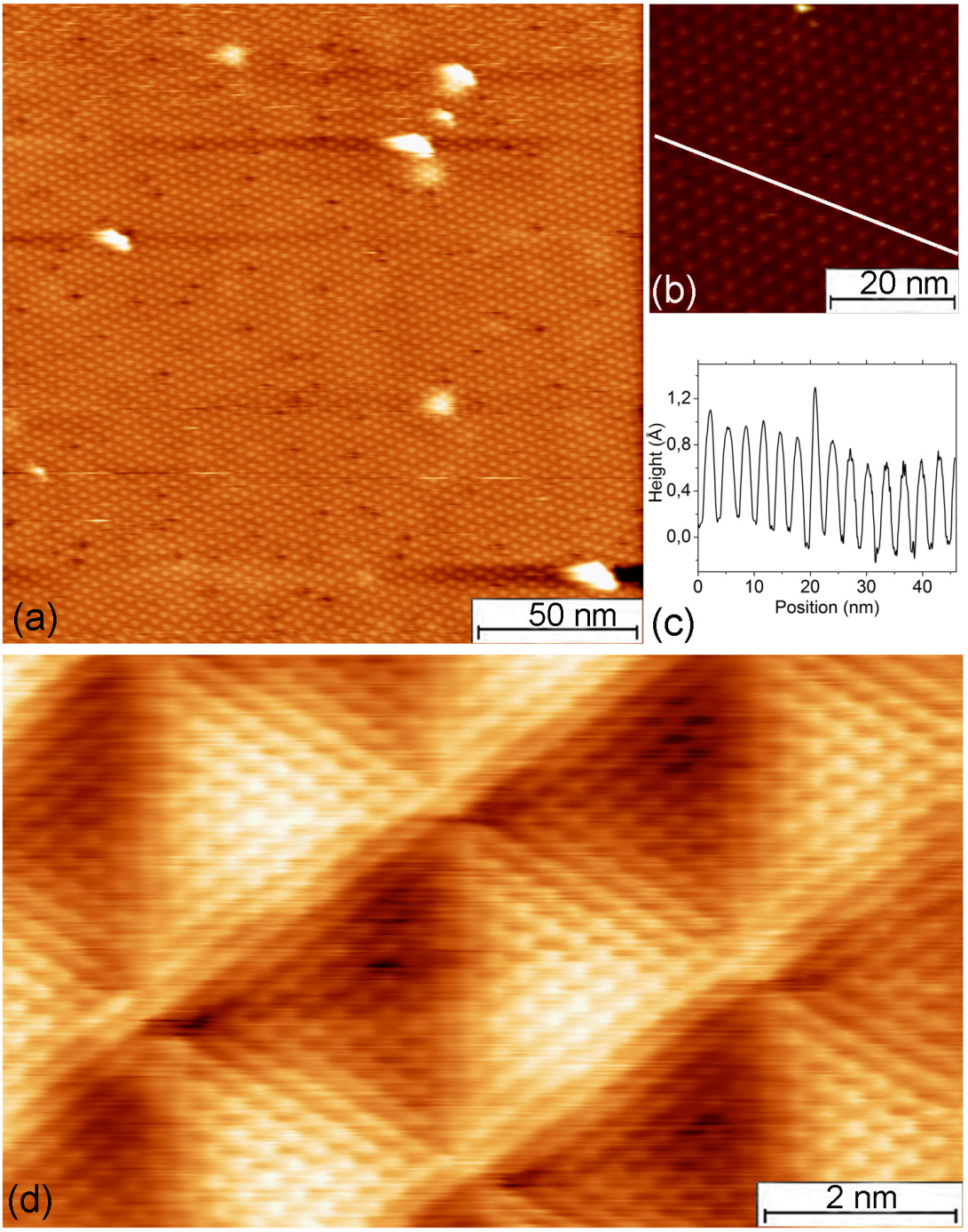

FIGURE 5.2: STM images of graphene on Ru(0001) measured at room temperature. The lattice constant is about 30 Å. Represented areas are (a) 200 nm x 200 nm, and (b) 50 nm x 50 nm with $I = 1$ nA, $V_{bias} = -0.6$ V, and (d) 6 nm x 10 nm with $I = 1$ nA, $V_{bias} = 0.2$ V. (c) Height profile along the white line in (b).

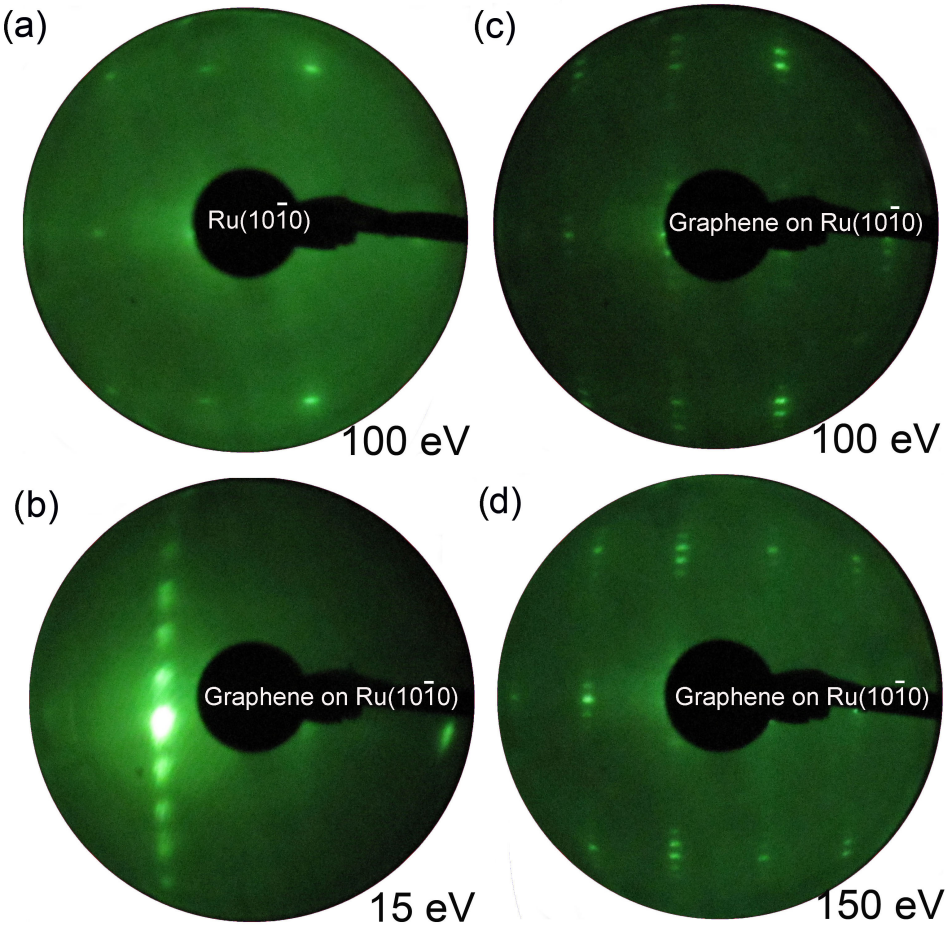

FIGURE 5.3: LEED patterns of (a) clean Ru(10$\bar{1}$0) measured at 100 eV and (b), (c), (d) graphene on Ru(10$\bar{1}$0) measured at 15 eV, 100 eV and 150 eV, respectively. The satellite spots in one direction are caused by a Moiré structure with an approximate periodicity of 12 graphenes overlaid on 11 Ru(10$\bar{1}$0) atoms.

atoms of graphene and the other one having a periodicity of about 30 Å and modulating the STM signal in only one direction. The direct imaging obtained by STM is in very good agreement with the LEED patterns shown in Fig. 5.3, also indicating the homogeneity of the films over lateral dimensions on the order of the electron beam width, i.e. a few millimeters. The periodicity of the large-scale modulation is the same as that of the ordered graphene on Ru(0001) despite being no longer six-fold symmetric. This is further evidence that the heating treatment produces, independent of the surface orientation, large graphene layers forming superlattices having the same periodicity. The remarkable difference is that the substrate lattice symmetry of Ru(10$\bar{1}$0) induces one-dimensional modulation of the long-range order.

A simple geometrical model of the structure of graphene on Ru(10$\bar{1}$0) is presented in Fig. 5.5, in which the lattice parameters for both materials are indicated. We assumed that the carbon atoms are adsorbed on top of the Ruthenium atoms. Thus, the lattice

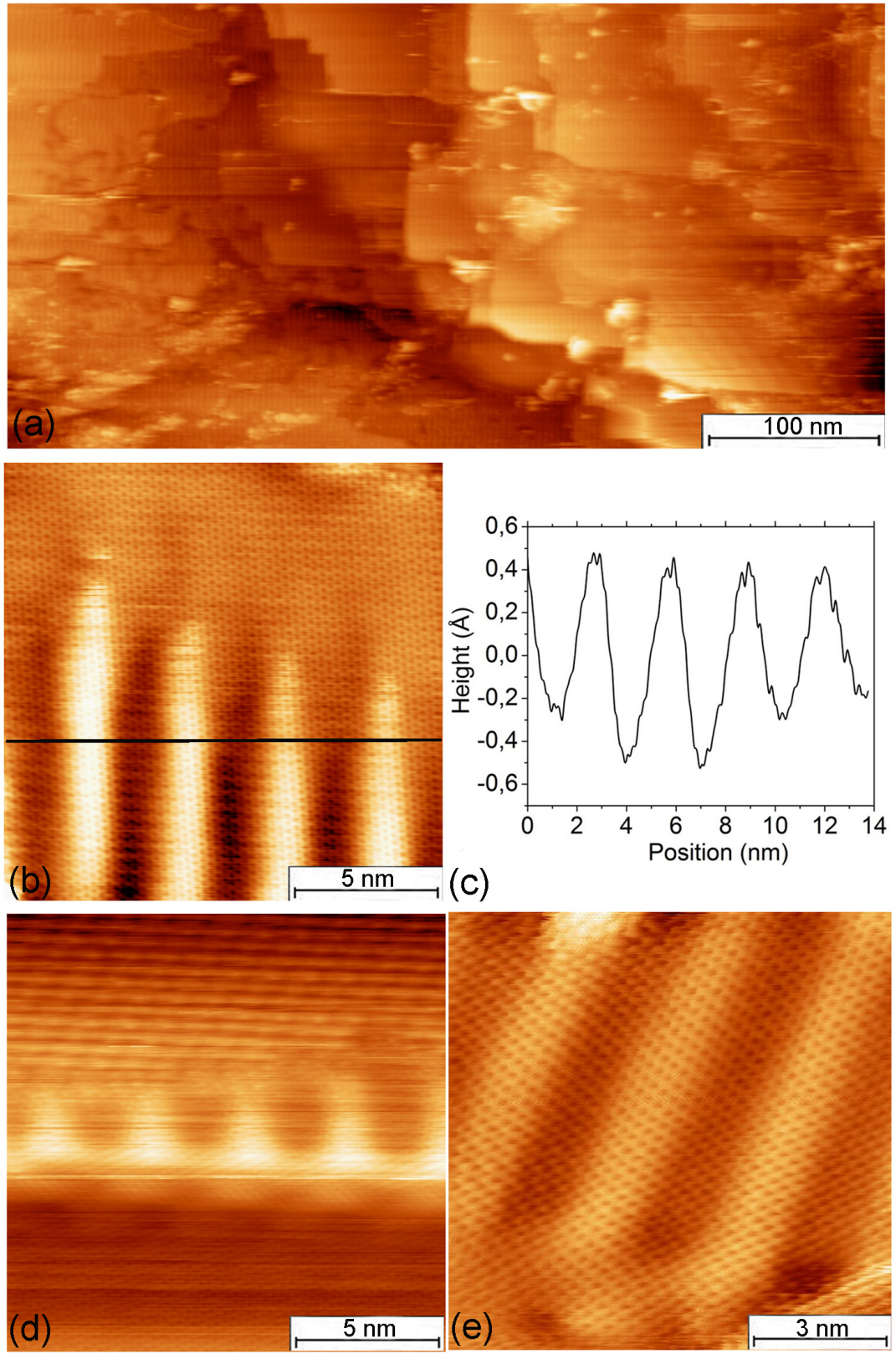

FIGURE 5.4: STM images of graphene on a Ru($10\bar{1}0$) surface measured at room temperature. Represented areas are (a) 250 nm x 500 nm with $I = 0.2$ nA, $V_{bias} = 100$ mV, (b) and (c) 15 nm x 15 nm with $I = 0.3$ nA, $V_{bias} = -500$ mV, and (e) 10 nm x 10 nm with $I = 0.5$ nA, $V_{bias} = -50$ mV. (d) Height profile along the white line in (b). The lattice constant is about 30 Å.

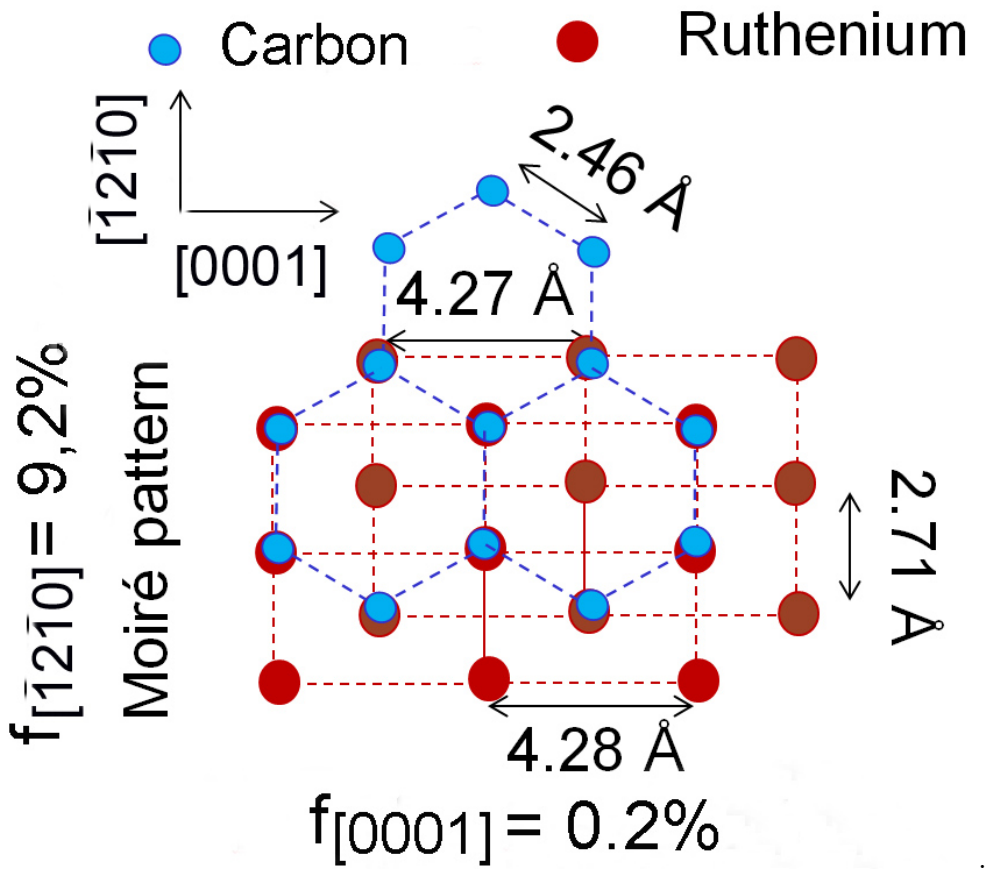

FIGURE 5.5: Atomic structure of graphene on Ru(10$\bar{1}$0) viewed from above. In the [0001] direction, the lattice mismatch between carbon and Ru is only $f_{[0001]} = 0.2\,\%$. In the [$\bar{1}$2$\bar{1}$0] direction, the lattice mismatch is $f_{[\bar{1}2\bar{1}0]} = 9.2\,\%$. Therefore, the Moiré structure is present only along the [$\bar{1}$2$\bar{1}$0] direction.

mismatch between the graphene and the Ru surface is $f = 100\%|(a_{Ru} - a_C)|/a_{Ru}$. Along the [0001]-direction, the lattice mismatch is only 0.2 % and carbon is on top of Ru at every lattice site given the negligible difference in the interatomic distances along this direction. Along the [$\bar{1}$2$\bar{1}$0] direction the carbon lattice is mismatched by about 9.2 % with respect to the Ruthenium one. For this reason, the Moiré structure is present only along one direction for graphene on Ru(10$\bar{1}$0).

Fig. 5.6 presents the LEED patterns of clean Ru(1,1,$\bar{2}$,10) (left) measured with different electron beam energies from 50 eV to 200 eV and Ru(1,1,$\bar{2}$,10) covered with graphene (right) obtained by heating the sample to 1400 K in 90 s, i.e. with the same procedure as used for Ru(0001) and Ru(10$\bar{1}$0). The spot splitting in the y-direction in the LEED patterns of clean Ru(1,1,$\bar{2}$,10) (left) is due to regular arrays of steps as discussed in detail in Chapter. 4. The satellite spots in the x-direction in the right patterns are caused by a Moiré structure with an approximate periodicity of 12 graphenes overlaid on 11 Ru atoms which is similar to the cases of Ru(0001) and Ru(10$\bar{1}$0). There is also an additional splitting of satellite spots visible in the LEED patterns of graphene on

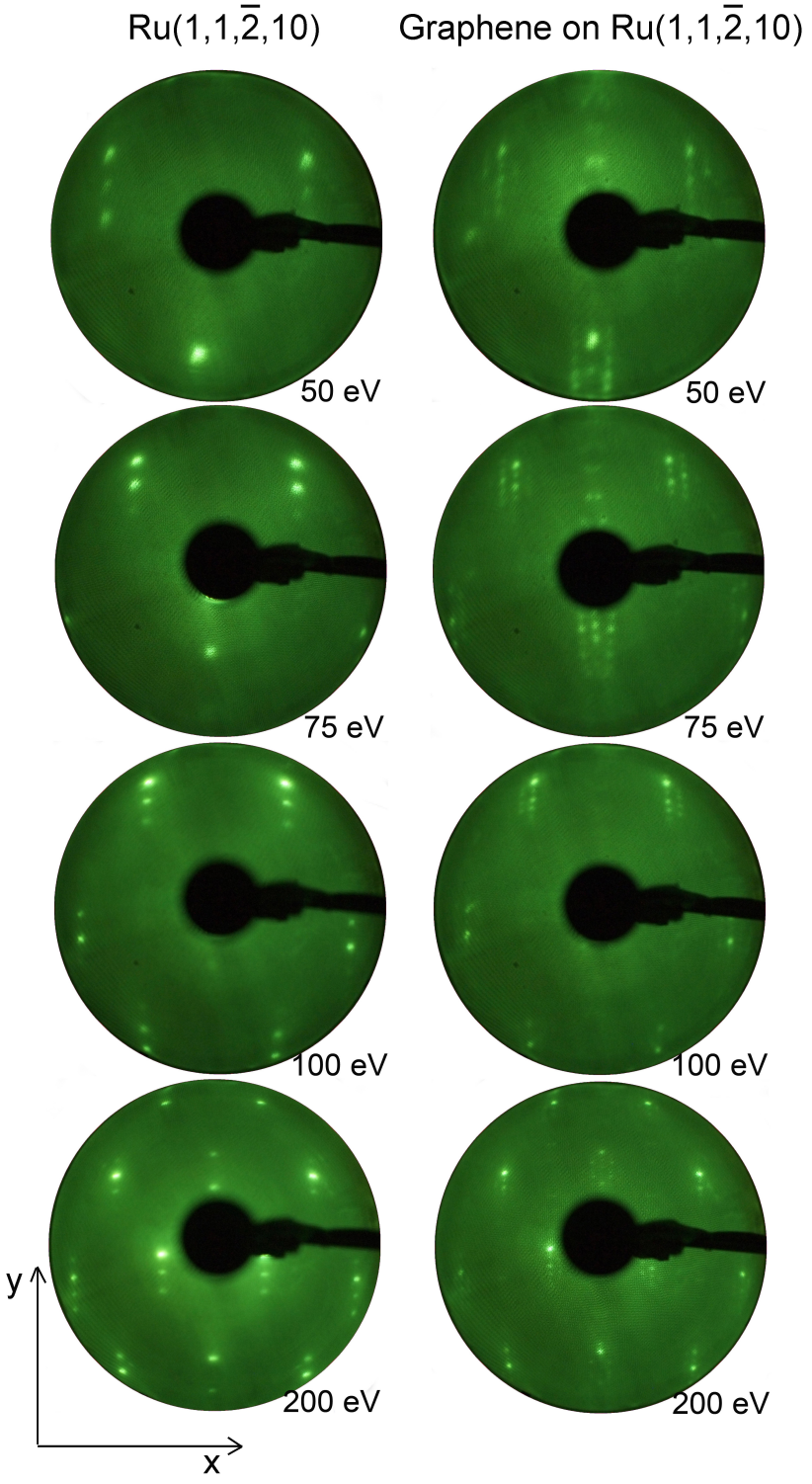

FIGURE 5.6: LEED patterns of clean Ru(1,1,$\bar{2}$,10) measured at 50 eV, 75 eV, 100 eV and 200 eV (left) and Graphene on Ru(1,1,$\bar{2}$,10) measured at 50 eV, 75 eV, 100 eV and 200 eV (right). The spot splitting in the left patterns in the y-direction is due to the regular arrays of steps. The satellite spots in the right patterns in the x-direction are caused by a Moiré structure with an approximate periodicity of 12 graphenes overlaid on 11 Ru atoms.

Ru(1,1,$\bar{2}$,10) which indicates that long-range well-ordered graphene nanoribbons were formed on the terraces of Ru(1,1,$\bar{2}$,10).

5.3 The bonding of graphene on Ru surfaces

Fig. 5.7 presents ARPES data measured at room temperature using He I_α excitation in the ΓM direction of (a) clean Ru(0001) and (b) graphene on Ru(0001) and in the ΓK direction of (a) clean Ru(0001) and (b) graphene on Ru(0001). For better visualization, the mapped ARPES data were divided into two areas with different color scales: one at low binding energy ($E_B < 6$ eV, where the Ru *4d* bands are located) and one at high binding energy ($E_B > 6$ eV, where the Ru *sp* and the graphene π-bands are located). The detailed electronic structure of Ru(0001) can be found in chapter 4. In Fig. 5.7(a) and (c) we can see two new features near the M and the K point which are denoted by $s1$ and $s2$ for the band in ΓM and in ΓK direction, respectively, which are not visible in Fig. 4.18 in chapter 4. The $s1$ and $s2$ bands can be attributed to the surface states predicted by Holzwarth *et. al.* [60]. At low binding energy ($E_B < 6$ eV), the main peaks are the Ru *4d* bands [16] which can be observed in both the mapped ARPES data of clean Ru(0001) and graphene on Ru(0001). In Fig. 5.7(b) we can see that some bands are more pronounced than those in Fig. 5.7(a), like the Ru *sp* band at about 5 eV. This is maybe because of the aspect ratio of color scale in both the mapped ARPES data of clean Ru(0001) and graphene on Ru(0001). Keep in mind that the bands of clean Ru(0001) and graphene on Ru(0001) are mapped by ARPES which means we measured the bands at different angles and then combined them to get the ARPES data. It took a long time to measure these bands, so possibly during the measurement a contamination occurred which was absorbed onto Ru(0001) but not onto the graphene on Ru(0001) (graphene is stable in air [56]). The result would be that some bands of Ru(0001) are less pronounced than that of graphene on Ru(0001). This would mean that a graphene layers is a very good candidate to protect surfaces or can be used as a capping layer to protect mirrors in EUVL. The graphene π-band is observed as a dispersing band of weak intensity with a binding energy of about 10 eV at the Γ point in Fig. 5.7(b) and (d). The theoretical graphene π-band had to be shifted by 1.7 eV to higher binding energy compared to free-standing graphene in order to be superimposed on the experimental band. The dashed black line is the π-band of graphene on Ru(0001). The effective mass of the π-band of graphene on Ru(0001) in a parabolic approximation around Γ is about 1.4 m_e which is larger than that of free-standing graphene (1.3 m_e [116]). The shift of the π-band of graphene on Ru(0001) indicates that there is strong bonding between graphene and Ru surfaces. It is consistent with previous electronic and surface structure measurements [100, 117–119] which shows that there is a transfer of charges between

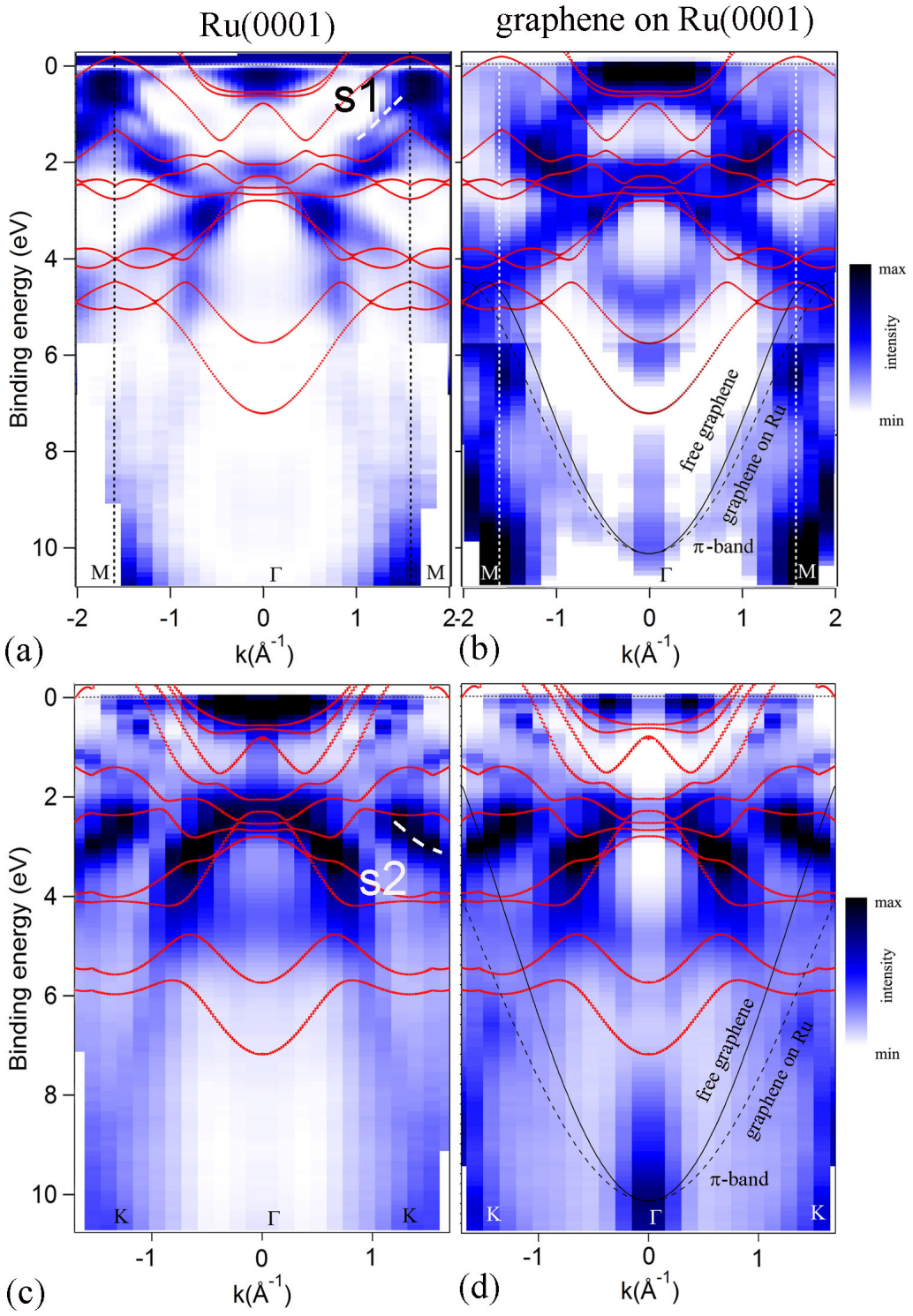

FIGURE 5.7: ARPES data measured at room temperature using He I_α excitation of (a) clean Ru(0001) and (b) graphene on Ru(0001) in the ΓM direction, and (c) clean Ru(0001) and (d) graphene on Ru(0001) in the ΓK direction. For better visualization the mapped ARPES data were divided into two areas with different color scales: one at low binding energy ($E_B < 6$ eV, where the Ru *4d* bands are located) and one at high binding energy ($E_B > 6$ eV, where the Ru *sp* and the graphene π-bands are located). The dotted red lines are the theoretical bands of Ru(0001) [16]. The solid black line is the theoretical band of free-standing graphene [115], the π-band is shifted by 1.7 eV to higher binding energy. The dashed black line is the π-band of graphene on Ru(0001).

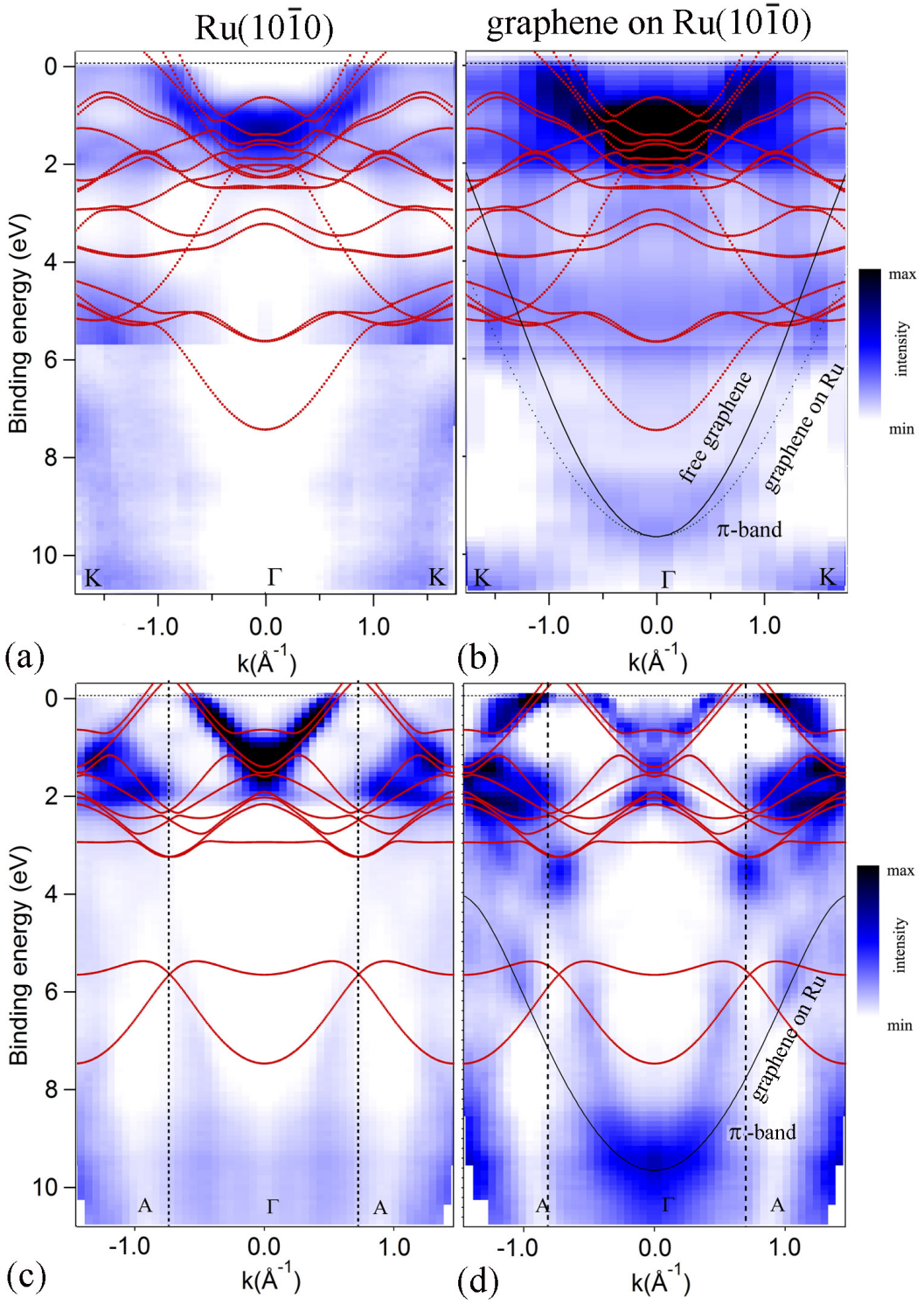

FIGURE 5.8: ARPES data measured at room temperature using He I_α excitation of (a) clean Ru(10$\bar{1}$0) and (b) graphene on Ru(10$\bar{1}$0) in the ΓK direction, and (c) clean Ru(10$\bar{1}$0) and (d) graphene on Ru(10$\bar{1}$0) in the ΓA direction. For better visualization the mapped ARPES data were divided into two areas with different color scales. The dotted red lines are the theoretical bands of Ru(0001) [16]. The solid black line is the theoretical band of free-standing graphene [115], the π-band is shifted by 1.3 eV to higher binding energy. The dashed black line is the π-band of graphene on Ru(10$\bar{1}$0).

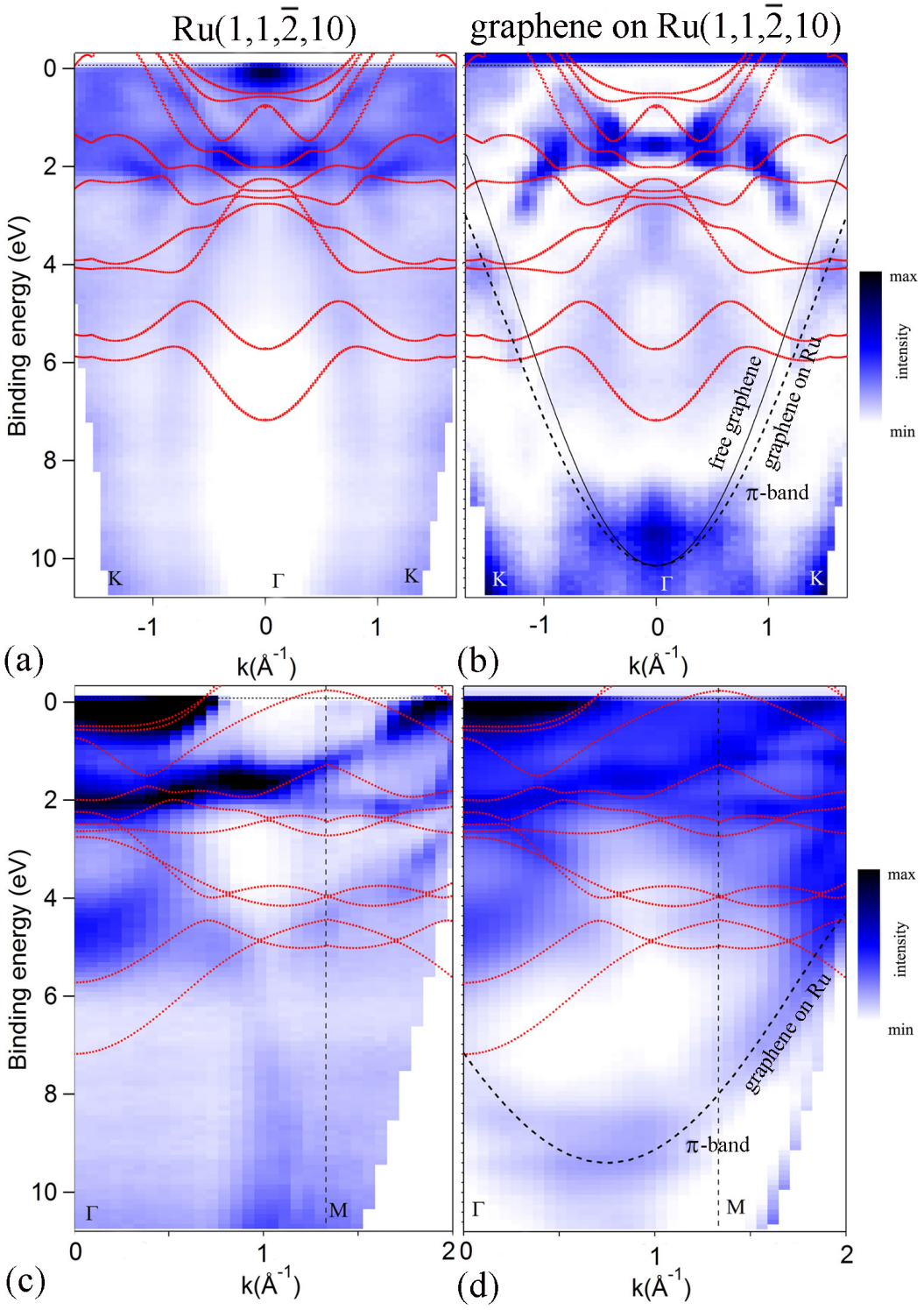

FIGURE 5.9: ARPES data measured at room temperature using He I_α excitation of (a) clean Ru(1,1,$\bar{2}$,10) and (b) graphene on Ru(1,1,$\bar{2}$,10) in the direction parallel to the step edge, i.e. the ΓK direction, and (c) clean Ru(1,1,$\bar{2}$,10) and (d) graphene on Ru(1,1,$\bar{2}$,10) in the direction perpendicular to the step edge, i.e. the ΓM direction. The dotted red lines are the theoretical bands of Ru(0001) [16]. The solid black line is the theoretical band of free-standing graphene [115], the π-band is shifted by 1.7 eV to higher binding energy. The dashed black line is the π-band of graphene on Ru(1,1,$\bar{2}$,10).

graphene and Ru(0001) leading to a strong hybridization between the graphene π orbital and the Ru 4*d* orbitals.

In the experimental ARPES data of graphene on Ru(10$\bar{1}$0) shown in Fig. 5.8 there is evidence of additional bands with respect to clean Ru(10$\bar{1}$0). For better visualization the mapped ARPES data also were divided into two areas with different color scales. The additional band of graphene is very similar to the π-bands of graphene on Ru(0001) but an energy shift of 1.3 eV is necessary to achieve a match with the theoretical data of free-standing graphene. The effective mass of the π-band of graphene on Ru(10$\bar{1}$0) in a parabolic approximation around Γ is also about 1.4 m_e. From the ARPES data we conclude that the bonding of graphene to Ru(0001) and to Ru(10$\bar{1}$0) is very similar. Both systems belong to the strongly bonding regime in which the graphene π-band is shifted by 1.3–1.7 eV.

Fig. 5.9 presents ARPES data measured at room temperature using He I_α excitation of (a) clean Ru(1,1,$\bar{2}$,10) and (b) graphene on Ru(1,1,$\bar{2}$,10) in the direction parallel to the step edge, i.e. the ΓK direction, and (c) clean Ru(1,1,$\bar{2}$,10) and (d) graphene on Ru(1,1,$\bar{2}$,10) in the direction perpendicular to the step edge, i.e. the ΓM direction. Similar to the case of graphene on Ru(0001) and Ru(10$\bar{1}$0) we observe that the π-bands of graphene on Ru(1,1,$\bar{2}$,10) are shifted by about 1.7 eV to higher binding energies with respect to free-standing graphene. However, there are differences between the π-bands of graphene in the ΓK direction and the ΓM direction due to the additional periodicity of the step array in one dimension. The band structure of graphene on Ru(1,1,$\bar{2}$,10) in the direction parallel to the step edge is similar to that of graphene on Ru(0001). In the direction perpendicular to the step edge, the minimum position of the π-bands of graphene is shifted not only to higher binding energy by about 1.7 eV but also to a higher wave vector about 0.75 $Å^{-1}$ which is about $2G = 4\pi/D$ where G indicates a reciprocal superlattice vector. The shift is due to Umklapp scattering while the wave vector transfer G is characteristic of the superlattice structure [71].

5.4 Summary

Well-ordered graphene can be prepared on three surfaces of different symmetry: Ru(0001), Ru(10$\bar{1}$0) and Ru(1,1,$\bar{2}$,10). The π-band of graphene is shifted by about 1.3–1.7 eV with respect to free-standing graphene on all Ru surfaces. Therefore the bonding of graphene with Ru(0001), Ru(10$\bar{1}$0) and Ru(1,1,$\bar{2}$,10) is very similar. Graphene interacts strongly with three Ru surfaces.

Chapter 6

CuPc on graphene/Ru surfaces

6.1 Introduction

Several groups studied MePc on highly oriented pyrolytic graphite (HOPG) [120–132] and on graphene [24, 25, 133–141]. Graphene is a single sheet of graphite and the outer sheet of a bilayer of graphene has essentially the same electronic structure as free-standing monolayer graphene [142]. Therefore, the bonding and orientation of MePc on HOPG and on graphene are presumably very similar. The influence of the graphene substrate on MePc is expected to be very small, like it is the case for a HOPG substrate [56]. Depending on how graphene is grown on metal substrates, the graphene will possess different geometric structures which will affect the arrangement of the MePc molecules. Graphene on metal surfaces can be divided in two categories: lattice-matched, such as graphene on Ni(111) [56], and lattice-mismatched, such as graphene on Ru(0001) [16]. A lattice mismatch leads to a Moiré structure of graphene on Ru(0001) [16]. If the periodicity of the Moiré structure coincides with the lattice parameters of an adsorbate layer, the Moiré structure can aid in the alignment and induce preferred adsorption sites and, consequently, particular adsorption patterns may be obtained [56]. Until now the interaction of MePc molecules with the metal-supported graphene is still controversial. As reported by Gao *et al.* [25], FePc, NiPc and H_2Pc molecules on graphene/Ru(0001) have similar special Kagome structures which adapt to the lattice of the Moiré pattern of graphene. An effect of the metal atom in the MePc has not been found by comparing FePc, NiPc and H_2Pc. However, CoPc and FePc molecules on the Moiré pattern of Graphene/Ir(111) form well-ordered domains with nearly square unit cells [133, 137, 138]. Dou *et al.* [24] studied several different MePc on graphene/Ni(111) and found that depending on the metal the bonding of the molecules with graphene is different. For

Me = Ni, Cu, Zn, the bonding of MePc with graphene/Ni(111) is weak like a π-π bonding between molecules, while for Me = Fe and Co, the bonding is stronger.

In this chapter I present a detailed study of CuPc on Ru surfaces and on graphene/Ru surfaces. The results show that ordered structures are formed when CuPc is deposited on Ru(10$\bar{1}$0) but they are not formed when it is deposited on Ru(0001). The study is focused on clarifying how the Moiré structures of the graphene on Ru(10$\bar{1}$0) and on Ru(0001) affect the adsorption of CuPc molecules.

6.2 CuPc on Ru(10$\bar{1}$0)

6.2.1 Geometric properties of CuPc on Ru(10$\bar{1}$0)

Fig. 6.1 shows the LEED patterns of CuPc on Ru(10$\bar{1}$0) with different thicknesses from 1.0 ML to 6.7 ML as labeled in the figure measured with an electron beam energy (E_o) of 15 eV. On the left-hand side are the measured LEED patterns and on the right-hand side are the measured LEED patterns with red circles representing the LEED patterns fitted by using the Spot-Plotter software [143]. Obviously the CuPc molecules can be grown with a very well-ordered structure on Ru(10$\bar{1}$0) from monolayer to multilayers. The LEED patterns are almost the same for all CuPc thicknesses. The differences in the LEED patterns cannot be distinguished due to the distortion of the patterns when low-energy electrons were used. The LEED patterns fitted by using the Spot-Plotter software [143] show two adsorbate domains of CuPc on Ru(10$\bar{1}$0) represented in Fig. 6.2(a). The red and blue circles indicate the two adsorbate domains and the adsorbate reciprocal-lattice unit cells are shown by solid lines. The best real structure of CuPc overlayer on Ru(10$\bar{1}$0) proposed is shown in Fig. 6.2(b). The superstructure matrix is M=$\begin{bmatrix} 5 & 1 \\ 2 & -3 \end{bmatrix}$ with respect to Ru(10$\bar{1}$0). There are two equivalent domains in which the distance between adjacent CuPc molecules is $a = 14.2$ Å and $b = 13.9$ Å. Both structures are drawn with respect to the ideal surface. The CuPc molecules form well-ordered domains with almost square unit cells which is in good agreement with MePcs on HOPG [120, 122] and also on the Moiré pattern of graphene on Ir(111) [133, 137, 138]. These results indicate that the interaction of CuPc with the Ru(10$\bar{1}$0) substrate is sufficiently weak to enable lateral diffusion of CuPc leading to ordered structures on Ru(10$\bar{1}$0).

6.2.2 The bonding of CuPc on Ru(10$\bar{1}$0)

Shown in Fig. 6.3 are the XPS-spectroscopic data of CuPc molecules on Ru(10$\bar{1}$0) at different thicknesses from 1.0 ML to 6.7 ML. Using the QUASES software, all data were

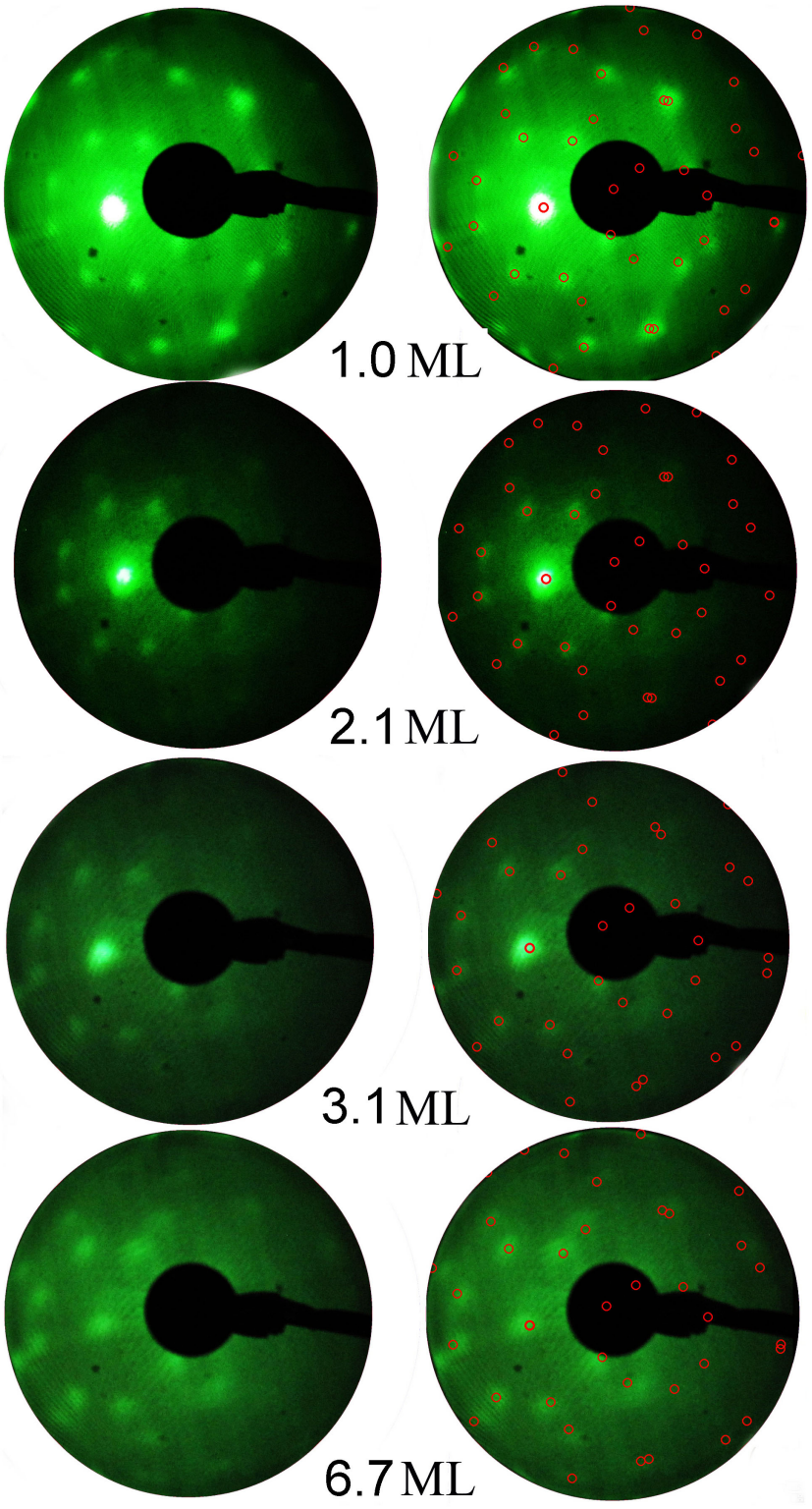

FIGURE 6.1: LEED patterns of CuPc on Ru(10$\bar{1}$0) with different thicknesses from 1.0 to 6.7 ML recorded with electron beam energy E_o = 15 eV. On the left-hand side are the measured LEED patterns and on the right-hand side are the measured LEED patterns with red circles representing the LEED patterns fitted by using the Spot-Plotter software [143]. CuPc molecules can be grown with a very well-ordered structure on Ru(10$\bar{1}$0) from monolayer to multilayers.

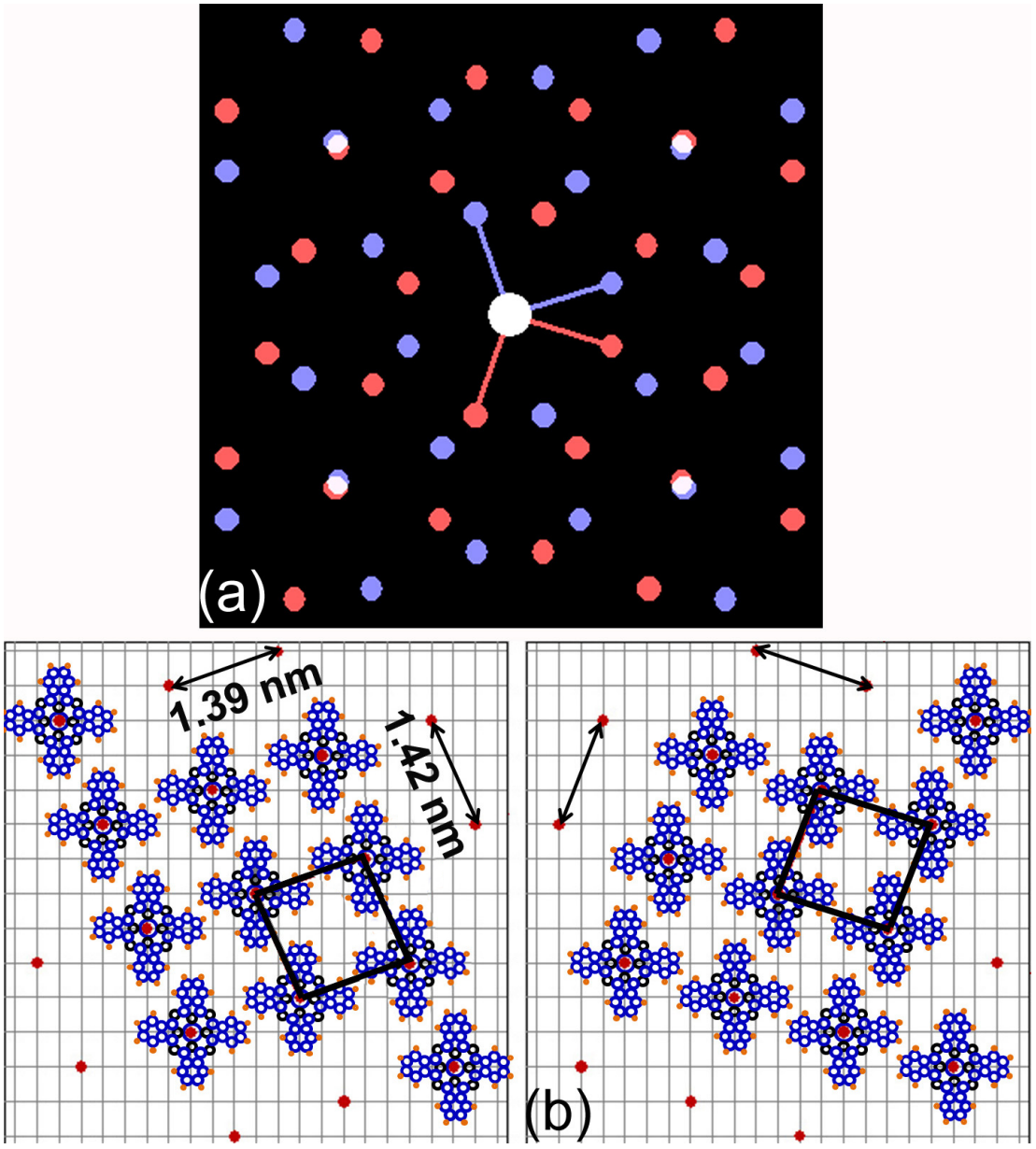

FIGURE 6.2: (a) Schematic LEED pattern withthe two adsorbate domains of CuPc on Ru(10$\bar{1}$0). Red and blue circles indicate the two adsorbate domains. Adsorbate reciprocal-lattice unit cells are shown by solid lines. (b) The proposed structure of CuPc on Ru(10$\bar{1}$0). There are two equivalent domains of CuPc on Ru(10$\bar{1}$0) in which the distance between adjacent CuPc molecules is $a = 14.2$ Å and $b = 13.9$ Å.

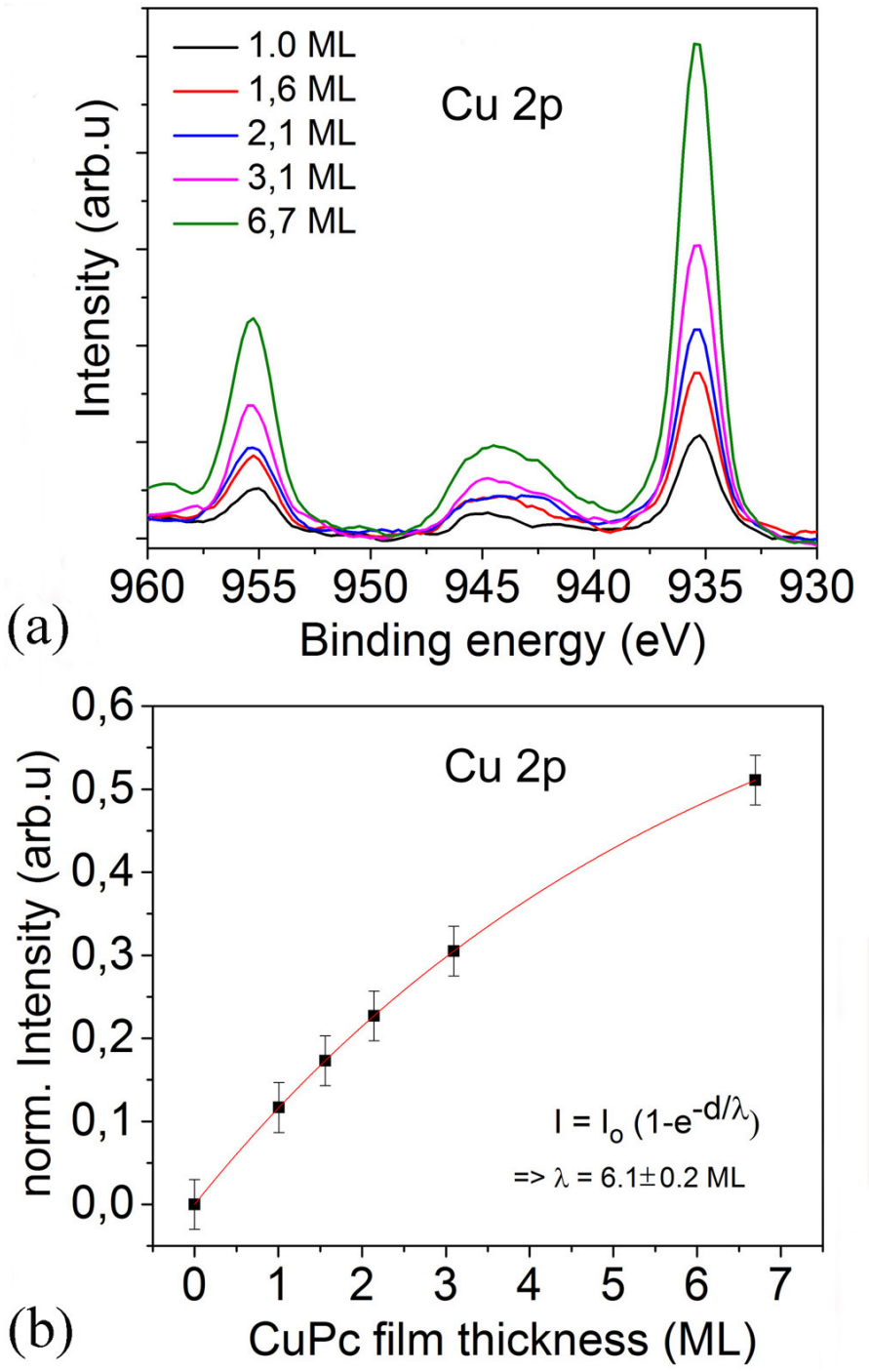

FIGURE 6.3: XPS spectroscopy of CuPc molecules on Ru($10\bar{1}0$) with different coverages: (a) Cu 2p PES signal, all data were background-corrected and normalized using the QUASES software as described by Tougaard's method [144], (b) Normalized intensity the of Cu 2p PES signal plotted against the CuPc thickness. The solid red line is fitted to the data using an exponential function. The estimated effective attenuation length of electrons is $\lambda(E) = 6.1$ ML at a kinetic energy of 1069 eV.

background-corrected and normalized as described by Tougaard's method [144]. The solid red line in Fig. 6.3(b) was fitted to the data using an exponential function. The simplest description of the dependence of the normalized intensities of CuPc on the thickness of the layer is an exponential law:

$$I = I_o \exp(1 - \frac{d_c}{\lambda(E)\cos\theta}) \tag{6.1}$$

where I_o is the intensity of an infinitely thick layer of CuPc, θ is the emergent angle of the photoelectrons ($\theta = 0°$), $\lambda(E)$ is the effective attenuation length of electrons in the CuPc film. The exponential function given in equation (6.1) is fitted to the data. The estimated effective attenuation length of electrons is $\lambda(E) = 6.1$ ML at a kinetic energy of 1069 eV. The result is in good agreement with previous studies of CuPc and PTCDA [145]. There are no significant differences in the binding energies of Cu 2p at different coverages. The binding energies of Cu 2p in a monolayer and in multilayers of CuPc are similar. This means that there is no charge transfer from Ru(10$\bar{1}$0) to the CuPc molecules and that the interaction between CuPc and Ru(10$\bar{1}$0) is weak. This is consistent with the LEED pattern of CuPc on Ru(10$\bar{1}$0).

From the LEED patterns, the morphology of the CuPc molecules on Ru(10$\bar{1}$0) cannot be determined. The LEED patterns of CuPc films of different thicknesses are almost the same, so the CuPc molecules probably only form islands. The LEED patterns of CuPc multilayers just come from the first layer. The study of H_2Pc films on single-crystal surfaces of Ag(111) and of Ni_3Al(111) by Kera *et al.* [147] shows that the H_2Pc-Ag(111) films form islands and the H_2Pc-Ni_3Al(111) films form several wetting layers and the molecules are tilted by about 0–60° depending on the deposition temperature. For a thorough understanding of the morphology of CuPc molecules on Ru(10$\bar{1}$0), the samples were studied in detail with angle-resolved X-ray photoelectron spectroscopy (ARXPS) measurement. First, we need to know the growth mechanisms of organic thin films, which can be subdivided into three different types [146]. Fig. 6.5 shows the three growth modes of molecules on a substrate with different coverages t_{CuPc} in ML: (a) Volmer-Weber or island growth, (b) Stranski-Krastanov or layer-plus-island growth, (c) Frank-van der Merwe or layer-by-layer growth. The growth models of the molecules will be determined by the strength of the attraction between the atoms of molecules themselves and between the atoms and the substrate. If the attraction between the atoms of molecules is stronger than that between the atoms and the substrate, the Volmer-Weber or island growth occurs. In the opposite case, the interaction between the atoms and the substrate is stronger than that between atoms themselves, the Frank-van der Merwe or layer-by-layer growth results. In an intermediate case, the growth mode is the Stranski-Krastanov or layer-plus-island. Fig. 6.4 shows the XPS spectroscopic data

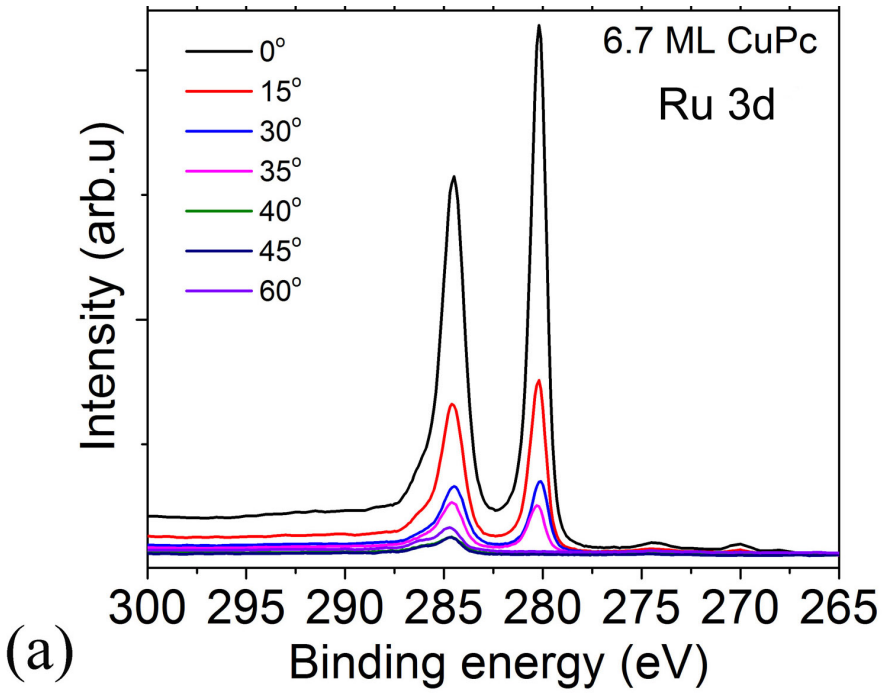

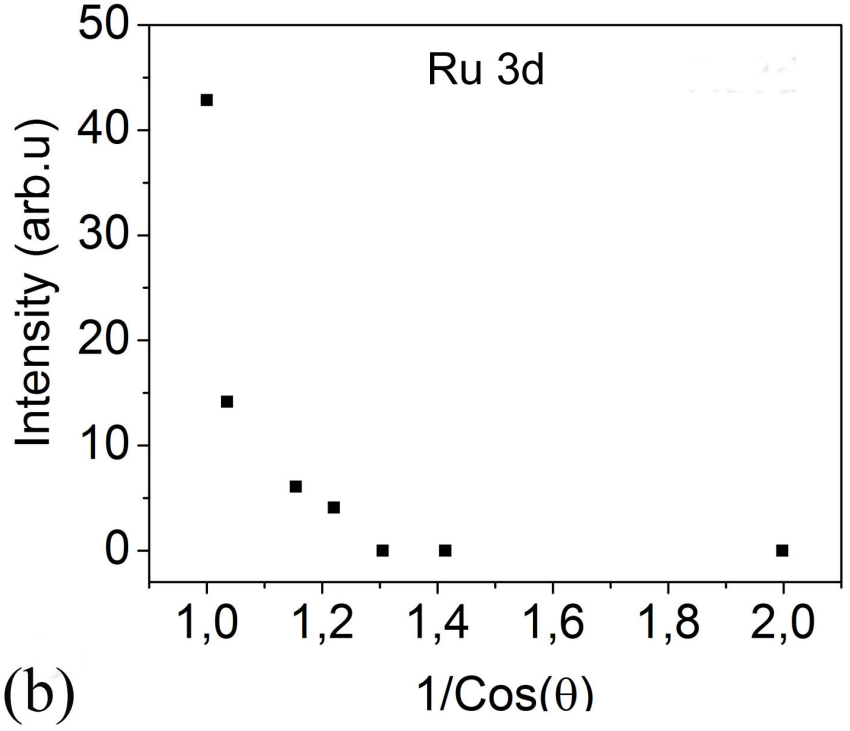

FIGURE 6.4: XPS spectroscopy of CuPc molecules on Ru($10\bar{1}0$) measured at different angles from $\theta = 0°$ to 60°. (a) Ru 3p PES signal, all data were background-corrected and normalized using the QUASES software as described by Tougaard's method [144]. (b) Normalized intensity of the Ru 3d PES signal plotted against the angle.

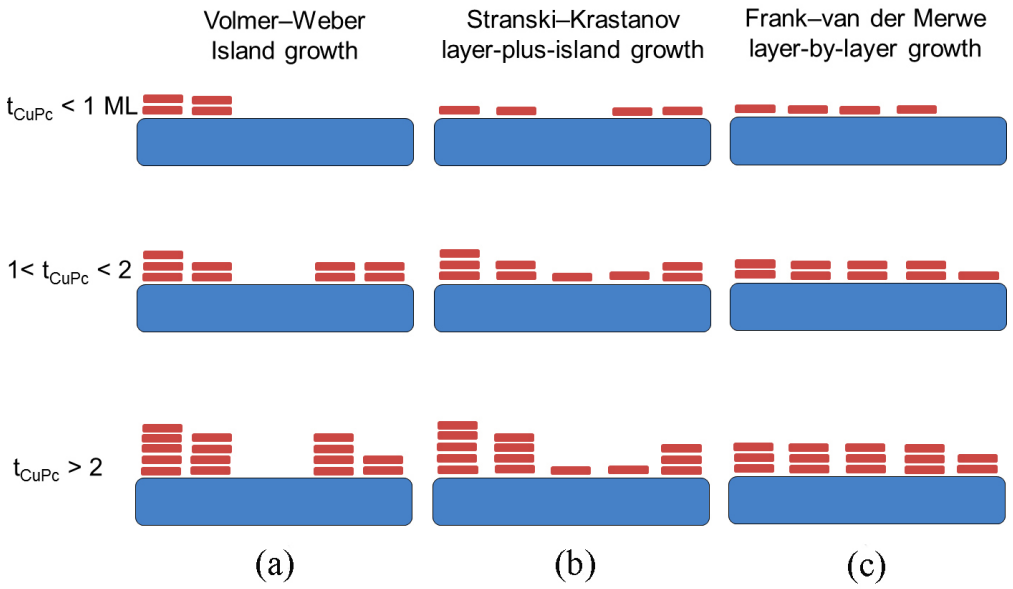

FIGURE 6.5: Three growth modes of molecules on a substrate with different coverages t_{CuPc} in ML: (a) Volmer-Weber or island growth, (b) Stranski-Krastanov or layer-plus-island growth, (c) Frank-van der Merwe or layer-by-layer growth (adapted from Ref. [146]).

of 6.7 ML of CuPc molecules on Ru(10$\bar{1}$0) measured at different angles from $\theta = 0°$ to 60°. When the measuring angles are larger than 40°, there is no signal from Ru 3d. The thickness of the CuPc layers is very small compared with the diameter of the Ru substrate, so the effect of shadow in ARPES can be neglected. The result indicates that the CuPc cannot be grown according to a Volmer-Weber or island model. If the CuPc molecules grow on Ru(10$\bar{1}$0) according to a Frank-van der Merwe or layer-by-layer model, the dependence of the normalized intensities of Ru 3d on the angle would be described by an exponential law:

$$I = I_o \exp(\frac{d_c}{\lambda(E)\cos\theta}) \tag{6.2}$$

Fig. 6.4(b) shows the dependence of the intensities of Ru 3d on $1/\cos(\theta)$. The dependence does not follow an exponential law. This means that the CuPc molecules do not grow layer by layer on Ru(10$\bar{1}$0). Therefore, the CuPc molecules grow according to the Stranski-Krastanov or layer-plus-island model on Ru(10$\bar{1}$0). To get more information about the morphology of CuPc on Ru(10$\bar{1}$0), the QUASES software with the universal loss function as described by Tougaard's method [144] is used. For a meaningful analysis of the peak intensities, we have to assume that the samples are homogeneous [148]. From the LEED patterns in Fig. 6.1 we know that CuPc molecules grow with a well-ordered structure on Ru(10$\bar{1}$0). If we do not know the surface morphology, a

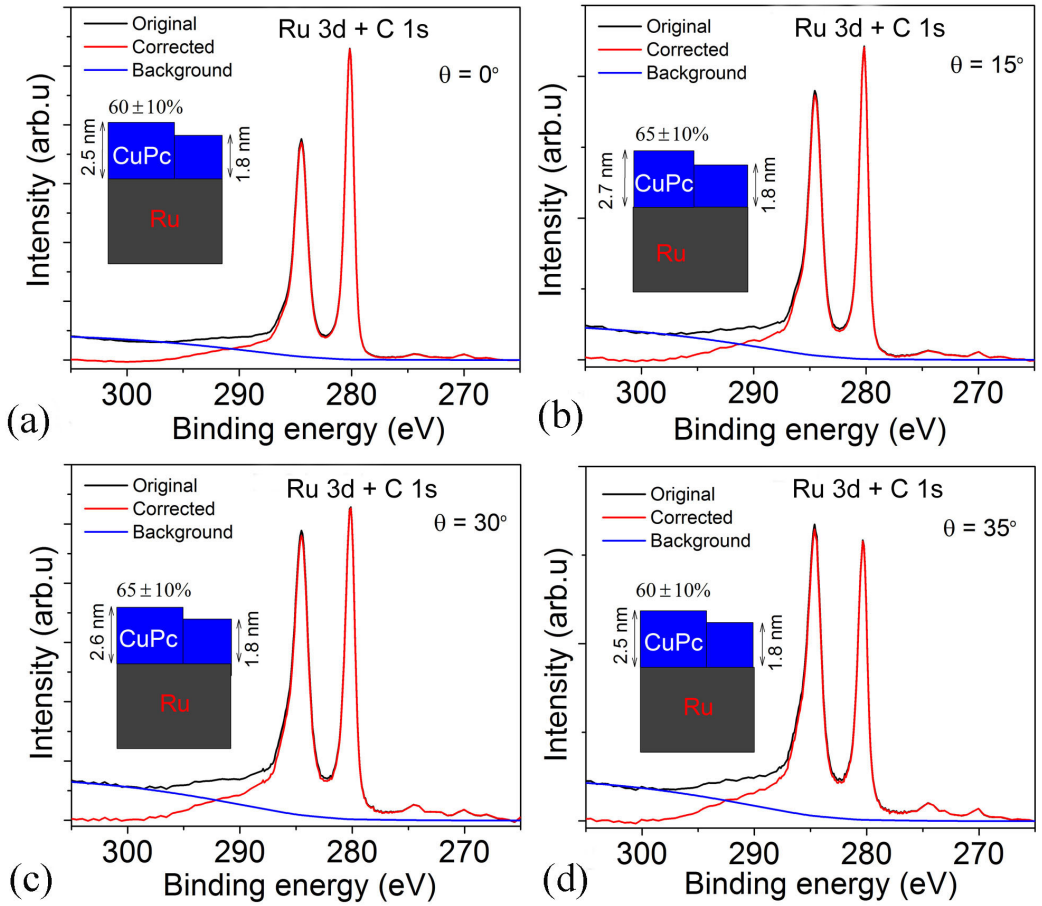

FIGURE 6.6: XPS spectroscopic data of CuPc molecules on Ru(10$\bar{1}$0) measured at different angles from $\theta = 0°$ to 60°. (a), (b), (c) and (d) Ru 3p PES signal measured at $\theta = 0°$, 15°, 30° and 35°, respectively. The morphology of CuPc was established by using the QUASES software [144] with the universal loss function to get the peak share or the background fitting the measured data best.

quantification based on peak intensities might cause enormous errors [148]. By analyzing the peak shape of Ru 3d, we can get more information about the CuPc morphology on Ru(10$\bar{1}$0). Depending on the surface morphology of CuPc, electrons move with a different path length and, thus, change the peak shape of Ru 3d [149, 150]. Fig. 6.6 shows the XPS spectroscopic data of CuPc molecules on Ru(10$\bar{1}$0) measured at different angles from $\theta = 0°$ to 60°. (a), (b), (c) and (d) show the Ru 3p PES signal measured at $\theta = 0°$, 15°, 30° and 35°, respectively. The morphology of CuPc is established to get the peak share or the background fitting the measured data best. The morphology of CuPc can roughly be estimated, which leads to the conclusion that CuPc grows according to a Stranski-Krastanov or layer-plus-island model with 60 ± 10 % of the surface being 2.6 ± 0.1 nm thick and the rest of the surface being 1.8 ± 0.1 nm thick.

Expanded C 1s spectra of 6.7 ML of CuPc molecules on Ru(10$\bar{1}$0) measured at $\theta = 60°$ are presented in Fig. 6.7. The data were background-corrected and normalized using

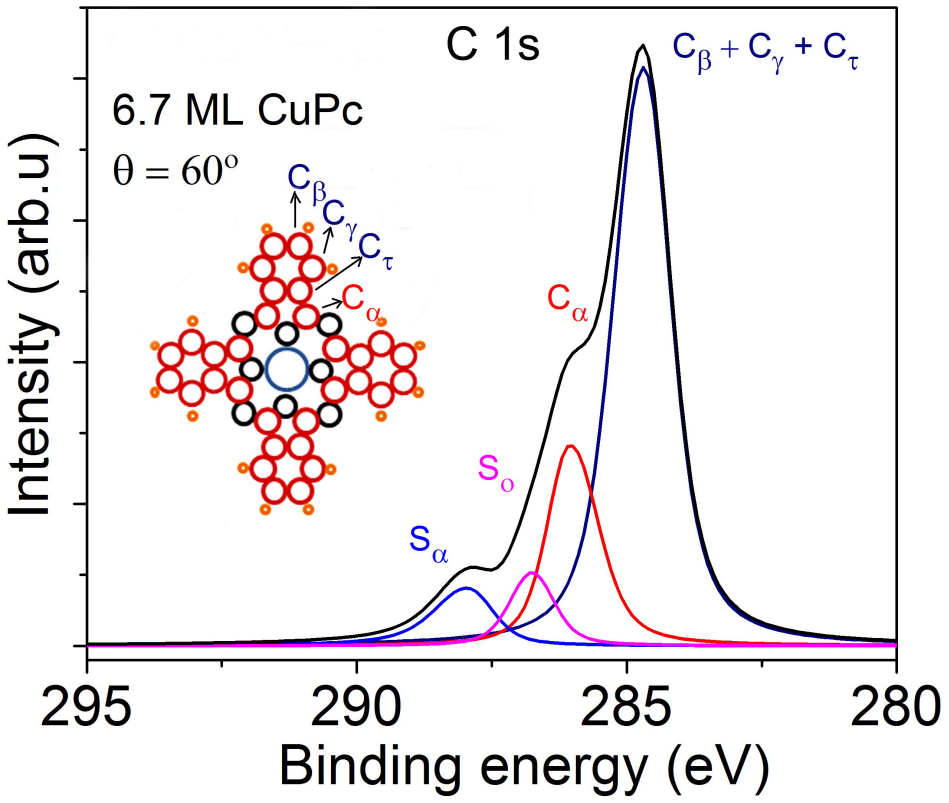

FIGURE 6.7: Expanded C 1s spectra of CuPc molecules on Ru(10$\bar{1}$0) measured at $\theta = 60°$. The data were background-corrected and normalized using the QUASES software as described by Tougaard's method [144].The inset illustration shows the schematic structure of CuPc with differently denoted carbons corresponding to the peaks in the spectra.

the QUASES software as described by Tougaard's method [144]. The inset illustration shows the schematic structure of CuPc with differently denoted carbons corresponding to the peaks in spectra. The black curve represents the measured data, the other curves represent data fitted by using pseudo-Voigt functions. It can be seen that there are four different main peaks related to different carbons with binding energy 284.7 eV, 286.1 eV, 286.8 eV and 287.8 eV, respectively. These features are similar to that of the phthalocyanine on other substrates [137, 151–153]. The peak at 284.7 eV binding energy is assigned to the atoms of benzene rings (C_β, C_γ and C_τ). Photoemission from C_α of the pyrrole ring occurs at a higher ionization energy (286.1 eV) compared to that of atoms of the benzene rings [153]. The peaks at 286.8 eV and 287.8 eV binding energy are satellites resulting from a HOMO-LUMO transition [137].

As shown in previous chapters, in the region of the valence band of a Ru surface it is difficult to distinguish the CuPc molecular features when CuPc molecules were prepared on Ru surfaces because there are a lot of features of Ru. Therefore, the valence band of CuPc with different thicknesses was measured at different angles, i.e. $\theta = 0°$, 15°, 30°, 45° and 60°, as illustrated in Fig. 6.9. The main features of CuPc molecules are

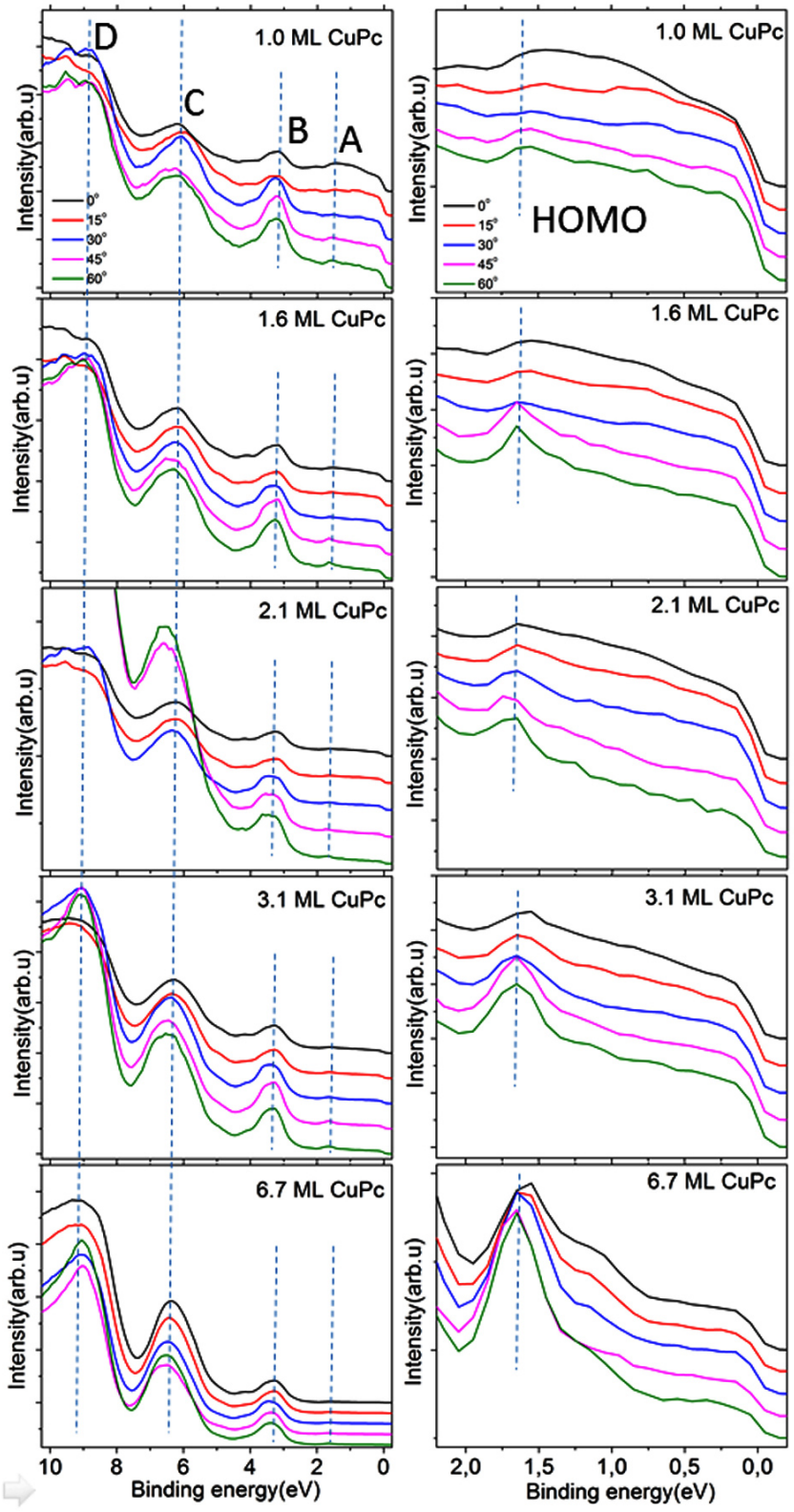

FIGURE 6.8: He 1_α UPS spectra of CuPc films on Ru(10$\bar{1}$0) with different thicknesses from 1.0 ML to 6.7 ML as labeled in the figure and measured with different angles, $\theta = 0°$, 15°, 30°, 45° and 60°. The main features of CuPc molecules are denoted by A-D.

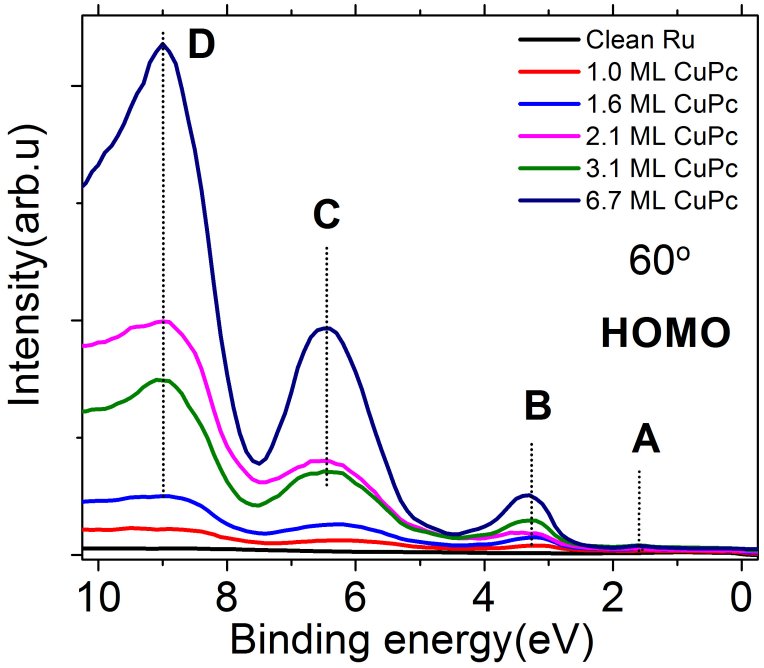

FIGURE 6.9: He 1_α UPS spectra of CuPc films on Ru(10$\bar{1}$0) with different thicknesses from 1.0 ML to 6.7 ML. The spectra were measured at an angle of $\theta = 60°$. On the right-hand side is the expanded spectrum at low binding energy, close to the Fermi level. The main features of CuPc molecules are denoted by A - D.

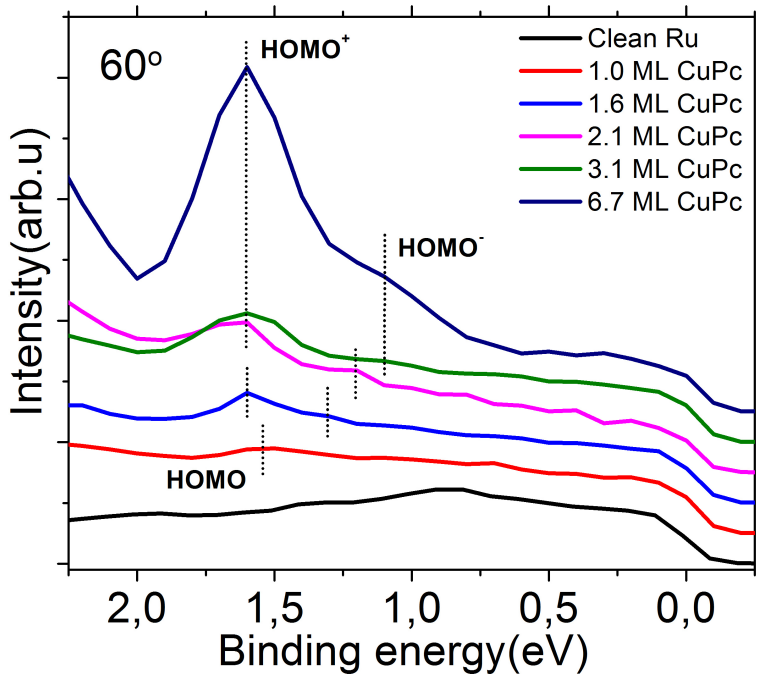

FIGURE 6.10: Expanded spectra of the HOMO region of He 1_α UPS spectra of CuPc films on Ru(10$\bar{1}$0) with different thicknesses from 1.0 ML to 6.7 ML. The spectra were measured at an angle of $\theta = 60°$. $HOMO^+$ and $HOMO^-$ which are denoted in the spectra of thick layers of CuPc arise from the splitting of the HOMO in a ML of CuPc.

denoted by A–D. The binding energies of states A, B, C and D are 1.6 eV, 3.3 eV, 6.4 eV and 9.0 eV, respectively. There are no significant differences of the valence bands of CuPc at various measured angles. The only difference is feature C in which the state is dispersive. But this state is a superposition of states of CuPc and the *sp* band of Ru(10$\bar{1}$0). There is also no significant difference between the valence bands of CuPc films of different thickness, as shown in Fig. 6.9 in which the spectra were measured at an angle of $\theta = 60°$. The main features of CuPc molecules denoted by A–D are observed in all CuPc molecular films. These features of CuPc films are similar to that of PbPc on HOPG [123, 127, 154]. Peak A at binding energy 1.6 eV is assigned to the HOMO which is related to the porphine-like ring. Feature B at binding energy 3.3 eV is arising from the outer four benzene rings and features C and D are related to many π and σ states [123].

For a thorough understanding of the bonding between CuPc and Ru(10$\bar{1}$0), the expanded spectra at low binding energy, close to the Fermi level of the HOMO region of CuPc films with different thicknesses from 1.0 ML to 6.7 ML are shown in Fig. 6.10. It can be seen that in a monolayer of CuPc there is a state at binding energy 1.53 eV which is denoted as the HOMO of CuPc. When we increase the thickness of CuPc, there are two states which appear in the HOMO region. The HOMO peak is split into HOMO$^+$ and HOMO$^-$ with an energy separation of 0.35 eV. This splitting does not come from the two domains of CuPc on Ru(10$\bar{1}$0) because in the XPS spectra of CuPc molecules there is no splitting of the Cu 2p peaks. This phenomenon is also observed in other systems, such as PbPc on HOPG [123, 127], SnPc on Ag(111) [155], and SnPc on PTCDA on Ag(111) [156]. Kera *et al.* [127] explained the splitting of the HOMO peak as due to weak inter-orbital interactions (the π-π interaction) which leads to a hybridization of the respective HOMOs and forms bonding and anti-bonding orbitals in the dimer structure of the bilayer. This only happens when the thickness of the phthalocyanine molecules is larger than a monolayer. Then they form stacked molecules within very well-ordered films.

6.3 CuPc on graphene/Ru(10$\bar{1}$0)

6.3.1 Geometric properties of CuPc on graphene/Ru(10$\bar{1}$0)

Deposition of CuPc on graphene/Ru(10$\bar{1}$0) is expected to be very similar to deposition on Ru(10$\bar{1}$0). In both Ru(10$\bar{1}$0) and graphene/Ru(10$\bar{1}$0), the influence of the substrate on CuPc is very small. Nevertheless, the Moiré-structure of graphene on Ru(10$\bar{1}$0) will affect the arrangements of CuPc molecules. In Fig. 6.11 it is obvious that CuPc molecules

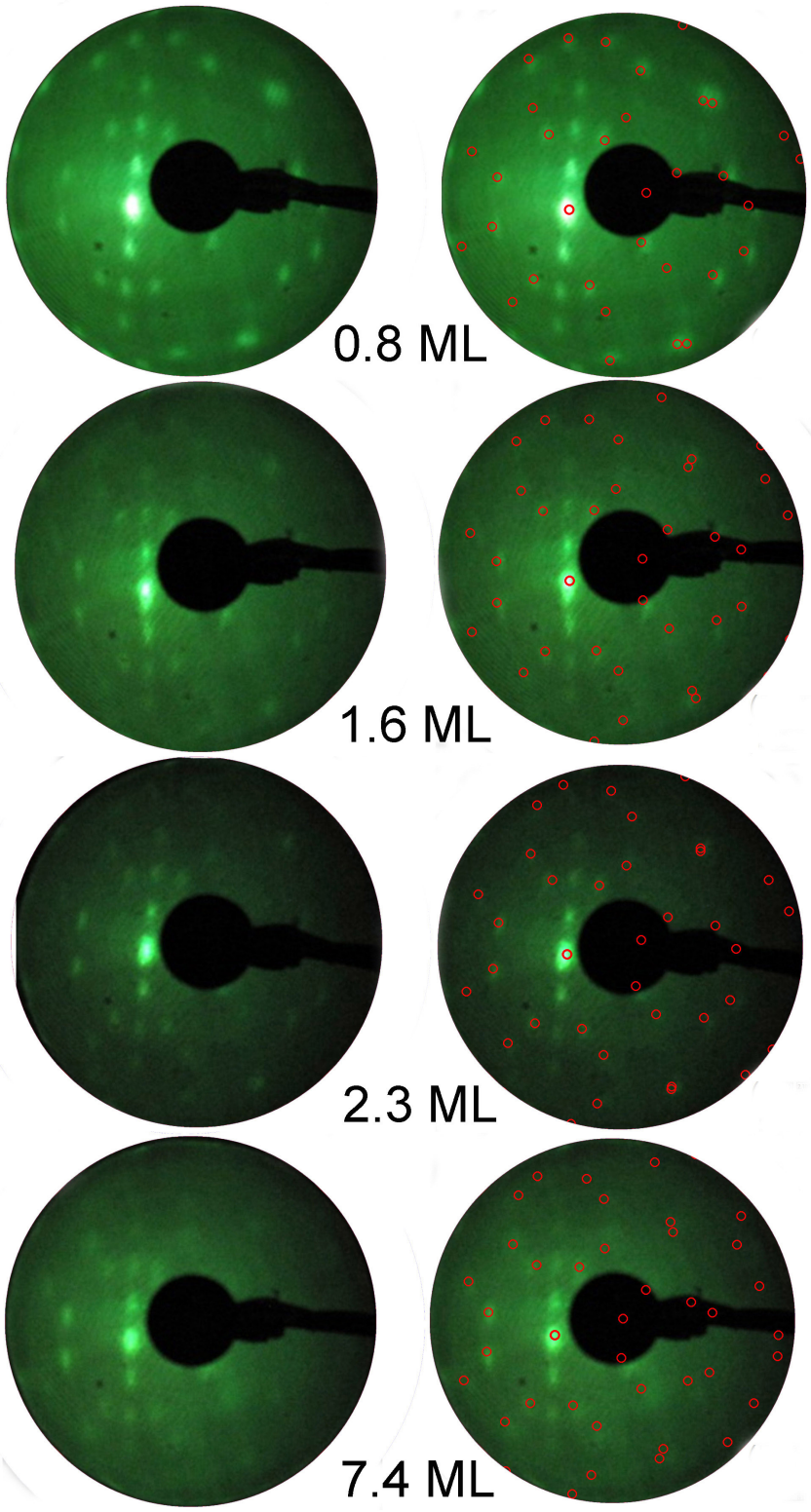

FIGURE 6.11: LEED patterns of CuPc on graphene/Ru($10\bar{1}0$) with different thicknesses from 0.8 ML to 7.4 ML as labeled in the figure recorded with an electron beam energy (E_o) of 15 eV. On the left-hand side are measured LEED patterns and on the right-hand side are measured LEED patterns with red circles representing the LEED patterns fitted by using the Spot-Plotter software [143]. CuPc molecules can be grown with a very well-ordered structure on graphene/Ru($10\bar{1}0$) from monolayer to multilayers.

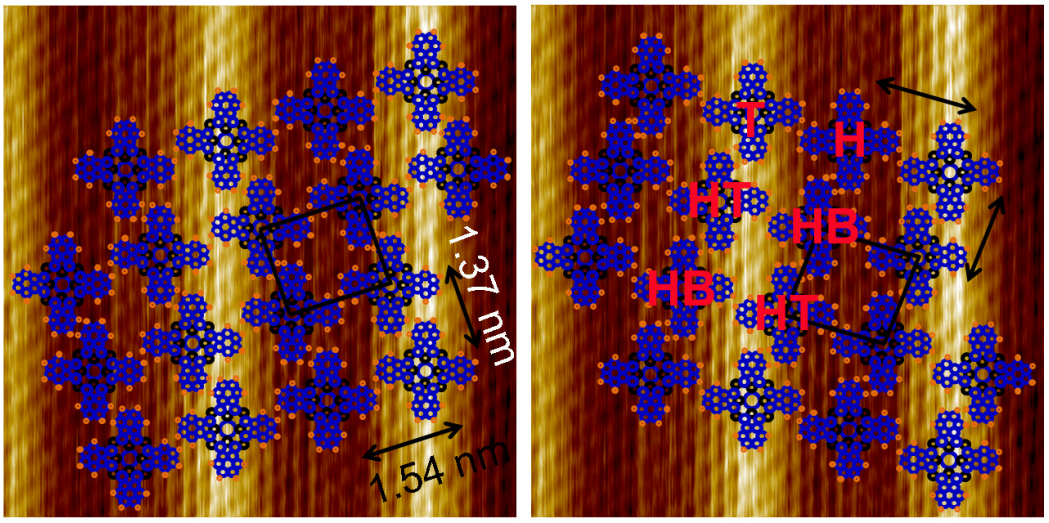

FIGURE 6.12: The proposed structure of CuPc on graphene/Ru(10$\bar{1}$0). There are two equivalent domains of CuPc on Ru(10$\bar{1}$0) in which the distance between adjacent CuPc molecules is $a = 15.4$ Å and $b = 13.7$ Å. The center of a CuPc molecule is either located at the bottom of the Moiré pattern ("hollow site", labeled "H"), on top ("top site", "T"), between two hollows ("hollow bridge", "HB"), or between two tops ("top bridge", "TB").

are also grown very well-ordered on graphene/Ru(10$\bar{1}$0) from monolayer to multilayers. On the left-hand side are the measured LEED patterns of films with different thicknesses recorded with anelectron beam energy (E_o) of 15 eV and on the right-hand side are the measured LEED patterns with red circles representing the LEED patterns fitted by using the Spot-Plotter software [143]. The LEED patterns are almost the same for all CuPc thicknesses. From the fit of the LEED patterns using the Spot-Plotter software [143], there are also two adsorbate domains of CuPc on graphene/Ru(10$\bar{1}$0) which is similar to the case of CuPc on Ru(10$\bar{1}$). But for CuPc on graphene/Ru(10$\bar{1}$0), the distance between adjacent CuPc molecules is $a = 15.4$ Å and $b = 13.7$ Å. The proposed structure of CuPc on graphene/Ru(10$\bar{1}$0) is shown in Fig. 6.12. The center of a CuPc molecule is either located at the bottom of the Moiré pattern ("hollow site", labeled "H"), on top ("top site", "T"), between two hollows ("hollow bridge", "HB"), or between two tops ("top bridge", "TB"). The superstructure matrix of CuPc on graphene is: N $= \begin{bmatrix} 7 & 2 \\ 1 & 6 \end{bmatrix}$ with respect to Ru(10$\bar{1}$0). The differences between the superstructure matrixes of CuPc on Ru(10$\bar{1}$0) and of CuPc on graphene/Ru(10$\bar{1}$0) indicate that the growth of CuPc on graphene/Ru(10$\bar{1}$0) is dominated by the Moiré pattern of graphene.

6.3.2 The bonding of CuPc on graphene/Ru(10$\bar{1}$0)

Shown in Fig. 6.13 are XPS spectra of CuPc molecules on graphene/Ru(10$\bar{1}$0) at different coverages. (a) shows the Cu 2p PES signal, background-corrected and normalized

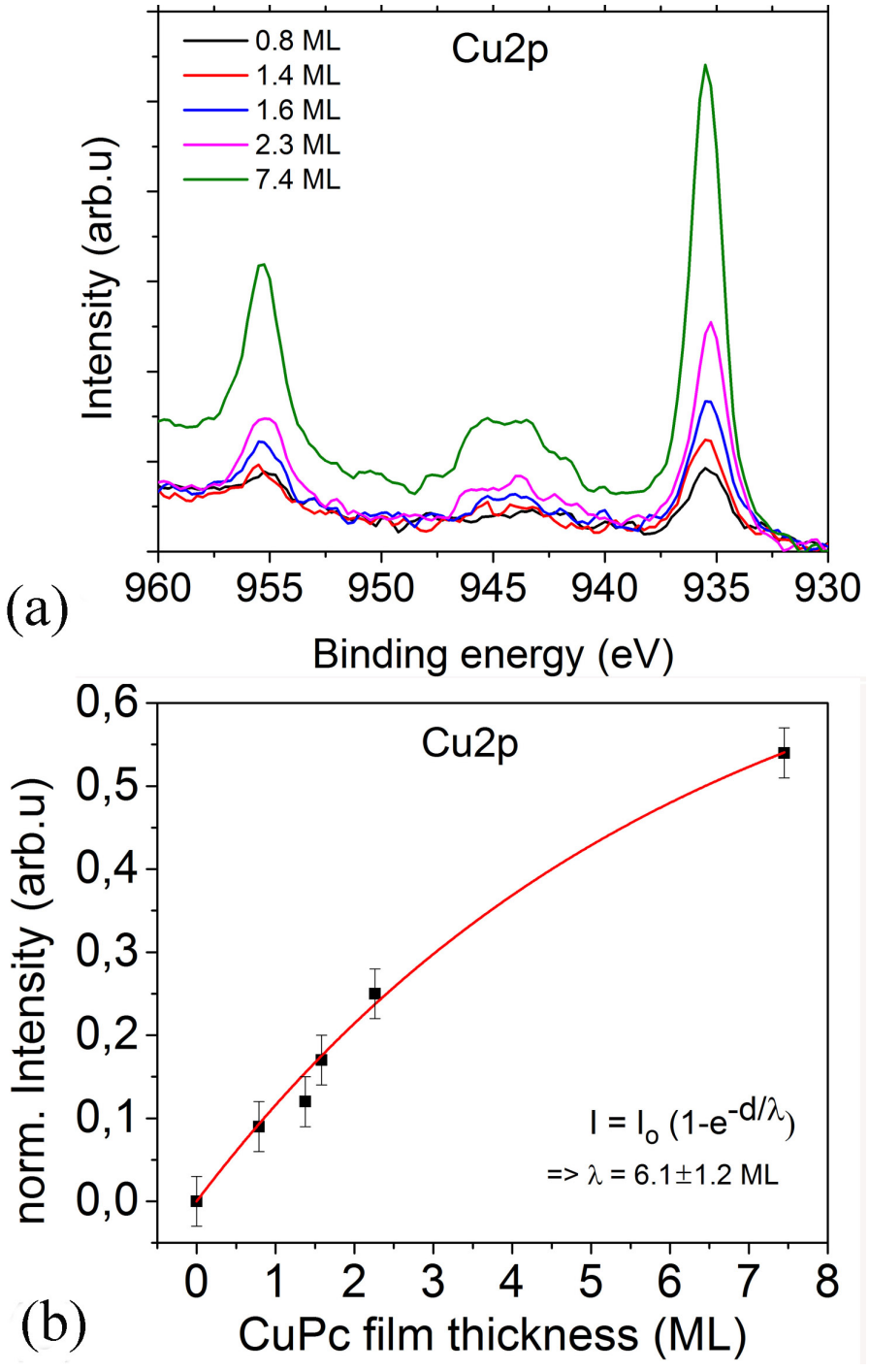

FIGURE 6.13: XPS spectra of CuPc molecules on Ru(10$\bar{1}$0) at different coverages. (a) Cu 2p PES signal, all data were background-corrected and normalized using the QUASES software as described by Tougaard's method [144], (b) Normalized intensity of the Cu 2p PES signal plotted against the CuPc thickness. The solid red line was fitted to the data using an exponential function.

using the QUASES software as described by Tougaard's method [144] and (b) shows the normalized intensity of the Cu 2p PES signal plotted against the CuPc thickness. The solid red line in (b) was fitted to the data using an exponential function as in equation (6.1). The fit describes the behavior sufficiently well. The estimated effective attenuation length of photoelectrons is $\lambda(E) = 6.1$ ML at a kinetic energy of 1069 eV. This result is in good agreement with the attenuation length of CuPc on Ru(10$\bar{1}$0). There are no significant differences between the binding energies of Cu 2p at different coverages. The binding energies of Cu 2p in monolayer and multilayers of CuPc are similar. This means that there is no charge transfer from graphene/Ru(10$\bar{1}$0) to the CuPc molecules and the interaction between CuPc and graphene/Ru(10$\bar{1}$0) is very weak. This is consistent with the LEED patterns of CuPc on graphene/Ru(10$\bar{1}$0).

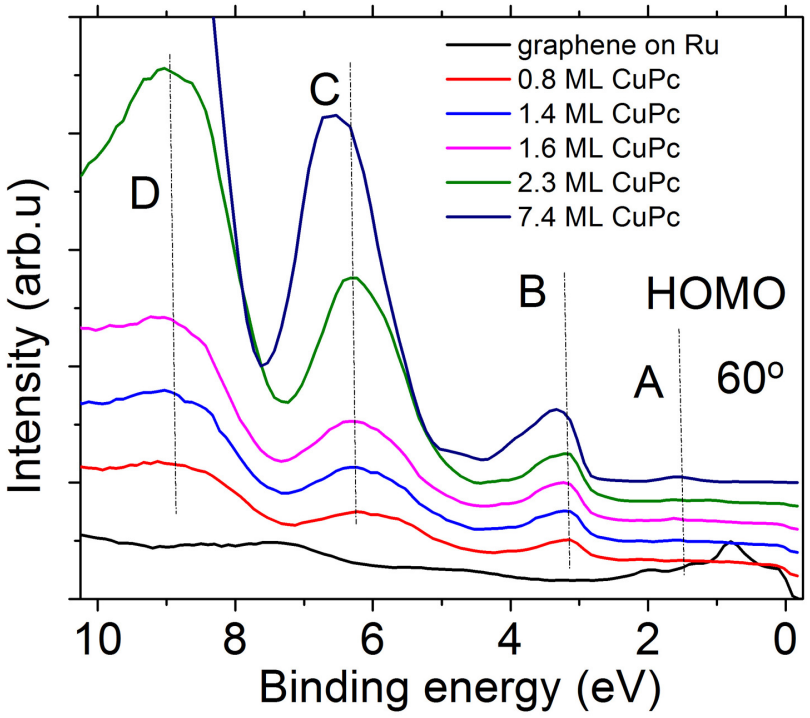

FIGURE 6.14: He 1_α UPS spectra of CuPc films on graphene/Ru(10$\bar{1}$0) with different thicknesses from 0.8 ML to 7.4 ML. The spectra were measured at an angle of $\theta = 60°$. The main features of the CuPc molecules are denoted by A - D.

The interaction of CuPc with graphene/Ru(10$\bar{1}$0) is weak as in the case of CuPc on Ru(10$\bar{1}$0). The UPS spectra of CuPc on graphene/Ru(10$\bar{1}$0) are expected to be very similar to that of CuPc on Ru(10$\bar{1}$0). Shown in Fig. 6.14 are the valence bands of CuPc molecules with different thicknesses, measured at an angle $\theta = 60°$. The main features of the CuPc molecules on graphene/Ru(10$\bar{1}$0) are denoted by A–D. The binding energies of states A, B, C and D are 1.5 eV, 3.2 eV, 6.3 eV and 8.9 eV, respectively. The results are similar to the valence band of CuPc molecules on Ru(10$\bar{1}$0), so peak A at binding energy 1.5 eV is assigned to the HOMO which is related to the porphine-like ring, feature B at

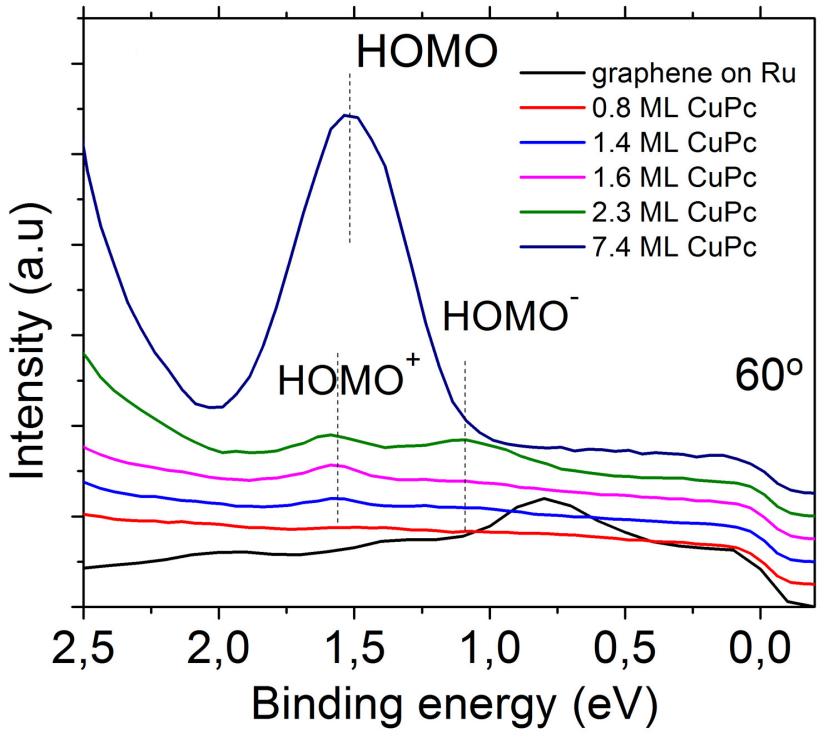

FIGURE 6.15: Expanded spectra of the HOMO region of He 1_α UPS spectra of CuPc films on graphene/Ru(10$\bar{1}$0) with different thicknesses from 0.8 ML to 7.4 ML. The spectra were measured at an angle of $\theta = 60°$. $HOMO^+$ and $HOMO^-$ which are denoted in the spectra of thick layers of CuPc arise from a split of the HOMO in a ML of CuPc.

binding energy 3.2 eV is arising from the outer four benzene rings and features C and D are related to many π and σ states [123]. The expanded spectra of the HOMO region of CuPc films with different thicknesses from 0.8 ML to 7.4 ML are shown in Fig. 6.15. It can be seen that in a ML of CuPc there is a state at binding energy 1.53 eV which is denoted as the HOMO of CuPc. When we increase the thickness of CuPc, there are two states which appear in the HOMO region. The HOMO peak is split into $HOMO^+$ and $HOMO^-$ due to weak inter-orbital interactions (the π-π interaction). The presented results are very similar to our previous results for CuPc on Ru(10$\bar{1}$0).

6.4 CuPc on Ru(0001)

I have tried a number of times to prepare a well-ordered structure of CuPc on Ru(0001), but I have never observed the superstructure of CuPc molecules on Ru(0001). This indicates that Ru(0001) cannot provide a suitable symmetry match to the CuPc lattice. It is not noteworthy to carry on measuring the electronic structure of CuPc on Ru(0001) without knowing the geometric structure.

6.5 CuPc on graphene/Ru(0001)

6.5.1 Geometric properties of CuPc on graphene/Ru(0001)

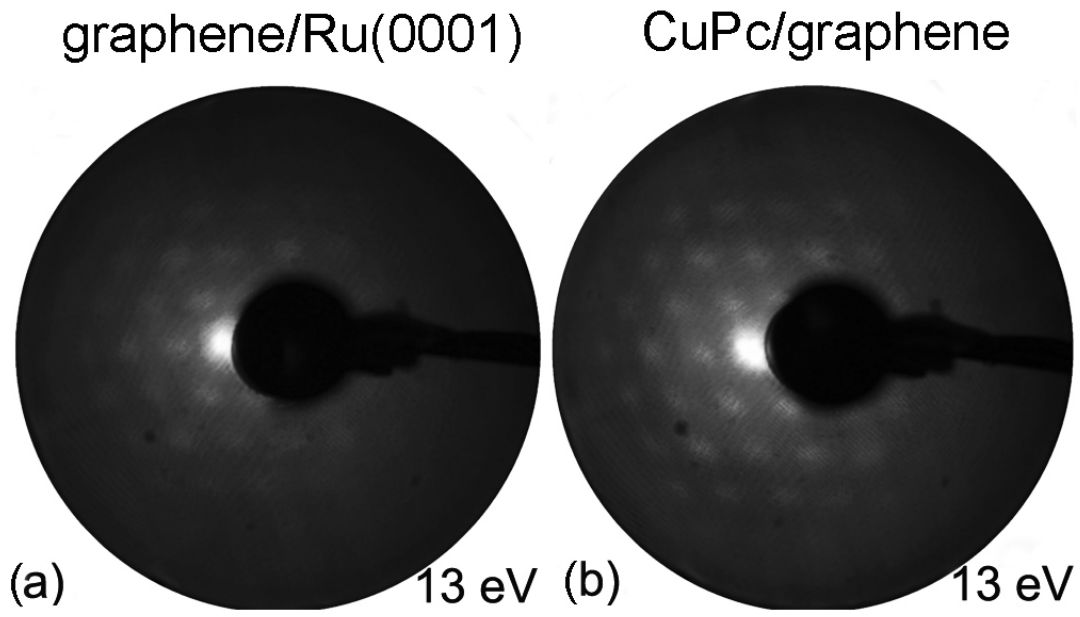

FIGURE 6.16: LEED patterns of (a) graphene on Ru(0001) and (b) on CuPc/graphene-/Ru(0001) recorded with an electron beam energy $E_o = 13\,\text{eV}$. The satellite spots in (a) are caused by a Moiré structure with an approximate periodicity of 11 Ru lattice constants. The distribution and relative distances of the spots in (a) and (b) are similar.

Fig. 6.16 shows LEED patterns of graphene/Ru(0001) and of CuPc/graphene/Ru(0001) recorded at $E_o = 13\,\text{eV}$. The details of the LEED pattern of graphene on Ru(0001) are discussed in chapter 5. The Moiré pattern in the LEED picture of graphene on Ru(0001) is still present in the LEED pictures of a monolayer of CuPc on graphene/Ru(0001). The arrangement and relative distances of the spots are similar to that of graphene/Ru(0001). This shows that the adsorption of CuPc in the monolayer regime does obviously not destroy or modify the Moiré structure of graphene/Ru(0001). Moreover, it indicates that the CuPc molecules may either grow without any lateral order, thus not leading to additional diffraction spots, or well-ordered with an adsorption pattern imprinted by the graphene/Ru(0001). In the latter case the CuPc-superstructure spots would coincide with the graphene/Ru(0001) signals. Such an adsorption behavior was reported previously for FePc on graphene/Ir(111) [137], who also found identical LEED patterns for FePc/graphene/Ir(111) and for graphene/Ir(111). It will be interesting to see if an ordered molecular layer is also established in case of CuPc/graphene/Ru(0001), even though the corrugation of the graphene layer is significantly larger on Ru(0001) than on Ir(111) [80].

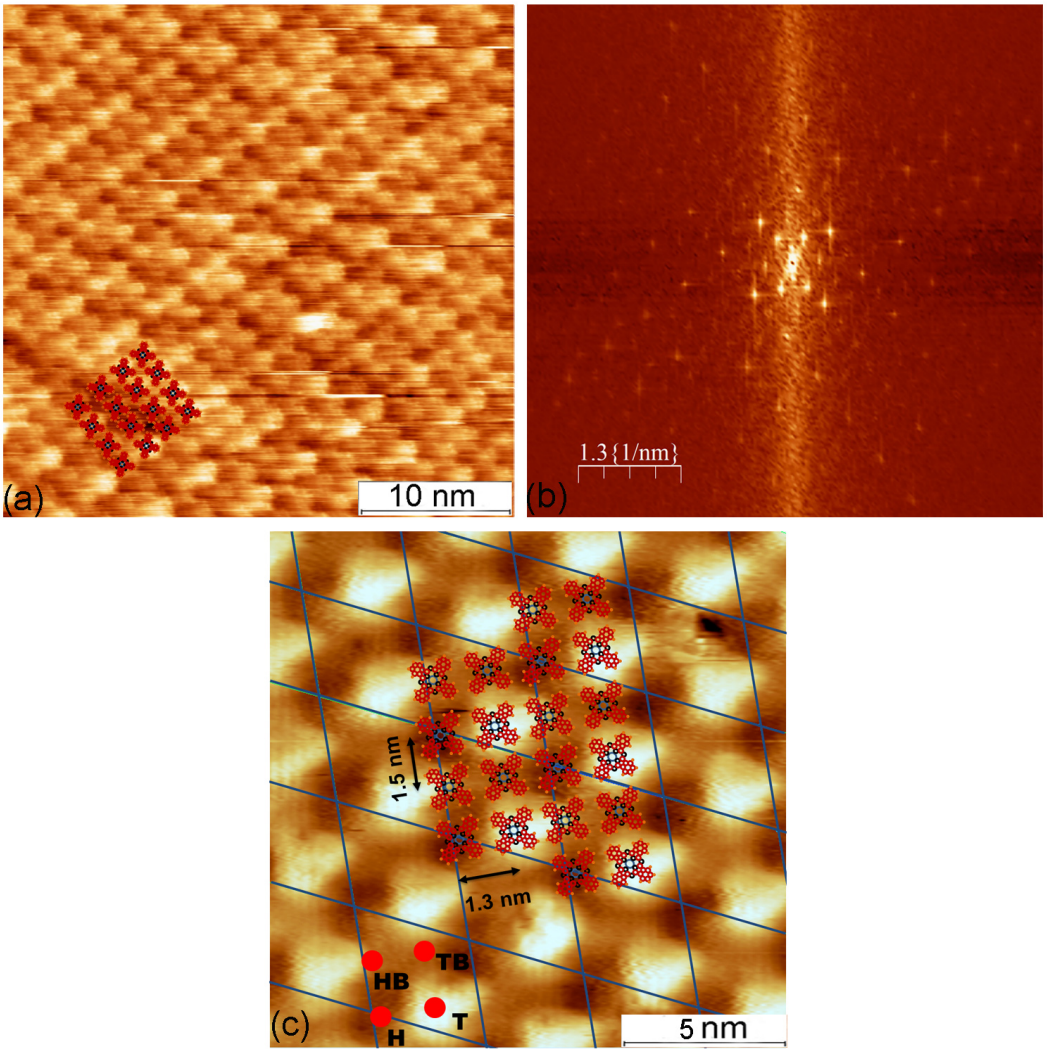

FIGURE 6.17: (a) 30 nm x 30 nm STM images of CuPc/graphene/Ru(0001) with $I = 0.3$ nA, $V_{bias} = -400$ mV. (b) 2D-FFT of (a). The 2D-FFT demonstrates that the spots of the hexagonal structure with threefold symmetry are similar to the LEED pattern of CuPc/graphene/Ru(0001) in Fig. 6.16(d). (c) Real-space model of CuPc-/graphene/Ru(0001) with lattice constants 15 ± 0.5 Å and 13 ± 0.5 Å. The blue lines indicate the unit cells of the graphene layer. See text for details.

Fig. 6.17(a) shows an atomic-resolution room-temperature STM image of a monolayer of CuPc on graphene/Ru(0001), measured with $I_t = 0.3$ nA and $V_{sample} = -0.4$ V. The CuPc molecules can be clearly identified to be closely packed and arranged in a well-ordered structure with domain sizes beyond 10 nm. Fig. 6.17(b) presents a 2D-FFT of Fig. 6.17(a). The 2D-FFT is consistent with the LEED pattern of CuPc/graphene-/Ru(0001) in Fig. 6.16(b) and two different patterns can be distinguished: one has a rectangular, almost square, structure while the other one is hexagonal. Interestingly, the spots in the rectangular structure coincide with the hexagonal pattern. The STM results thus clearly show that the LEED patterns of CuPc/graphene/Ru(0001)

(Fig. 6.16(b)) and of graphene/Ru(0001) (Fig. 6.16(a)) are very similar due to a laterally ordered growth of the CuPc layer with its diffraction spots coinciding with those of the graphene/Ru(0001) substrate. From Fig. 6.17(b) a real-space structure model is derived for CuPc/graphene/Ru(0001) which is shown in Fig. 6.17(c). The CuPc molecules form a well-ordered overlayer on graphene/Ru(0001) with a superstructure matrix $M=\begin{bmatrix} 1/2 & 0 \\ 1/4 & 1/2 \end{bmatrix}$ with respect to the graphene layer.

In this structure model four different absorption sites are observed for the CuPc molecules on the Moiré pattern of graphene/Ru(0001). The CuPc center is either located at the bottom of the Moiré pattern ("hollow site", labeled "*H*" in Fig. 6.17(c)), on top (labeled "top", "*T*"), between two hollows (labeled "hollow bridge", "*HB*"), or between two tops (labeled "top bridge", "*TB*"). The distance between adjacent CuPc molecules is $a = 15 \pm 0.5$ Å and $b = 13 \pm 0.5$ Å, respectively. Note that the ordered phase of CuPc-/graphene/Ru(0001) differs from that of FePc, NiPc and H_2Pc molecules on graphene-/Ru(0001) [25, 134] which form unique Kagome lattices. The distances of adjacent CuPc molecules on HOPG found by STM and by theoretical calculations are 13.8-15.5 Å [126, 157] and 14.0 Å [158], respectively. In contrast to the almost square unit cells generally found for MePc molecules on HOPG [120, 122] and also on the Moiré pattern of graphene/Ir(111) [133, 137, 138], the CuPc molecules in our study form well-ordered domains with a rectangular unit cell ($a = 15 \pm 0.5$ Å and $b = 13 \pm 0.5$ Å). Even though the graphene layer reduces the reactivity of the Ru surface [142], the Moiré pattern of graphene/Ru(0001) obviously still plays a key role in the self-organization of the CuPc adsorbates.

6.5.2 The bonding of CuPc on graphene/Ru(0001)

Shown in Fig. 6.18 are UPS valence spectra measured at different emission angles, (a) of the band structure of graphene/Ru(0001) in EDC (energy distribution curve) and (b) the corresponding mapping model, (c) of the band structure of CuPc/graphene/Ru(0001) in EDC and (d) the corresponding mapping model. The spectra were measured at room temperature using helium I_α excitation energy. The red dotted line is the UPS spectrum of gas-phase CuPc from Ref. [153]. The spectra were intensity-normalized by dividing by the integrated EDC. The detailed discussion of the electron-band structure of graphene on Ru(0001) can be found in chapter 5. For further analysis, these data have to be used as a reference for the interpretation of the valence-band spectra of CuPc-/graphene/Ru(0001) which are presented in Fig. 6.18(c). While the graphene/Ru(0001) features are generally damped by the CuPc adlayer, some additional weak signals appear. However, an assignment is not straightforwardly possible. We thus use the different

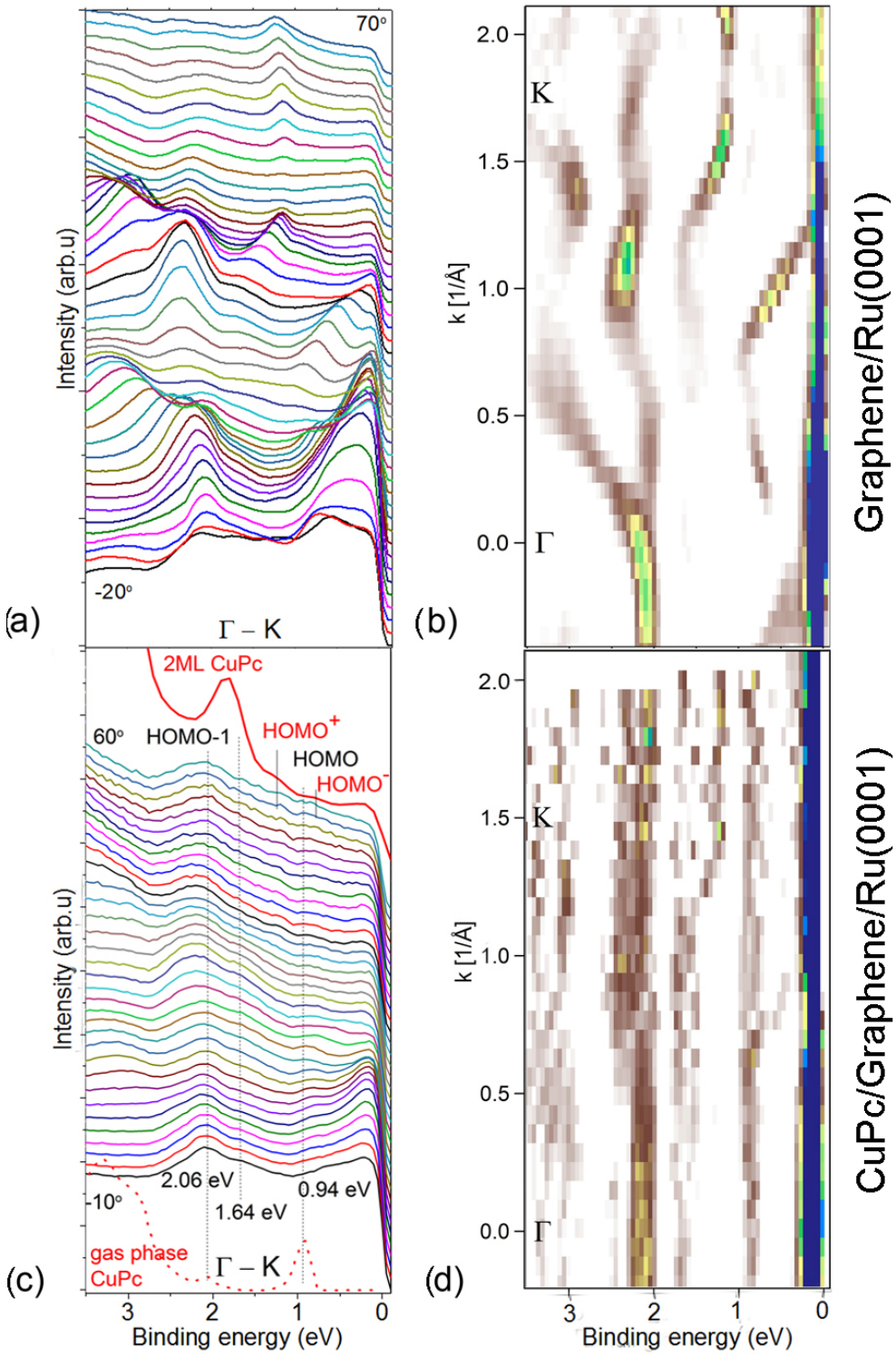

FIGURE 6.18: (a) Angle-dependent UPS spectra in EDC (energy distribution curve) of graphene/Ru(0001) recorded at room temperature with He I_α excitation for emission angles between −20° and 70° in steps of 2° along the Γ-K direction. The spectra were intensity-normalized to the overall intensity of each EDC. (b) Second derivatives of the data in (a) in a color-coded plot after smoothing. (c) and (d): Respective data recorded for CuPc/graphene/Ru(0001) at emission angles between −10° and 60° in steps of 2°. For comparison, a gas-phase spectrum of CuPc is plotted as a red dotted line in Fig. (c) (taken from Ref. [153], intensity not to scale) as well as a spectrum of a 2 ML sample of CuPc on graphene/Ru(0001) plotted as a red solid line (emission angle 45°).

energy-dispersion behaviors of the different signals to distinguish between CuPc and graphene/Ru(0001) contributions. For this purpose, Figs. 6.18(b) and (d) display the second derivatives of the respective ARUPS data recorded at emission angles from −20° to 70° and from −10° to 60°, respectively. Fig. 6.18(b) demonstrates that the graphene-/Ru(0001) bands show a significant energy dispersion. When comparing Fig. 6.18(b) with (d), three additional signals become obvious. These are located at 0.94, 1.64 and 2.06 eV binding energy and show no signs of energy dispersion. This is expected for the CuPc states which show only very weak lateral overlap between adjacent molecules [159, 160]. In the gas phase, CuPc shows two distinct signals in the valence regime which are associated to the highest occupied molecular orbital (HOMO) and the HOMO-1 which are separated by 1.1 eV [153]. The respective gas-phase spectrum (taken from Ref. [153] and shifted in intensity) is plotted at the bottom of Fig. 6.18(c). The comparison suggests an assignment of the signals at 0.94 eV and 2.06 eV binding energy to the CuPc HOMO and HOMO-1, respectively. This agrees well with previous experiments of CuPc on Au(111) [161] and Pc moleculess on HOPG [123, 125], which also show a separation of HOMO and HOMO-1 of about 1.1 eV. The origin of the signal at 1.64 eV binding energy is not clear. However, if we consider the spectrum of a 2 ML sample of CuPc-/graphene/Ru(0001) which is plotted at the top of Fig. 6.18(c), it catches the eye that the HOMO signal of the 2nd-layer CuPc is in this energy regime. Taking into account the considerable error bar in the determination of the energy position of the CuPc signals around 2 eV due to the intense background signal from the graphene/Ru(0001) bands, the most likely explanation for the 1.64 eV peak is a HOMO signal of some CuPc molecules in the 2nd layer which may also be present in case of the 1 ML CuPc/graphene/Ru(0001) sample.

6.6 Summary

The details of the geometric and electronic structures of CuPc on Ru(10$\bar{1}$0), graphene-/Ru(10$\bar{1}$0) and graphene/Ru(0001) have been studied. CuPc molecules can be grown well-ordered on Ru(10$\bar{1}$0) but not on Ru(0001). The growth of CuPc on graphene-/Ru(10$\bar{1}$0) and on grapheneRu(0001) is dominated by the Moiré pattern of graphene. CuPc form well-ordered structures on graphene/Ru(10$\bar{1}$0) and graphene/Ru(0001) with rectangular unit cells. Although complicated by the intense graphene/Ru(0001) background, the UPS results for CuPc/graphene/Ru(0001) indicate relative peak positions of the CuPc HOMO and HOMO-1 signals which are very similar to the gas phase [153] and to CuPc on weakly bonding substrates [128, 161].

Chapter 7

Discussion

7.1 Graphene on Ru surfaces

We use the vertical graphene-metal distance and the downward shift of the graphene π band to characterize the bonding strength between graphene and metal surfaces. The bonding of graphene to a metal surface can be either strong or weak. For the strong-bonding system, a strong chemical bond is formed by electron exchange between the graphene and the metal surface, resulting in a graphene-metal distance of about 0.2 nm and a shift of the graphene π band by about 1–2 eV to higher binding energies. In the weak-bonding regime, the bond is dominated by van der Waals forces without electron exchange, the graphene π band is not shifted in energy and the graphene-metal separation is larger than 0.3 nm.

The bonding of graphene to both Ru surfaces is strong, the graphene π band is shifted by about 1–2 eV to higher binding energies, and the minimum graphene-Ru distance (0.21 nm [100, 104, 112]) is nearly equal to the sum of the covalent Ru radius (R_{Ru} = 0.146 nm) and the covalent graphene radius (R_{gra} = 0.07 nm) [166], R = R_{Ru} + R_{gra} = 0.216 nm. So graphene on Ru surfaces should be chemisorbed. Nevertheless, the adsorption energy of graphene on Ru(0001) is only about 0.1 eV [111] which is smaller than typical chemisorption energies of 0.5–2 eV [167, 168] and, thus, the concepts of chemisorption and physisorption cannot be applied to graphene on Ru surfaces. This is consistent with a previous study of graphene on other metal surfaces which showed weak adsorption energy in combination with strong-bonding graphene-metal surface [168].

Mittendorfer *et al.* [168] studied graphene on Ni(111) and showed that a charge transfer occurs between graphene and Ni(111), leading to a strong hybridization between the top-site C p_z orbital and the Ni d_{z^2} orbitals. Ni donates electrons from its d_{z^2} orbitals

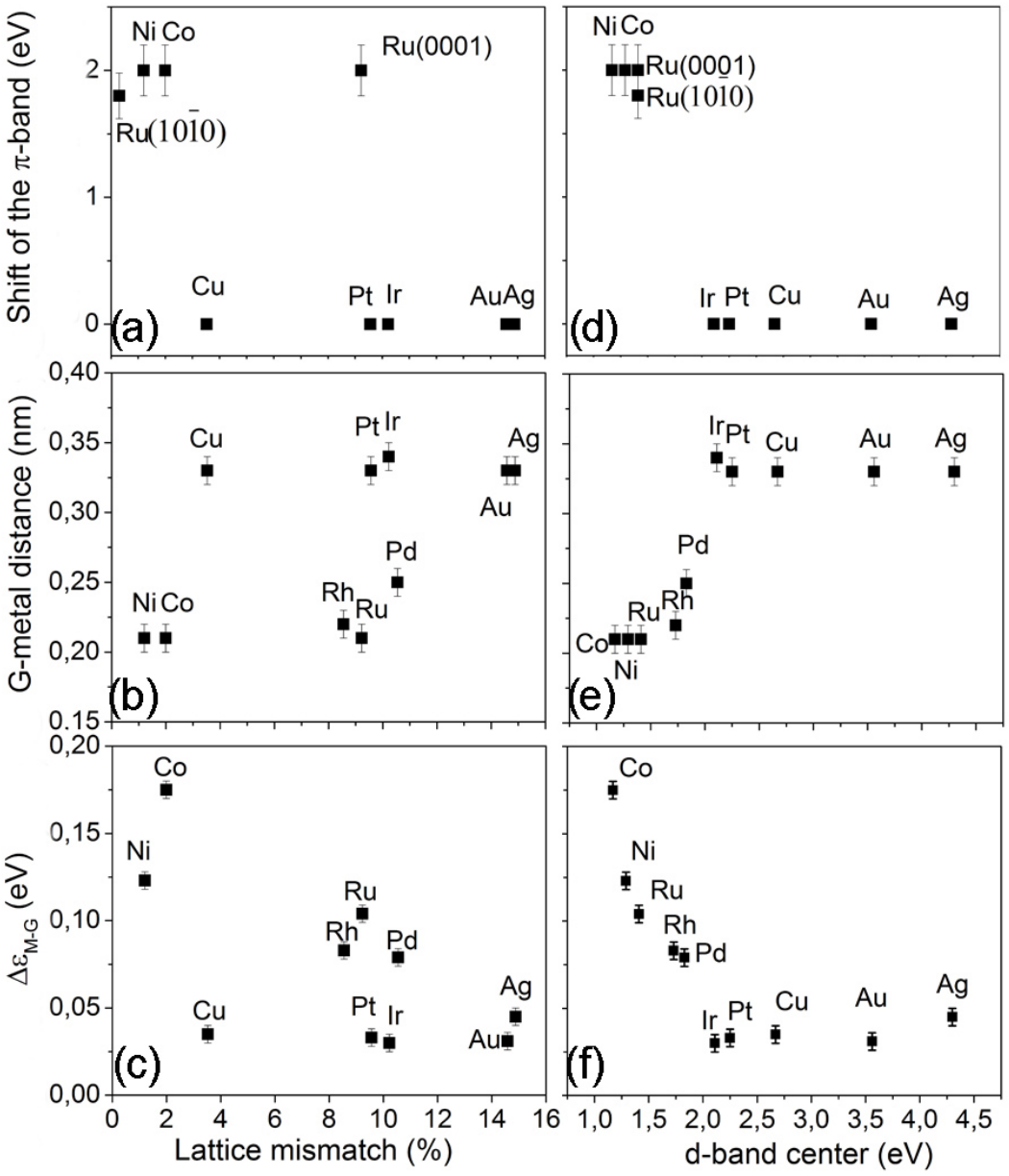

FIGURE 7.1: (a) shows the shift of the π band of graphene on different metals (Ni [78, 79], Co [77], Cu [86, 87], Pt [83, 84], Ir [82, 83], Au [86, 89], and Ag [86, 88]), (b) the graphene-metal distance [56], and (c) the interaction energy, $\Delta\epsilon_{M-G}$, [111, 162–164], all as functions of the lattice mismatch; (d), (e) and (f) report the same quantities as functions of the *d*-band center [165].

to the graphene π-band and graphene back-donates electrons from its σ-band to the Ni d_{xz} and d_{yz} orbitals [168], thus forming a chemical bond via a donation/back-donation mechanism [167]. The adsorption energy is dominated by van der Waals interactions and, therefore, only amounts to 0.2 eV.

As shown in the previous paragraphs, even though the lattice mismatches of graphene on Ru(0001) and on Ru(10$\bar{1}$0) are different, the binding-energy shifts for the two surface orientations are very similar. Graphene interacts strongly with both Ru(0001) and Ru(10$\bar{1}$0) and this is also consistent with other systems [117, 118]. Fig. 7.1(a), (b) and (c) show the dependence of the theoretical interaction energy, $\Delta\epsilon_{M-G}$ [111, 162–164], i.e. the energy per carbon atom that is needed to remove the graphene from the metal, the measured graphene-metal distance, and the downward shift of the π band of graphene on different metals (Ni [78, 79], Co [77], Cu [86, 87], Pt [83, 84], Ir [82, 83], Au [86, 89], and Ag [86, 88]), all as a function of the lattice mismatch [56]. The local-density approximation (LDA) data, $\Delta\epsilon_{M-G}$, in Refs. [111, 162–164] were used to explain the strong bonding trend of graphene to a large variety of metallic substrates. The generalized gradient approximations (GGAs) and the recently developed van der Waals density functional (vdW-DF) usually tend to underestimate the bonding in these systems and, therefore, contrary to the experimental data, predict no binding at all.

As one can see in Fig. 7.1, the bonding strength does not depend on the lattice mismatch as there is no obvious trend in the data. Strong bonding is observed in both lattice-matched and lattice-mismatched systems [56], e.g. graphene on Ni(111) (lattice-matched) and graphene on Ru(0001) (lattice-mismatched) are both strongly interacting. Conversely, Ru(0001) (2.71 Å), Re(0001) (2.76 Å), Rh(111) (2.69 Å), Pd(111) (2.75 Å) and Pt(111) (2.77 Å) have very similar lattice parameters but can be sorted into the two different interaction regimes. We conclude that there is no clear dependence of the interaction between graphene and transition metals on the lattice mismatch and, therefore, that the lattice mismatch does not play an important role in the bonding of graphene. This also explains why the downward shift of the π band is similar for Ru(0001) and Ru(10$\bar{1}$0).

While the lattice mismatch cannot explain the difference in the bonding strength, the hybridization between the metal d valence band and the π bands of graphene is the most important parameter, as suggested in Ref. 56. According to the d-band model [165, 169, 170], the different interaction between the different metals and graphene is due to the position of the metal d band below the Fermi level. Figs. 7.1(d), (e) and (f) show the dependence of the π-band position, the experimental graphene-metal distance and the interaction energy [111, 162–164] as a function of the center of the d band [165].

The downward shifts of the π-band on Ru(0001) and Ru(10$\bar{1}$0) that we obtained are also included in Fig. 7.1(d).

It it visible that depending on the position of the d-band center the metal-graphene interaction changes in a monotonic way. If the d-band center is closer to the Fermi level the graphene will interact stronger. Metals with their d-band center located within 2 eV below the Fermi level are strongly interacting while those having their d-band center more than 2 eV below are weakly interacting [56].

Our data are consistent with the d-band model: The interaction of graphene with Ru is very strong and the Ru d-band center is less than 2 eV below the Fermi level. Although the d-band model is very simple it can explain the strong bonding trend of graphene to a large variety of metallic substrates. However, the d-band model cannot be used for weak-bonding systems which are dominated by van der Waals interactions. In this case, more detailed electronic structure calculations are required.

7.2 CuPc on graphene on Ru surfaces

There are two main factors influencing the formation of ordered structures of CuPc. One is the lattice mismatch between CuPc and the substrate and the other is the chemical composition of the surface region which affects the strength of the substrate-molecule interaction [171]. CuPc molecules can be grown in well-ordered layers on Ru(10$\bar{1}$0) but not on the active surface Ru(0001). One possible explanation is that Ru(0001) cannot provide a suitable symmetry match to the CuPc lattice but Ru(10$\bar{1}$0) can. The present results are in good agreement with previous experiments of CuPc on InAs(100) and on InSb(100) [171]. The study of CuPc on InAs(100) and on InSb(100) [171] demonstrated that ordered CuPc can be grown on InAs(100) and InSb(100) (4 x 2)/c(8 x 2) but not on GaSb(100) and GaSb(100). The GaAs(100) bulk lattice is not of an appropriate size for the accommodation of CuPc and GaSb(100) is an active surface leading to strong substrate-molecule interactions resulting in disordered adsorption. In our case, the lattice constant of Ru(10$\bar{1}$0) in one direction is similar to that of the InSb(100) (4 x 2)/c(8 x 2) surface (a = 0.428 nm). Therefore, Ru(10$\bar{1}$0) provides a suitable symmetry match to the CuPc lattice leading to the growth of CuPc molecules in a well-ordered structure.

There are no significant differences in the valence bands of CuPc in various thicknesses on Ru(10$\bar{1}$0), graphene/Ru(10$\bar{1}$0) and graphene/Ru(0001). This indicates that the electronic properties of CuPc are not affected by these substrates or that the interactions between CuPc and Ru(10$\bar{1}$0), graphene/Ru(10$\bar{1}$0) and graphene/Ru(0001) are rather

weak. If the interaction is sufficiently weak the CuPc molecules can diffuse laterally to form an ordered structure. This is similar to the findings for FePc, MnPc, NiPc and H_2Pc molecules on graphene/Ru(0001) [134] and CuPc on graphene/Ni(111) [24], which also show a weak molecule-substrate interaction. These findings are also consistent with previous studies by Raman spectroscopy and ARPES [142] on multilayers of graphene on Ru(0001). Graphene interacts very strongly with Ru surfaces but the outer sheet of a bilayer of graphene essentially has the electronic structure of a freestanding monolayer of graphene [142]. Due to the strong electronic coupling of the π states of graphene with the Ru d states graphene plays an active role as a buffer which reduces the reactivity of Ru surfaces. Therefore, the added second layer of graphene or of another molecule interacts weakly with graphene/Ru surfaces [142].

Chapter 8

Conclusion and Outlook

8.1 Conclusion

Using high-resolution angle-resolved photoemission spectroscopy and density-functional theory, the details of the electronic structures of three ruthenium surfaces, Ru(0001), Ru ($10\bar{1}0$) and Ru(1,1,$\bar{2}$,10), were investigated. In our experiments, the Fermi surfaces of Ru surfaces are richer in details than those reported in the literature. The results are consistent with previous de Haas-van Alphen data and with relativistic calculations of the bulk. The inner potential of Ru surfaces has been estimated by comparing the experimental data with bulk calculations. The main contribution to the photoemission signal comes from the bulk electronic structure even though surface states were measured directly. On the basis of LEED and STM data Ru(1,1,$\bar{2}$,10) can be estimated to feature, as expected, five-atom wide (0001) terraces and one-atom high steps. In the band structure of Ru(1,1,$\bar{2}$,10), a split band is observed due to a lateral surface superlattice by Umklapp processes. The data can be used as a reference to facilitate subsequent studies of the catalysis of organic molecules on ruthenium.

Well-ordered graphene can be prepared on three surfaces of different symmetry: Ru(0001), Ru($10\bar{1}0$) and Ru(1,1,$\bar{2}$,10). Graphene on Ru(0001) has a Moiré structure which approximately corresponds to 12 carbon atoms overlaid on 11 Ru(0001) atoms. Graphene on Ru($10\bar{1}0$) only has a Moiré structure in one direction. In the [0001]-direction, the lattice mismatch is only 0.2% averaged while in the [$\bar{1}2\bar{1}0$] direction the carbon lattice is mismatched by about 9.2% with respect to the Ruthenium lattice. Interestingly, the ARPES data show that the π band of graphene on Ru(0001), Ru($10\bar{1}0$) and Ru(1,1,$\bar{2}$,10) is shifted by about 1.3–1.7 eV with respect to the free-standing graphene. This means that the bonding of graphene with Ru(0001), Ru($10\bar{1}0$) and Ru(1,1,$\bar{2}$,10) is very similar. Graphene interacts strongly with all three surfaces, Ru(0001), Ru($10\bar{1}0$)

and Ru(1,1,$\bar{2}$,10), even though the lattice mismatch is different. The *d*-band model completely explains the trend of the bonding properties of graphene on different metal surfaces and shows that the main parameter governing the strong bonding is the position of the metal *d*-band center while the lattice mismatch plays no significant role.

CuPc molecules can be grown well-ordered on Ru(10$\bar{1}$0) but not on Ru(0001) because Ru(10$\bar{1}$0) provides a suitable symmetry match to the CuPc lattice. The growth of CuPc on graphene/Ru(10$\bar{1}$0) and Ru(0001) is dominated by the Moiré pattern of graphene. CuPc molecules form well-ordered structures with rectangular unit cells on graphene-/Ru(10$\bar{1}$0) and graphene/Ru(0001). The distances of adjacent CuPc molecules are 15 ± 0.5 Å and 13 ± 0.5 Å on graphene/Ru(0001) and 15.4 ± 0.5 Å and 13.7 ± 0.5 Å on graphene/Ru(10$\bar{1}$0). This indicates that the molecule-substrate interaction dominates over the intermolecular interaction for CuPc molecules on graphene/Ru(10$\bar{1}$0) and graphene/Ru(0001). From the ARPES data, it is shown that the interactions between CuPc and graphene/Ru surfaces are rather weak because graphene plays an active role as a buffer which reduces the reactivity of Ru surfaces.

8.2 Outlook

The basics of the geometric and electronic properties of CuPc molecules on graphene-/Ru surfaces have been studied. I have shown that graphene can be prepared in long-range well-ordered structures on different Ru surfaces and that the Moiré pattern of graphene plays an important role in the self-organization of CuPc molecules. Therefore, graphene on Ru surfaces can be used as a template for the preferential adsorption of metals and organic molecules in further fundamental studies in surface science. For a deeper understanding of the nature of the interaction of molecules with graphene on metal surfaces it is necessary to carry out experimental and theoretical investigations of molecules on graphene. Graphene also can be grown in well-ordered structures on the stepped Ru surface. This means that we can use graphene on stepped Ru as a candidate for future nanoelectronics to study the electronic properties of 1D systems which will yield some new physical properties. Graphene nanoribbons have a band gap which is a prerequisite to be applied in transistors [172]. Therefore, it is necessary to continue to study the geometric and electronic properties molecules graphene on stepped metal surfaces.

Appendix A

Calculated electronic structure of bulk Ruthenium

In this appendix, the calculated electronic structure of bulk Ruthenium will be presented [16]. It can be used as reference to have a better understanding of the experimental data and it might be helpful for future projects. Fig.A.1, A.2, A.3, A.4, A.5, A.6, A.7 and A.8 shows the calculated Fermi surface and band structure in three main directions in which $k_{\perp}$ vector is parallel to the ΓA, ΓM and ΓK direction, respectively.

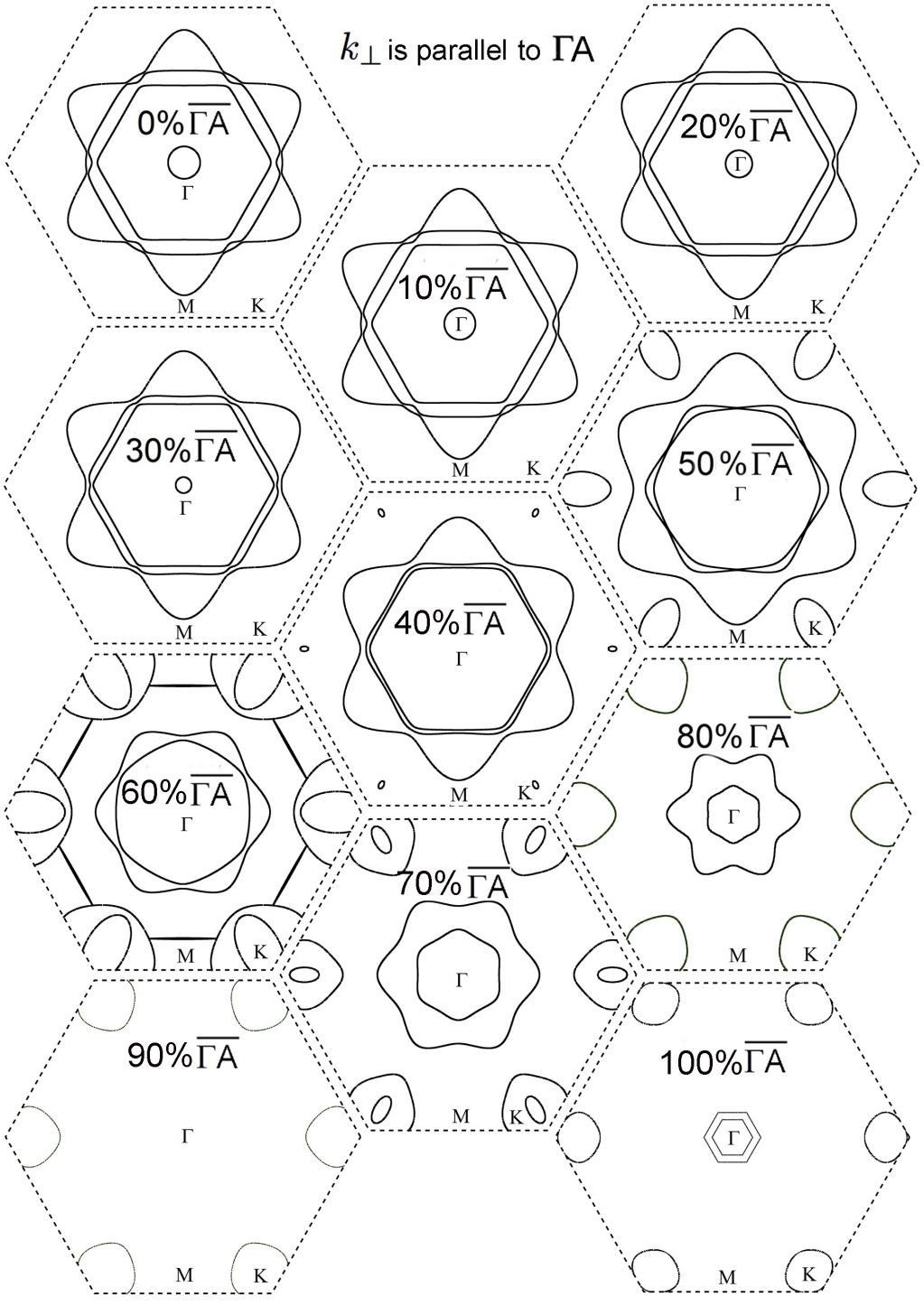

FIGURE A.1: Bulk Fermi surfaces calculated in the ΓMK plane for different $k_\perp$ which is parallel to the ΓA vector, given in fractions of the $\overline{\Gamma A}$ distance; 0 % corresponds to the Γ point and 100 % to the A point.

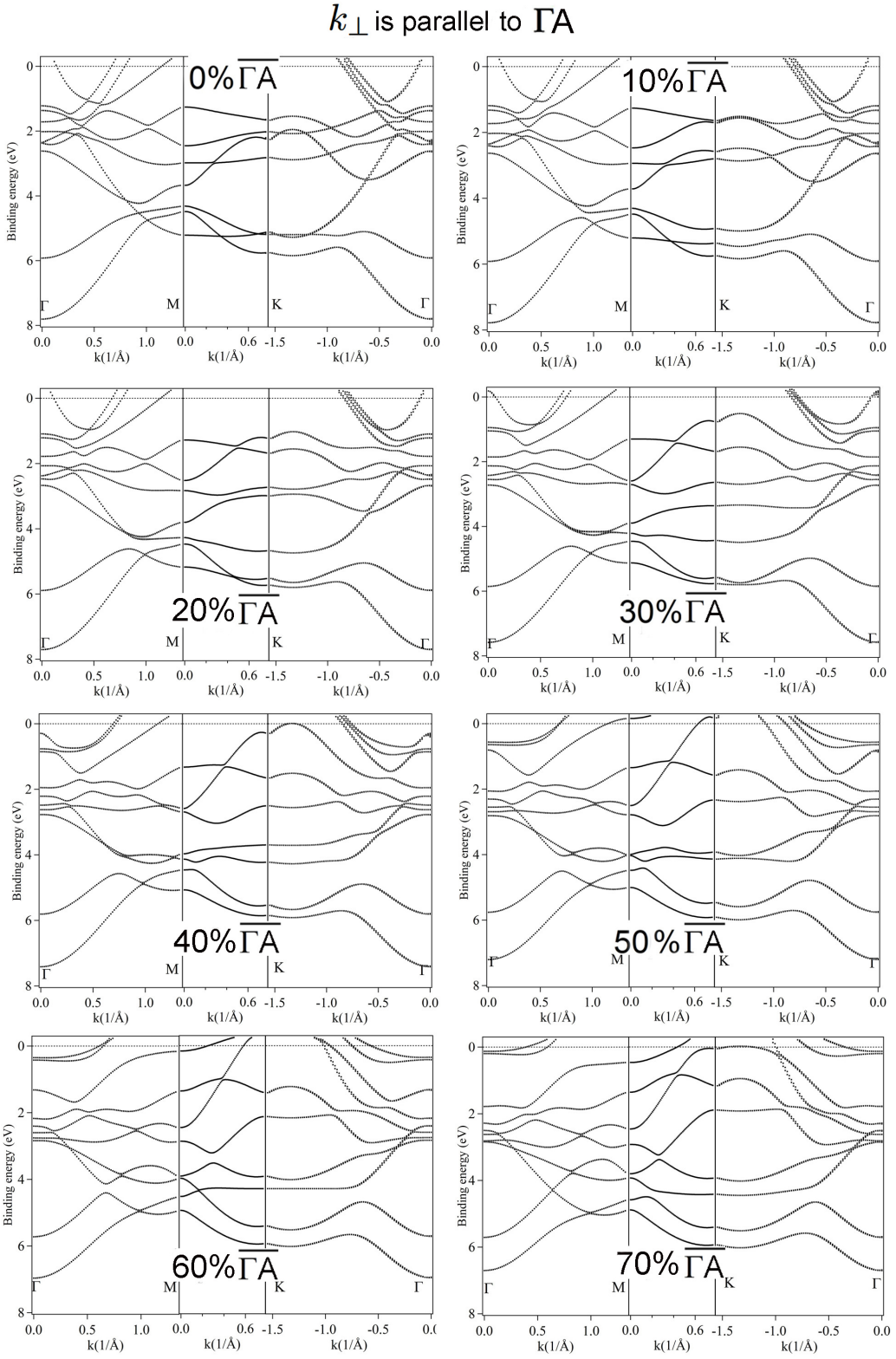

FIGURE A.2: Bulk band structure calculated in ΓM-MK-KΓ direction for different $k_\perp$ (from 0 % to 70 %) which is parallel to the ΓA vector, given in fractions of the $\overline{\Gamma A}$ distance; 0 % corresponds to the Γ point and 100 % to the A point.

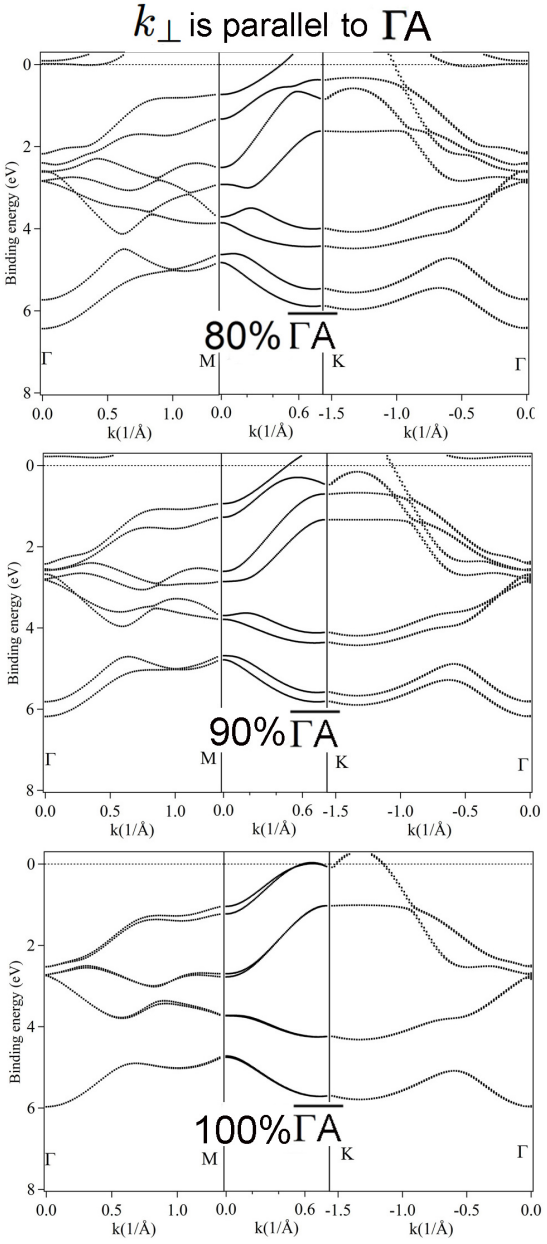

FIGURE A.3: Bulk band structure calculated in ΓM-MK-KΓ direction for different $k_\perp$ (from 80 % to 100 %) which is parallel to the ΓA vector, given in fractions of the $\overline{\Gamma A}$ distance; 0 % corresponds to the Γ point and 100 % to the A point.

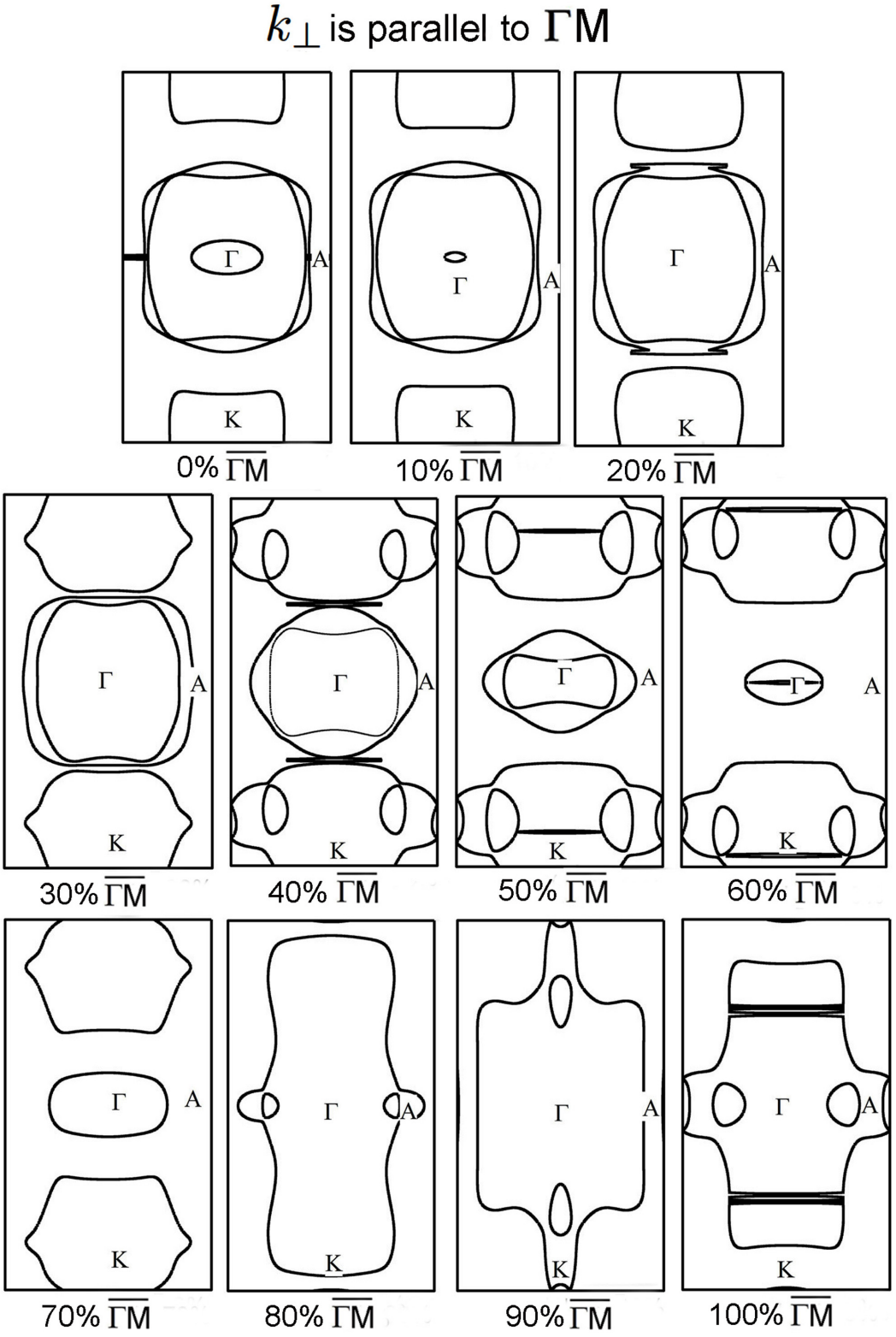

FIGURE A.4: Bulk Fermi surfaces calculated in the ΓAK plane for different $k_\perp$ which is parallel to the ΓM vector, given in fractions of the $\overline{\Gamma M}$ distance; 0 % corresponds to the Γ point and 100 % to the M point.

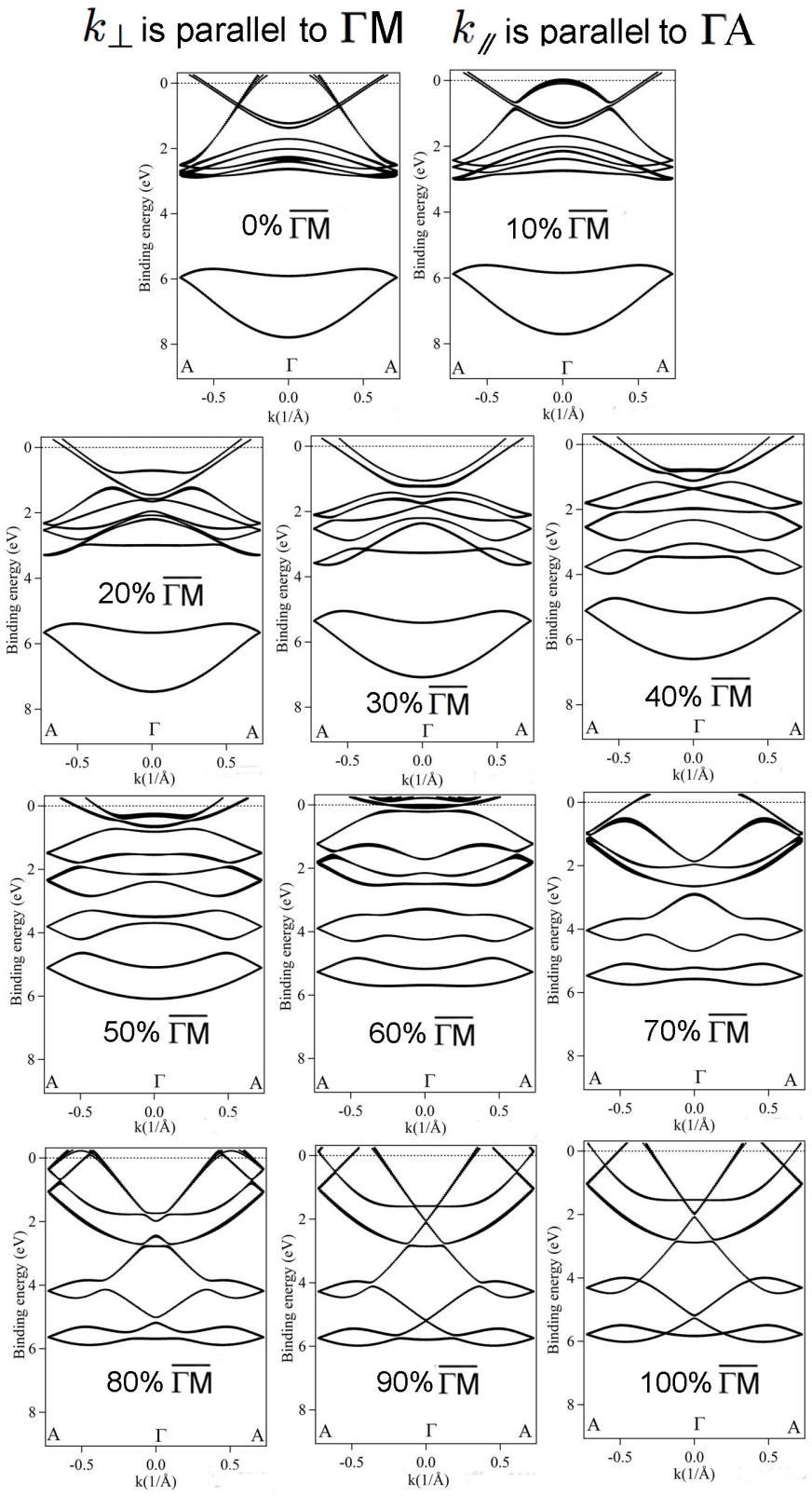

FIGURE A.5: Bulk band structure calculated in ΓA direction for different $k_\perp$ which is parallel to the ΓM vector, given in fractions of the $\overline{\Gamma M}$ distance; 0 % corresponds to the Γ point and 100 % to the M point.

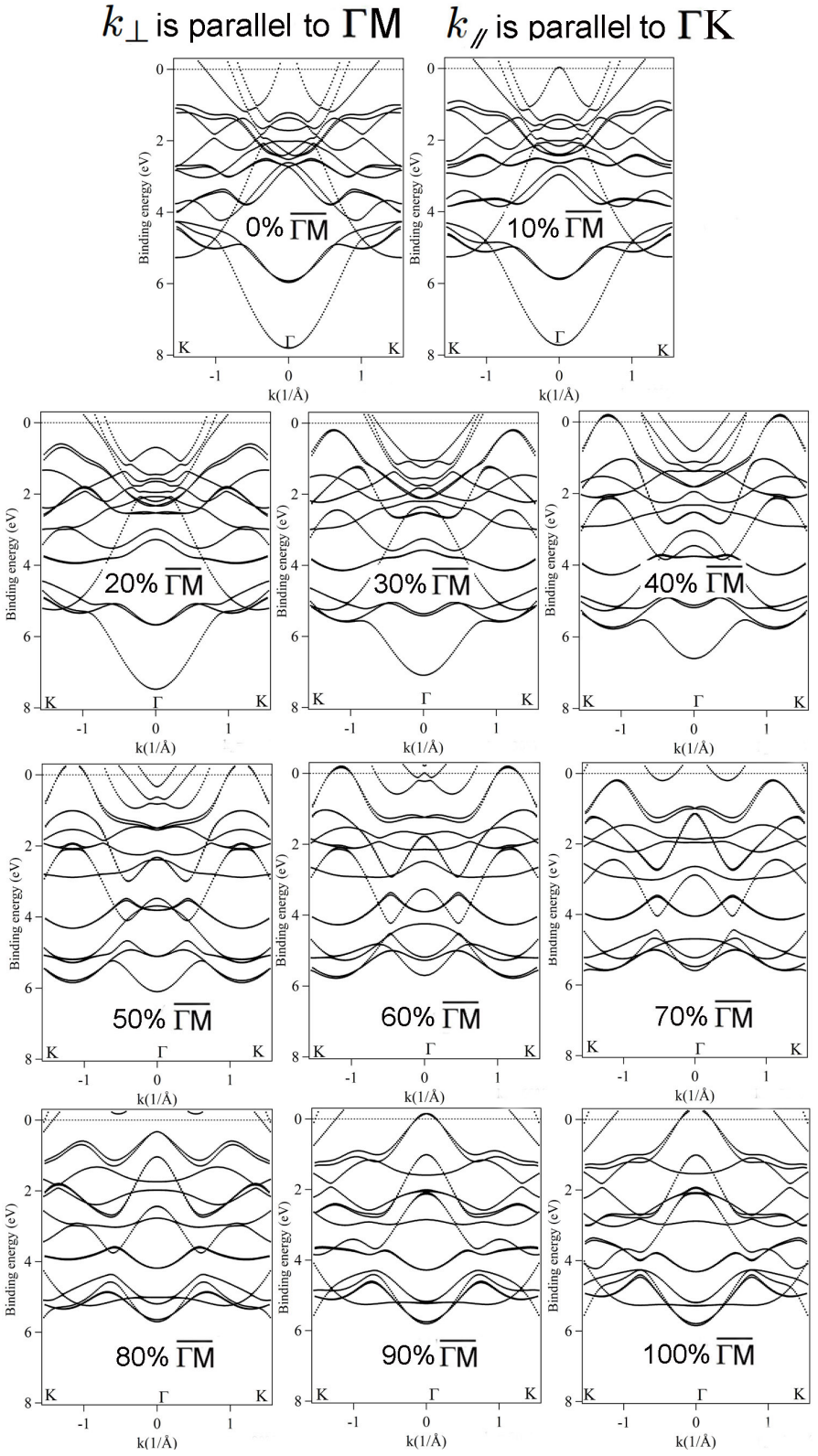

FIGURE A.6: Bulk band structure calculated in ΓK direction for different $k_\perp$ which is parallel to the ΓM vector, given in fractions of the $\overline{\Gamma M}$ distance; 0 % corresponds to the Γ point and 100 % to the M point.

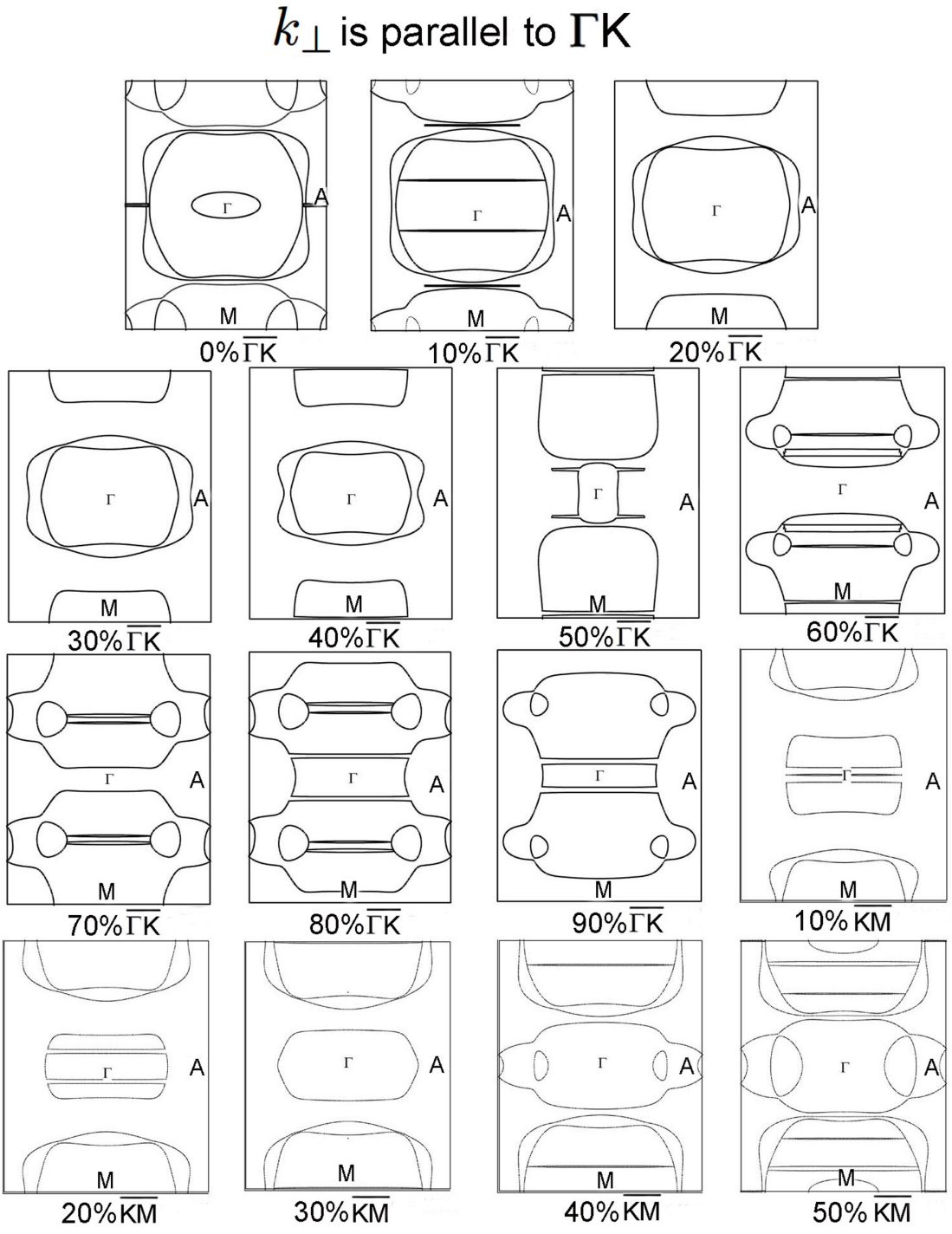

FIGURE A.7: Bulk Fermi surfaces calculated in the ΓAM plane for different $k_\perp$ which is parallel to the ΓKM vector, given in fractions of the $\overline{\Gamma K}$ distance; 0 % corresponds to the Γ point and 100 % to the K point.

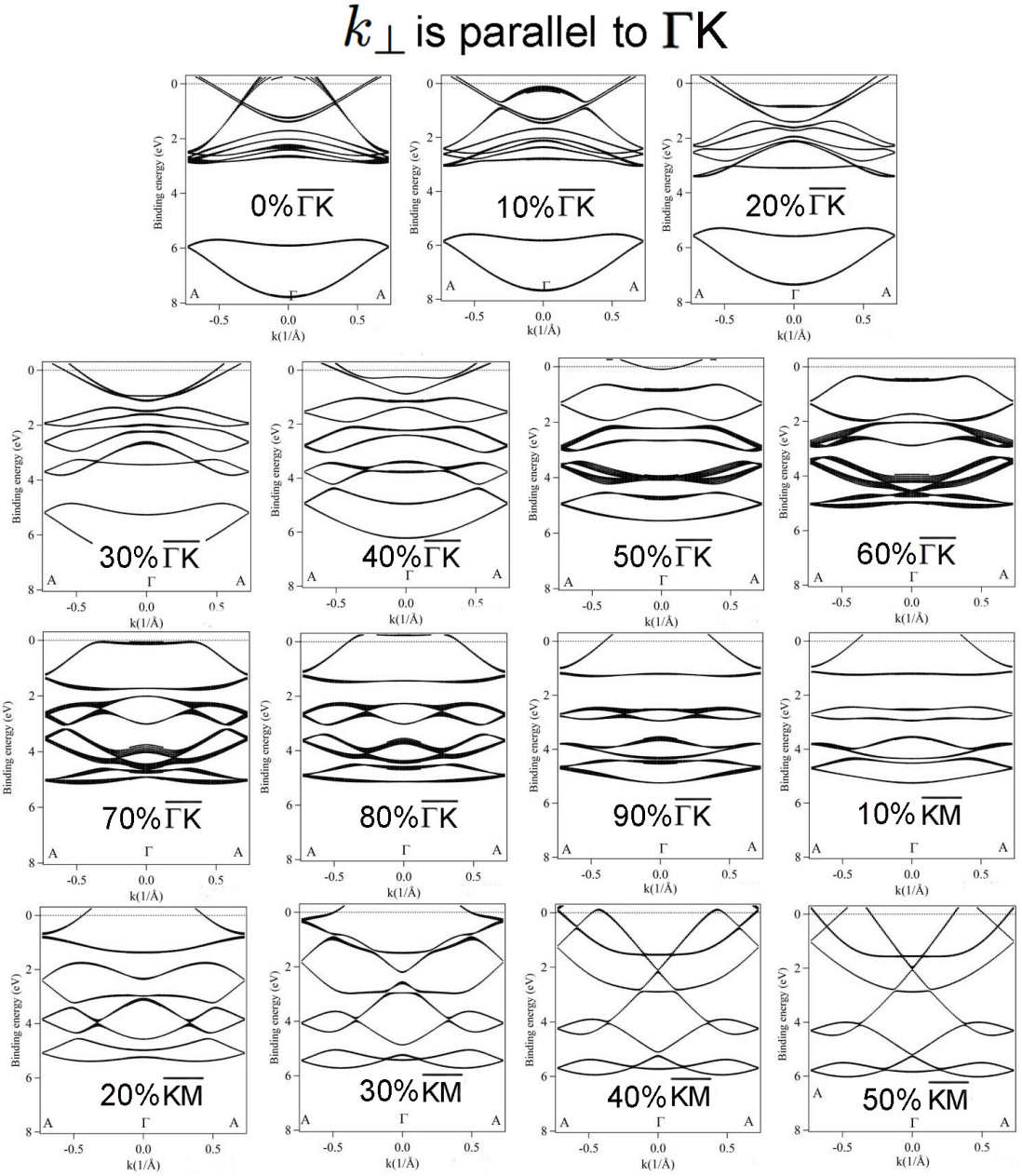

FIGURE A.8: Bulk band structure calculated in ΓA direction for different $k_\perp$ which is parallel to the ΓKM vector, given in fractions of the $\overline{\Gamma K}$ distance; 0 % corresponds to the Γ point and 100 % to the K point.

Bibliography

[1] ITRS. Lithography. In *International Technology Roadmap for Semiconductors*, 2011.

[2] C. W. Gwyn, R. Stulen, D. Sweeney, and D. Attwood. Extreme ultraviolet lithography. *Journal of Vacuum Science & Technology B*, 16(6):3142, 1998.

[3] S. Bajt, N. V. Edwards, and T. E. Madey. Properties of ultrathin films appropriate for optics capping layers exposed to high energy photon irradiation. *Surface Science Reports*, 63(2):73, 2008.

[4] T. E. Madey, N. S. Faradzhev, B. V. Yakshinskiy, and N. V. Edwards. Surface phenomena related to mirror degradation in extreme ultraviolet (EUV) lithography. *Applied Surface Science*, 253(4):1691, 2006.

[5] K. S. Novoselov, A. K. Geim, S. V. Morozov, D. Jiang, M. I. Katsnelson, I. V. Grigorieva, S. V. Dubonos, and A. A. Firsov. Two-dimensional gas of massless Dirac fermions in graphene. *Nature*, 438(7065):197, 2005.

[6] K. S. Novoselov, A. K. Geim, S. V. Morozov, D. Jiang, Y. Zhang, S. V. Dubonos, I. V. Grigorieva, and A. A. Firsov. Electric field effect in atomically thin carbon films. *Science*, 306(5296):666, 2004.

[7] A. K. Geim and K. S. Novoselov. The rise of graphene. *Nature Materials*, 6(3): 183, 2007.

[8] P. W. Sutter, J. I. Flege, and E. A. Sutter. Epitaxial graphene on ruthenium. *Nature Materials*, 7(5):406, 2008.

[9] S. Marchini, S. Gunther, and J. Wintterlin. Scanning tunneling microscopy of graphene on Ru(0001). *Physical Review B*, 76(7):075429, 2007.

[10] A. B. Kuzmenko, E. van Heumen, F. Carbone, and D. van der Marel. Universal optical conductance of graphite. *Physical Review Letters*, 100(11):117401, 2008.

[11] P. Sutter, M. Minniti, P. Albrecht, D. Farias, R. Miranda, and E. Sutter. A high-reflectivity, ambient-stable graphene mirror for neutral atomic and molecular beams. *Applied Physics Letters*, 99(21):211907, 2011.

[12] S. Bae, H. Kim, Y. Lee, X. F. Xu, J. S. Park, Y. Zheng, J. Balakrishnan, T. Lei, H. R. Kim, Y. I. Song, Y. J. Kim, K. S. Kim, B. Ozyilmaz, J. H. Ahn, B. H. Hong, and S. Iijima. Roll-to-roll production of 30-inch graphene films for transparent electrodes. *Nature Nanotechnology*, 5(8):574, 2010.

[13] F. J. Himpsel, K. Christmann, P. Heimann, and D. E. Eastman. Experimental energy-band dispersions and lifetimes for ruthenium. *Physical Review B*, 23(6): 2548, 1981.

[14] M. Lindroos, P. Hofmann, and D. Menzel. Angle-resolved photoemission determination of the band structure of Ru(001). *Physical Review B*, 33(10):6798, 1986.

[15] T. Pelzer, G. Ceballos, F. Zbikowski, B. Willerding, K. Wandelt, U. Thomann, C. Reuss, T. Fauster, and J. Braun. Electronic structure of the Ru(0001) surface. *Journal of Physics-Condensed Matter*, 12(10):2193, 2000.

[16] N. Nguyen, M. Mulazzi, and F. Reinert. Electronic structure and fermi surface of ru(0001) and ru(100) measured with high-resolution angle-resolved photoemission. *Journal of Electron Spectroscopy and Related Phenomena*, 2013.

[17] K. Katsiev, Y. Losovyj, Z. H. Zhou, E. Vescovo, L. Liu, P. A. Dowben, and D. W. Goodman. Graphene on Ru(0001): Evidence for two graphene band structures. *Physical Review B*, 85(19):195405, 2012.

[18] C. Stadler, S. Hansen, I. Kroger, C. Kumpf, and E. Umbach. Tuning intermolecular interaction in long-range-ordered submonolayer organic films. *Nature Physics*, 5 (2):153, 2009.

[19] R. R. Nair, P. Blake, A. N. Grigorenko, K. S. Novoselov, T. J. Booth, T. Stauber, N. M. R. Peres, and A. K. Geim. Fine structure constant defines visual transparency of graphene. *Science*, 320(5881):1308, 2008.

[20] F. Bonaccorso, Z. Sun, T. Hasan, and A. C. Ferrari. Graphene photonics and optoelectronics. *Nature Photonics*, 4(9):611, 2010.

[21] T. J. Echtermeyer, L. Britnell, P. K. Jasnos, A. Lombardo, R. V. Gorbachev, A. N. Grigorenko, A. K. Geim, A. C. Ferrari, and K. S. Novoselov. Strong plasmonic enhancement of photovoltage in graphene. *Nature Communications*, 2, 2011.

[22] B. H. Hong, K. S. Kim, Y. Zhao, H. Jang, S. Y. Lee, J. M. Kim, K. S. Kim, J. H. Ahn, P. Kim, and J. Y. Choi. Large-scale pattern growth of graphene films for stretchable transparent electrodes. *Nature*, 457(7230):706, 2009.

[23] S. X. Wu, Z. Y. Yin, Q. Y. He, X. A. Huang, X. Z. Zhou, and H. Zhang. Electrochemical Deposition of Semiconductor Oxides on Reduced Graphene Oxide-Based Flexible, Transparent, and Conductive Electrodes. *Journal of Physical Chemistry C*, 114(27):11816, 2010.

[24] W. D. Dou, S. P. Huang, R. Q. Zhang, and C. S. Lee. Molecule-substrate interaction channels of metal-phthalocyanines on graphene on Ni(111) surface. *Journal of Chemical Physics*, 134(9):094705, 2011.

[25] H. J. Gao, J. H. Mao, H. G. Zhang, Y. H. Jiang, Y. Pan, M. Gao, and W. D. Xiao. Tunability of Supramolecular Kagome Lattices of Magnetic Phthalocyanines Using Graphene-Based Moire Patterns as Templates. *Journal of the American Chemical Society*, 131(40):14136, 2009.

[26] E. Shincho, C. Egawa, S. Naito, and K. Tamaru. The Behavior of Co Adsorbed on Ru(1,1,10) and Ru(001) - the Dissociation of Co at the Step Sites of the Ru(1,1,10) Surface. *Surface Science*, 149(1):1, 1985.

[27] H. Over, Y. B. He, A. Farkas, G. Mellau, C. Korte, M. Knapp, M. Chandhok, and M. Fang. Long-term stability of Ru-based protection layers in extreme ultraviolet lithography: A surface science approach. *Journal of Vacuum Science & Technology B*, 25(4):1123, 2007.

[28] R. F. Service. Molecules get wired. *Science*, 294(5551):2442, 2001.

[29] J. E. Ortega, S. Speller, A. R. Bachmann, A. Mascaraque, E. G. Michel, A. Narmann, A. Mugarza, A. Rubio, and F. J. Himpsel. Electron wave function at a vicinal surface: Switch from terrace to step modulation. *Physical Review Letters*, 84(26):6110, 2000.

[30] F. Baumberger, M. Hengsberger, M. Muntwiler, M. Shi, J. Krempasky, L. Patthey, J. Osterwalder, and T. Greber. Step-lattice-induced Band-Gap Opening at the Fermi Level. *Physical Review Letters*, 92(1):016803, 2004.

[31] K. S. Kim, H. Morikawa, W. H. Choi, and H. W. Yeom. Strong lateral electron coupling of pb nanowires on stepped Si(111): Angle-resolved photoemission studies. *Physical Review Letters*, 99(19):196804, 2007.

[32] T. Zambelli, J. Wintterlin, J. Trost, and G. Ertl. Identification of the "active sites" of a surface-catalyzed reaction. *Science*, 273(5282):1688, 1996.

[33] C. E. Tripa and J. T. Yates. Surface-aligned reaction of photogenerated oxygen atoms with carbon monoxide targets. *Nature*, 398(6728):591, 1999.

[34] Mikhail I. Katsnelson. *Graphene: Carbon in two dimensions*. Cambridge University Press, 2012.

[35] O. SIDS. *Copper phthalocyanine, CAS No.: 147-14-8*. International Programme on Chemical Safety (IPCS), 1993.

[36] N. M. Amar, R. D. Gould, and A. M. Saleh. Structural and electrical properties of the alpha-form of metal-free phthalocyanine (α-H_2Pc) semiconducting thin films. *Current Applied Physics*, 2(6):455, 2002.

[37] Yip wah Chung. *Practical guide to surface science and spectroscopy*. Academic Press, San Diego, 2001.

[38] M. Horn-von Hoegen. Growth of semiconductor layers studied by spot profile analysing low energy electron diffraction - Part II. *Zeitschrift Fur Kristallographie*, 214(11):684, 1999.

[39] M. Henzler. Measurement of Surface Defects by Low-Energy Electron Diffraction. *Appl. Phys. A*, 34:205, 1984.

[40] M. Henzler. LEED-investigation of step arrays on cleaved germanium(111) surfaces. *Surface science*, 19:159, 1970.

[41] Hoelzl J., F. K. Schulte, and H. Wagner. *Solid surface physics*. Springer tracts in modern physics. Springer-Verlag, Berlin ; New York, 1979.

[42] R. Wiesendanger. *Scanning Probe Microscopy and Spectroscopy: Methods and Applications*. Cambridge University Press, 1994.

[43] H. Bubert and H. Jenett. *Surface and Thin Film Analysis: Principles, Instrumentation and Application*. Wiley-VCH Verlag GmbH, 2002.

[44] G. Binnig, H. Rohrer, C. Gerber, and E. Weibel. Tunneling Through a Controllable Vacuum Gap. *Applied Physics Letters*, 40:178, 1982.

[45] G. Binnig, H. Rohrer, C. Gerber, and E. Weibel. 7x7 Reconstruction on Si(111) Resolved in Real Space. *Physical Review Letters*, 50:120, 1983.

[46] K.S. Birdi. *Scanning probe microscopes: Applications in Science and Technology*. CRC Press, LLC, 2003.

[47] F. Reinert and S. Hüfner. Photoemission spectroscopy - from early days to recent applications. *New Journal of Physics*, 7:97, 2005.

[48] Stefan Hüfner. *Photoelectron Spectroscopy: Principles and Applications.* Springer Series in Solid-State Science, 2003.

[49] Stefan Hüfner. *Very High Resolution Photoelectron Spectroscopy.* Springer, 2007.

[50] Wolfgang Schattke and Michel A.Van Hove. *Solid-State Photoemission and Related Methods.* Wiley-VCH, 2003.

[51] S. D. Kevan. *Angle-resolved photoemission: Theory and Current Applications.* Elsevier Science Publishers B.V, 1992.

[52] H. Hertz. Über einen Einfluss des ultravioletten Lichtes auf die electrische Entladung. *Annalen der Physik und Chemie*, 367:983, 1887.

[53] A. Einstein. Über einen die Erzeugung und Verwandlung des Lichtes betreffenden heuristischen Gesichtspunkt. *Annalen der Physik*, 322:132, 1905.

[54] A. Damascelli, Z. Hussain, and Z. Shen. Angle-resolved photoemission studies of the cuprate superconductors. *Rev. Mod. Phys*, 75:2, 2003.

[55] D. Ehm, F. Reinert, G. Nicolay, S. Schmidt, S. Hufner, R. Claessen, V. Eyert, and C. Geibel. Electronic structure of $CeNi_2Ge_2$ investigated by angle-resolved photoemission and density-functional calculations. *Physical Review B*, 64(23): 235104, 2001.

[56] Matthias Batzill. The surface science of graphene: Metal interfaces, CVD synthesis, nanoribbons, chemical modifications, and defects. *Surface Science Reports*, 67 (3-4):83, 2012.

[57] O. Jepsen, O. Krogh Andersen, and A. R. Mackintosh. Electronic structure of hcp transition metals. *Physical Review B*, 12(8):3084, 1975.

[58] V. L. Moruzzi, James F. Janak, and A. R. Williams. *Calculated electronic properties of metals.* Pergamon Press, New York, 1978.

[59] Peter J. Feibelman. Electronic structure of clean and carbon-covered closed-packed Rhodium and ruthenium surfaces. *Physical Review B*, 26(10):5347, 1982.

[60] N. A. W. Holzwarth and J. R. Chelikowsky. Bulk and Surface Electron-States in Ruthenium. *Solid State Communications*, 53(2):171, 1985.

[61] James R. Chelikowsky, C. T. Chan, and Steven G. Louie. Theoretical study of the electronic, structural, and cohesive properties of ruthenium. *Physical Review B*, 34(10):6656, 1986.

[62] P. T. Coleridge. The Fermi Surface of Ruthenium as Determined by the de Haas-van Alphen Effect. *Journal of Low Temperature Physics*, 1:577, 1969.

[63] M. Henzler. Atomic Steps on Single-Crystals-Experimental Methods and Properties. *Applied Physics*, 9(1):11, 1976.

[64] B. Lesiak, A. Jablonski, Z. Prussak, and P. Mrozek. Experimental-Determination of the Inelastic Mean Free-Path of Electrons in Solids. *Surface Science*, 223(1-2): 213, 1989.

[65] J. C. Fuggle, T. E. Madey, M. Steinkilberg, and D. Menzel. Photoelectron Spectroscopic Studies of Adsorption of Co and Oxygen on Ru(001). *Surface Science*, 52(3):521, 1975.

[66] P. Giannozzi, S. Baroni, N. Bonini, M. Calandra, R. Car, C. Cavazzoni, D. Ceresoli, G. L. Chiarotti, M. Cococcioni, I. Dabo, A. Dal Corso, S. de Gironcoli, S. Fabris, G. Fratesi, R. Gebauer, U. Gerstmann, C. Gougoussis, A. Kokalj, M. Lazzeri, L. Martin-Samos, N. Marzari, F. Mauri, R. Mazzarello, S. Paolini, A. Pasquarello, L. Paulatto, C. Sbraccia, S. Scandolo, G. Sclauzero, A. P. Seitsonen, A. Smogunov, P. Umari, and R. M. Wentzcovitch. QUANTUM ESPRESSO: a modular and open-source software project for quantum simulations of materials. *Journal of Physics-Condensed Matter*, 21(39):395502, 2009.

[67] Neil W. Ashcroft and N. David Mermin. *Solid state physics*. Holt, New York,, 1976.

[68] A. P. Shapiro, T. Miller, and T. C. Chiang. Angle-Resolved Photoemission-Studies of a Surface-State on a Stepped Cu(332) Surface. *Physical Review B*, 38(3):1779, 1988.

[69] X. Y. Wang, X. J. Shen, R. M. Osgood, R. Haight, and F. J. Himpsel. Observation of lateral superlattice effects on stepped Cu(001). *Physical Review B*, 53(23):15738, 1996.

[70] A. Mugarza, A. Mascaraque, V. Perez-Dieste, V. Repain, S. Rousset, F. J. G. de Abajo, and J. E. Ortega. Electron confinement in surface states on a stepped gold surface revealed by angle-resolved photoemission. *Physical Review Letters*, 87(10):107601, 2001.

[71] A. M. Shikin, S. A. Gorovikov, V. K. Adamchuk, W. Gudat, and O. Rader. Electronic structure of carbon nanostripes. *Physical Review Letters*, 90(25):256803, 2003.

[72] A. M. Shikin, A. Varykhalov, G. V. Prudnikova, V. K. Adamchuk, W. Gudat, and O. Rader. Photoemission from stepped W(110): Initial or final state effect? *Physical Review Letters*, 93(14):146802, 2004.

[73] A. Mugarza, A. Mascaraque, V. Repain, S. Rousset, K. N. Altmann, F. J. Himpsel, Y. M. Koroteev, E. V. Chulkov, F. J. G. de Abajo, and J. E. Ortega. Lateral quantum wells at vicinal Au(111) studied with angle-resolved photoemission. *Physical Review B*, 66(24):245419, 2002.

[74] H. P. Boehm, A. Clauss, G. O. Fischer, and U. Hofmann. Das Adsorptionsverhalten Sehr Dunner Kohlenstoff-Folien. *Zeitschrift Fur Anorganische Und Allgemeine Chemie*, 316(3-4):119, 1962.

[75] J. Kong, A. Reina, X. T. Jia, J. Ho, D. Nezich, H. B. Son, V. Bulovic, and M. S. Dresselhaus. Large Area, Few-Layer Graphene Films on Arbitrary Substrates by Chemical Vapor Deposition. *Nano Letters*, 9(1):30, 2009.

[76] M. Chhowalla, G. Eda, and G. Fanchini. Large-area ultrathin films of reduced graphene oxide as a transparent and flexible electronic material. *Nature Nanotechnology*, 3(5):270, 2008.

[77] D. Eom, D. Prezzi, K. T. Rim, H. Zhou, M. Lefenfeld, S. Xiao, C. Nuckolls, M. S. Hybertsen, T. F. Heinz, and G. W. Flynn. Structure and Electronic Properties of Graphene Nanoislands on Co(0001). *Nano Letters*, 9(8):2844, 2009.

[78] A. Nagashima, N. Tejima, and C. Oshima. Electronic states of the pristine and alkali-metal-intercalated monolayer graphite/ni(111) systems. *Physical Review B*, 50(23):17487–17495, 1994.

[79] A. Varykhalov, J. Sanchez-Barriga, A. M. Shikin, C. Biswas, E. Vescovo, A. Rybkin, D. Marchenko, and O. Rader. Electronic and Magnetic Properties of Quasifreestanding Graphene on Ni. *Physical Review Letters*, 101(15):157601, 2008.

[80] A. B. Preobrajenski, M. L. Ng, A. S. Vinogradov, and N. Martensson. Controlling graphene corrugation on lattice-mismatched substrates. *Physical Review B*, 78(7): 073401, 2008.

[81] E. Miniussi, M. Pozzo, A. Baraldi, E. Vesselli, R. R. Zhan, G. Comelli, T. O. Mentes, M. A. Nino, A. Locatelli, S. Lizzit, and D. Alfe. Thermal Stability of Corrugated Epitaxial Graphene Grown on Re(0001). *Physical Review Letters*, 106 (21):216101, 2011.

[82] C. Busse, P. Lazic, R. Djemour, J. Coraux, T. Gerber, N. Atodiresei, V. Caciuc, R. Brako, A. T. N'Diaye, S. Blugel, J. Zegenhagen, and T. Michely. Graphene on

Ir(111): Physisorption with Chemical Modulation. *Physical Review Letters*, 107 (3):036101, 2011.

[83] M. Kralj, I. Pletikosic, M. Petrovic, P. Pervan, M. Milun, A. T. N'Diaye, C. Busse, T. Michely, J. Fujii, and I. Vobornik. Graphene on ir(111) characterized by angle-resolved photoemission. *Physical Review B*, 84(7), 2011.

[84] P. Sutter, J. T. Sadowski, and E. Sutter. Graphene on Pt(111): Growth and substrate interaction. *Physical Review B*, 80(24):245411, 2009.

[85] Y. Murata, E. Starodub, B. B. Kappes, C. V. Ciobanu, N. C. Bartelt, K. F. McCarty, and S. Kodambaka. Orientation-dependent work function of graphene on Pd(111). *Applied Physics Letters*, 97(14):143114, 2010.

[86] A. M. Shikin, V. K. Adamchuk, and K. H. Rieder. Formation of quasi-free graphene on the ni(111) surface with intercalated cu, ag, and au layers. *Physics of the Solid State*, 51(11):2390–2400, 2009.

[87] L. Gao, J. R. Guest, and N. P. Guisinger. Epitaxial Graphene on Cu(111). *Nano Letters*, 10(9):3512, 2010.

[88] J. M. Cai, P. Ruffieux, R. Jaafar, M. Bieri, T. Braun, S. Blankenburg, M. Muoth, A. P. Seitsonen, M. Saleh, X. L. Feng, K. Mullen, and R. Fasel. Atomically precise bottom-up fabrication of graphene nanoribbons. *Nature*, 466(7305):470, 2010.

[89] B. Song, D. Li, W. P. Qi, M. Elstner, C. H. Fan, and H. P. Fang. Graphene on Au(111): A Highly Conductive Material with Excellent Adsorption Properties for High-Resolution Bio/Nanodetection and Identification. *Chemphyschem*, 11(3): 585, 2010.

[90] Y. S. Dedkov, M. Fonin, U. Rudiger, and C. Laubschat. Graphene-protected iron layer on Ni(111). *Applied Physics Letters*, 93(2):022509, 2008.

[91] L. Zhao, K. T. Rim, H. Zhou, R. He, T. F. Heinz, A. Pinczuk, G. W. Flynn, and A. N. Pasupathy. Influence of copper crystal surface on the CVD growth of large area monolayer graphene. *Solid State Communications*, 151(7):509, 2011.

[92] J. D. Wood, S. W. Schmucker, A. S. Lyons, E. Pop, and J. W. Lyding. Effects of Polycrystalline Cu Substrate on Graphene Growth by Chemical Vapor Deposition. *Nano Letters*, 11(11):4547, 2011.

[93] A. L. Walter, S. Nie, A. Bostwick, K. S. Kim, L. Moreschini, Y. J. Chang, D. Innocenti, K. Horn, K. F. McCarty, and E. Rotenberg. Electronic structure of graphene on single-crystal copper substrates. *Physical Review B*, 84(19):195443, 2011.

[94] Y. Ogawa, B. S. Hu, C. M. Orofeo, M. Tsuji, K. Ikeda, S. Mizuno, H. Hibino, and H. Ago. Domain Structure and Boundary in Single-Layer Graphene Grown on Cu(111) and Cu(100) Films. *Journal of Physical Chemistry Letters*, 3(2):219, 2012.

[95] N. R. Wilson, A. J. Marsden, M. Saghir, C. J. Bromley, R. Schaub, G. Costantini, T. W. White, C. Partridge, A. Barinov, P. Dudin, A. M. Sanchez, J. J. Mudd, M. Walker, and G. R. Bell. Weak mismatch epitaxy and structural feedback in graphene growth on copper foil. *Nano Research*, 6(2):99, 2013.

[96] J. B. Sun, J. B. Hannon, R. M. Tromp, P. Johari, A. A. Bol, V. B. Shenoy, and K. Pohl. Spatially-Resolved Structure and Electronic Properties of Graphene on Polycrystalline Ni. *Acs Nano*, 4(12):7073, 2010.

[97] S. Thiele, A. Reina, P. Healey, J. Kedzierski, P. Wyatt, P. L. Hsu, C. Keast, J. Schaefer, and J. Kong. Engineering polycrystalline Ni films to improve thickness uniformity of the chemical-vapor-deposition-grown graphene films. *Nanotechnology*, 21(1):015601, 2010.

[98] E. Sutter, P. Albrecht, and P. Sutter. Graphene growth on polycrystalline Ru thin films. *Applied Physics Letters*, 95(13):133109, 2009.

[99] M. C. Wu, Q. Xu, and D. W. Goodman. Investigations of Graphitic Overlayers Formed from Methane Decomposition on Ru(0001) and Ru(11$\bar{2}$0) Catalysts with Scanning Tunneling Microscopy and High Resolution Electron Energy Loss Spectroscopy. *Journal of Physical Chemistry*, 98(19):5104, 1994.

[100] D. Martoccia, P. R. Willmott, T. Brugger, M. Bjorck, S. Gunther, C. M. Schleputz, A. Cervellino, S. A. Pauli, B. D. Patterson, S. Marchini, J. Wintterlin, W. Moritz, and T. Greber. Graphene on Ru(0001): A 25x25 supercell. *Physical Review Letters*, 101(12):126102, 2008.

[101] Y. Cui, Q. Fu, H. Zhang, D. L. Tan, and X. H. Bao. Dynamic Characterization of Graphene Growth and Etching by Oxygen on Ru(0001) by Photoemission Electron Microscopy. *Journal of Physical Chemistry C*, 113(47):20365, 2009.

[102] E. Sutter, D. P. Acharya, J. T. Sadowski, and P. Sutter. Scanning tunneling microscopy on epitaxial bilayer graphene on ruthenium (0001). *Applied Physics Letters*, 94(13):133101, 2009.

[103] S. J. Altenburg, J. Kroger, B. Wang, M. L. Bocquet, N. Lorente, and R. Berndt. Graphene on Ru(0001): Contact Formation and Chemical Reactivity on the Atomic Scale. *Physical Review Letters*, 105(23):236101, 2010.

[104] B. Borca, S. Barja, M. Garnica, J. J. Hinarejos, A. L. V. de Parga, R. Miranda, and F. Guinea. Periodically modulated geometric and electronic structure of graphene on Ru(0001). *Semiconductor Science and Technology*, 25(3):034001, 2010.

[105] B. Borca, S. Barja, M. Garnica, M. Minniti, A. Politano, J. M. Rodriguez-Garcia, J. J. Hinarejos, D. Farias, A. L. V. de Parga, and R. Miranda. Electronic and geometric corrugation of periodically rippled, self-nanostructured graphene epitaxially grown on Ru(0001). *New Journal of Physics*, 12:093018, 2010.

[106] D. Martoccia, M. Bjorck, C. M. Schleputz, T. Brugger, S. A. Pauli, B. D. Patterson, T. Greber, and P. R. Willmott. Graphene on Ru(0001): a corrugated and chiral structure. *New Journal of Physics*, 12:043028, 2010.

[107] W. Feng, S. L. Lei, Q. X. Li, and A. D. Zhao. Periodically Modulated Electronic Properties of the Epitaxial Monolayer Graphene on Ru(0001). *Journal of Physical Chemistry C*, 115(50):24858, 2011.

[108] S. Gunther, S. Danhardt, B. Wang, M. L. Bocquet, S. Schmitt, and J. Wintterlin. Single Terrace Growth of Graphene on a Metal Surface. *Nano Letters*, 11(5):1895, 2011.

[109] M. Gyamfi, T. Eelbo, M. Wasniowska, and R. Wiesendanger. Inhomogeneous electronic properties of monolayer graphene on Ru(0001). *Physical Review B*, 83 (15):153418, 2011.

[110] B. Wang, M. L. Bocquet, S. Marchini, S. Gunther, and J. Wintterlin. Chemical origin of a graphene moire overlayer on Ru(0001). *Physical Chemistry Chemical Physics*, 10(24):3530, 2008.

[111] B. Wang, S. Gunther, J. Wintterlin, and M. L. Bocquet. Periodicity, work function and reactivity of graphene on Ru(0001) from first principles. *New Journal of Physics*, 12:043041, 2010.

[112] W. Moritz, B. Wang, M. L. Bocquet, T. Brugger, T. Greber, J. Wintterlin, and S. Gunther. Structure Determination of the Coincidence Phase of Graphene on Ru(0001). *Physical Review Letters*, 104(13):136102, 2010.

[113] D. Stradi, S. Barja, C. Diaz, M. Garnica, B. Borca, J. J. Hinarejos, D. Sanchez-Portal, M. Alcami, A. Arnau, A. L. V. de Parga, R. Miranda, and F. Martin. Role of Dispersion Forces in the Structure of Graphene Monolayers on Ru Surfaces. *Physical Review Letters*, 106(18):186102, 2011.

[114] D. Stradi, S. Barja, C. Diaz, M. Garnica, B. Borca, J. J. Hinarejos, D. Sanchez-Portal, M. Alcami, A. Arnau, A. L. V. de Parga, R. Miranda, and F. Martin.

Electron localization in epitaxial graphene on Ru(0001) determined by moire corrugation. *Physical Review B*, 85(12):121404(R), 2012.

[115] A. H. Castro Neto, F. Guinea, N. M. R. Peres, K. S. Novoselov, and A. K. Geim. The electronic properties of graphene. *Reviews of Modern Physics*, 81(1):109, 2009.

[116] M. Wiessner, N. S. R. Lastra, J. Ziroff, F. Forster, P. Puschnig, L. Dossel, K. Mullen, A. Scholl, and F. Reinert. Different views on the electronic structure of nanoscale graphene: aromatic molecule versus quantum dot. *New Journal of Physics*, 14:113008, 2012.

[117] C. Enderlein, Y. S. Kim, A. Bostwick, E. Rotenberg, and K. Horn. The formation of an energy gap in graphene on ruthenium by controlling the interface. *New Journal of Physics*, 12:033014, 2010.

[118] T. Brugger, S. Gunther, B. Wang, J. H. Dil, M. L. Bocquet, J. Osterwalder, J. Wintterlin, and T. Greber. Comparison of electronic structure and template function of single-layer graphene and a hexagonal boron nitride nanomesh on Ru(0001). *Physical Review B*, 79(4):045407, 2009.

[119] D. E. Jiang, M. H. Du, and S. Dai. First principles study of the graphene/Ru(0001) interface. *Journal of Chemical Physics*, 130(7):074705, 2009.

[120] C. Ludwig, R. Strohmaier, J. Petersen, B. Gompf, and W. Eisenmenger. Epitaxy and Scanning-Tunneling-Microscopy Image-Contrast of Copper Phthalocyanine on Graphite and Mos2. *Journal of Vacuum Science & Technology B*, 12(3):1963, 1994.

[121] V. Petracek. Observation of Cu-Phthalocyanine Single Molecules and Islands Deposited on Gold and Highly-Oriented Pyrolytic-Graphite Substrates. *International Journal of Electronics*, 78(2):267, 1995.

[122] L. Ottaviano, S. DiNardo, L. Lozzi, M. Passacantando, P. Picozzi, and S. Santucci. Thin and ultra-thin films of nickel phthalocyanine grown on highly oriented pyrolitic graphite: An XPS, UHV-AFM and air tapping-mode AFM study. *Surface Science*, 373(2-3):318, 1997.

[123] S. Kera, A. Abduaini, M. Aoki, K. Okudaira, N. Ueno, Y. Harada, Y. Shirota, and T. Tsuzuki. Characterization of ultrathin films of titanyl phthalocyanine on graphite: PIES and UPS study. *Thin Solid Films*, 327-329:278, 1998.

[124] K. Walzer and M. Hietschold. STM and STS investigation of ultrathin tin phthalocyanine layers adsorbed on HOPG(0001) and Au(111). *Surface Science*, 471 (1-3):1, 2001.

[125] S. Kera, H. Yamane, I. Sakuragi, K. K. Okudaira, and N. Ueno. Very narrow photoemission bandwidth of the highest occupied state in a copper-phthalocyanine monolayer. *Chemical Physics Letters*, 364(1-2):93, 2002.

[126] S. D. Wang, X. Dong, C. S. Lee, and S. T. Lee. Orderly growth of copper phthalocyanine on highly oriented pyrolytic graphite (HOPG) at high substrate temperatures. *Journal of Physical Chemistry B*, 108(5):1529, 2004.

[127] S. Kera, H. Fukagawa, T. Kataoka, S. Hosoumi, H. Yamane, and N. Ueno. Spectroscopic evidence of strong π - π interorbital interaction in a lead-phthalocyanine bilayer film attributed to the dimer nanostructure. *Physical Review B*, 75:121305, 2007.

[128] T. Kataoka, H. Fukagawa, S. Hosoumi, K. Nebashi, K. Sakamoto, and N. Ueno. Observation of a temperature-dependent transition of a copper-phthalocyanine thin film adsorbed on HOPG. *Chemical Physics Letters*, 451(1-3):43, 2008.

[129] K. Nilson, J. Ahlund, B. Brena, E. Gothelid, J. Schiessling, N. Martensson, and C. Puglia. Scanning tunneling microscopy study of metal-free phthalocyanine monolayer structures on graphite. *Journal of Chemical Physics*, 127(11):114702, 2007.

[130] Y. L. Huang, H. Li, J. Ma, H. Huang, W. Chen, and A. T. S. Wee. Scanning Tunneling Microscopy Investigation of Self-Assembled CuPc/F_{16}CUPc Binary Superstructures on Graphite. *Langmuir*, 26(5):3329, 2010.

[131] T. C. Niu, Y. L. Huang, J. T. Sun, S. Kera, N. Ueno, A. T. S. Wee, and W. Chen. Tunable two-dimensional molecular dipole dot arrays on graphite. *Applied Physics Letters*, 99(14):143114, 2011.

[132] M. Scheffler, L. Smykalla, D. Baumann, R. Schlegel, T. Hanke, M. Toader, B. Buchner, M. Hietschold, and C. Hess. Structural study of monolayer cobalt phthalocyanine adsorbed on graphite. *Surface Science*, 608:55, 2013.

[133] S. K. Hamalainen, M. Stepanova, R. Drost, P. Liljeroth, J. Lahtinen, and J. Sainio. Self-Assembly of Cobalt-Phthalocyanine Molecules on Epitaxial Graphene on Ir(111). *Journal of Physical Chemistry C*, 116(38):20433, 2012.

[134] K. Yang, W. D. Xiao, Y. H. Jiang, H. G. Zhang, L. W. Liu, J. H. Mao, H. T. Zhou, S. X. Du, and H. J. Gao. Molecule-Substrate Coupling between Metal Phthalocyanines and Epitaxial Graphene Grown on Ru(0001) and Pt(111). *Journal of Physical Chemistry C*, 116(26):14052, 2012.

[135] H. G. Zhang, W. D. Xiao, J. H. Mao, H. T. Zhou, G. Li, Y. Zhang, L. W. Liu, S. X. Du, and H. J. Gao. Host-Guest Superstructures on Graphene-Based Kagome Lattice. *Journal of Physical Chemistry C*, 116(20):11091, 2012.

[136] W. D. Dou, Q. D. Yang, and C. S. Lee. Anisotropic film growth of iron-phthalocyanine on graphene on a Ni(111) substrate: Roles of molecule-substrate and intermolecular interaction. *Applied Physics Letters*, 102(13):131606, 2013.

[137] M. Scardamaglia, G. Forte, S. Lizzit, A. Baraldi, P. Lacovig, R. Larciprete, C. Mariani, and M. G. Betti. Metal-phthalocyanine array on the moir, pattern of a graphene sheet . *Journal of Nanoparticle Research*, 13(11):6013, 2011.

[138] M. Scardamaglia, S. Lisi, S. Lizzit, A. Baraldi, R. Larciprete, C. Mariani, and M. G. Betti. Graphene-Induced Substrate Decoupling and Ideal Doping of a Self-Assembled Iron-phthalocyanine Single Layer. *Journal of Physical Chemistry C*, 117(6):3019, 2013.

[139] K. Xiao, W. Deng, J. K. Keum, M. Yoon, I. V. Vlassiouk, K. W. Clark, A. P. Li, I. I. Kravchenko, G. Gu, E. A. Payzant, B. G. Sumpter, S. C. Smith, J. F. Browning, and D. B. Geohegan. Surface-Induced Orientation Control of CuPc Molecules for the Epitaxial Growth of Highly Ordered Organic Crystals on Graphene. *Journal of the American Chemical Society*, 135(9):3680, 2013.

[140] S. Zhong, J. Q. Zhong, H. Y. Mao, R. Wang, Y. Wang, D. C. Qi, K. P. Loh, A. T. S. Wee, Z. K. Chen, and W. Chen. CVD Graphene as Interfacial Layer to Engineer the Organic Donor Acceptor Heterojunction Interface Properties. *Acs Applied Materials & Interfaces*, 4(6):3134, 2012.

[141] S.T. Lee Qi-Hui Wu, Guo Hong. Modification of CuPc/graphene interfacial electronic structure. *Organic Electronics*, 14(2):542, 2013.

[142] P. Sutter, M. S. Hybertsen, J. T. Sadowski, and E. Sutter. Electronic Structure of Few-Layer Epitaxial Graphene on Ru(0001). *Nano Letters*, 9(7):2654, 2009.

[143] Patrick Bayersdorfer. *Spot-Plotter software*, 2008.

[144] S. Tougaard. *QUASES, Software package for quantitative XPS/AES of surface nanostructures by inelasticpeak shape analysis*, 1994-2014.

[145] T. Graber, F. Forster, A. Scholl, and F. Reinert. Experimental determination of the attenuation length of electrons in organic molecular solids: The example of PTCDA. *Surface Science*, 605(9-10):878, 2011.

[146] John Venables. *Introduction to surface and thin film processes.* Cambridge University Press, Cambrige, UK ; New York, 2000.

[147] S. Kera, M. B. Casu, K. R. Bauchspiess, D. Batchelor, T. Schmidt, and E. Umbach. Growth mode and molecular orientation of phthalocyanine molecules on metal single crystal substrates: A NEXAFS and XPS study. *Surface Science*, 600(5): 1077, 2006.

[148] S. Tougaard. Quantitative-Analysis of the Inelastic Background in Surface Electron-Spectroscopy. *Surface and Interface Analysis*, 11:453, 1988.

[149] S. Tougaard and S. Hansen, H. Non-Destructive Depth Profiling through Quantitative-Analysis of Surface Electron-Spectra. *Surface and Interface Analysis*, 14:730, 1989.

[150] S. Tougaard. Accuracy of the non-destructive surface nanostructure quantification technique based on analysis of the XPS or AES peak shape. *Surface and Interface Analysis*, 26:249, 1998.

[151] M. Toader, P. Shukrynau, M. Knupfer, D. R. T. Zahn, and M. Hietschold. Site-Dependent Donation/Backdonation Charge Transfer at the CoPc/Ag(111) Interface. *Langmuir*, 28(37):13325, 2012.

[152] K. T. Park, A. Miller, K. Klier, R. L. Opila, and J. E. Rowe. Heteroepitaxial copper phthalocyanine on Au(001) studied by high-resolution X-ray photoelectron spectroscopy. *Surface Science*, 529(3):L285, 2003.

[153] F. Evangelista, V. Carravetta, G. Stefani, B. Jansik, M. Alagia, S. Stranges, and A. Ruocco. Electronic structure of copper phthalocyanine: An experimental and theoretical study of occupied and unoccupied levels. *Journal of Chemical Physics*, 126(12):124709, 2007.

[154] S. Kera, H. Yamane, and N. Ueno. First-principles measurements of charge mobility in organic semiconductors: Valence hole vibration coupling in organic ultrathin films. *Progress in Surface Science*, 84:135, 2009.

[155] M. Haming, C. Scheuermann, A. Scholl, F. Reinert, and E. Umbach. Coverage dependent organic-metal interaction studied by high-resolution core level spectroscopy: SnPc (sub)monolayers on Ag(111). *Journal of Electron Spectroscopy and Related Phenomena*, 174(1-3):59, 2009.

[156] M. Haming, M. Greif, M. Wiessner, A. Scholl, and F. Reinert. Characterization of ultra-thin organic hetero-interfaces - SnPc/PTCDA/Ag(111). *Surface Science*, 604(19-20):1619, 2010.

[157] H. Karacuban, M. Lange, J. Schaffert, O. Weingart, T. Wagner, and R. Moller. Substrate-induced symmetry reduction of CuPc on Cu(111): An LT-STM study. *Surface Science*, 603(5):L39, 2009.

[158] S. X. Yin, C. Wang, B. Xu, and C. L. Bai. Studies of CuPc adsorption on graphite surface and alkane adlayer. *Journal of Physical Chemistry B*, 106(35):9044, 2002.

[159] M. Wiessner, J. Ziroff, F. Forster, M. Arita, K. Shimada, P. Puschnig, A. Scholl, and F. Reinert. Substrate-mediated band-dispersion of adsorbate molecular states. *Nature Communications*, 4, 2013.

[160] M. Wiessner, J. Kubert, V. Feyer, P. Puschnig, A. Scholl, and F. Reinert. Lateral band formation and hybridization in molecular monolayers: Ntcda on ag(110) and cu(100). *Physical Review B*, 88(7), 2013.

[161] B. Stadtmuller, I. Kroger, F. Reinert, and C. Kumpf. Submonolayer growth of CuPc on noble metal surfaces. *Physical Review B*, 83(8):085416, 2011.

[162] P. A. Khomyakov, G. Giovannetti, P. C. Rusu, G. Brocks, J. van den Brink, and P. J. Kelly. First-principles study of the interaction and charge transfer between graphene and metals. *Physical Review B*, 79(19):195425, 2009.

[163] M. Vanin, J. J. Mortensen, A. K. Kelkkanen, J. M. Garcia-Lastra, K. S. Thygesen, and K. W. Jacobsen. Graphene on metals: A van der Waals density functional study. *Physical Review B*, 81(8):081408(R), 2010.

[164] R. Brako, D. Sokcevic, P. Lazic, and N. Atodiresei. Graphene on the ir(111) surface: from van der waals to strong bonding. *New Journal of Physics*, 12, 2010.

[165] A. Ruban, B. Hammer, P. Stoltze, H. L. Skriver, and J. K. Norskov. Surface electronic structure and reactivity of transition and noble metals. *Journal of Molecular Catalysis a-Chemical*, 115(3):421, 1997.

[166] B. Cordero, V. Gomez, A. E. Platero-Prats, M. Reves, J. Echeverria, E. Cremades, F. Barragan, and S. Alvarez. Covalent radii revisited. *Dalton Transactions*, 21 (21):2832, 2008.

[167] S. M. Kozlov, F. Vines, and A. Gorling. Bonding Mechanisms of Graphene on Metal Surfaces. *Journal of Physical Chemistry C*, 116(13):7360, 2012.

[168] F. Mittendorfer, A. Garhofer, J. Redinger, J. Klimes, J. Harl, and G. Kresse. Graphene on Ni(111): Strong interaction and weak adsorption. *Physical Review B*, 84(20):201401(R), 2011.

[169] B. Hammer, Y. Morikawa, and J. K. Norskov. CO chemisorption at metal surfaces and overlayers. *Physical Review Letters*, 76(12):2141, 1996.

[170] M. Mavrikakis, B. Hammer, and J. K. Norskov. Effect of strain on the reactivity of metal surfaces. *Physical Review Letters*, 81(13):2819, 1998.

[171] J. J. Cox, S. M. Bayliss, and T. S. Jones. Ordered copper phthalocyanine overlayers on InAs and InSb(100) surfaces. *Surface Science*, 433:152, 1999.

[172] F. Schwierz. Graphene Transistors: Status, Prospects, and Problems. *Proceedings of the Ieee*, 101(7):1567, 2013.

List of Figures

Publication

1. Daniel Lüftner, Matus Milko, Sophia Huppmann, Markus Scholz, **N. Nguyen**, Michael Wießner, Achim Schöll, Friedrich Reinert and Peter Puschnig, CuPc-/Au(110): Determination of the azimuthal alignment by combination of a angle-resolved photoemission and density functional theory, *Journal of Electron Spectroscopy and Related Phenomena*, 195, 293–300 (2014).

2. **N. Nguyen**, M. Mulazzi, F. Reinert, Electronic structure and Fermi surface of Ru(0001) and Ru($10\bar{1}0$) measured with high resolution angle-resolved photoemission spectroscopy, *Journal of Electron Spectroscopy and Related Phenomena*, 191, 27–34 (2013)

3. M. Scholz, C. Sauer, M. Wießner, **N. Nguyen**, A. Schöll, F. Reinert, Structure formation in organic thin films observed in real time by energy dispersive near-edge x-ray absorption fine-structure spectroscopy, *New J Phys*, 15 (2013).

4. **N. Nguyen**, W. Lu, and T. Suzuki, Temperature Dependence of Magnetic Properties in Epitaxial FePt/FeRh Bilayer, *IEEE T Magn* 45 (6), 2531–2533 (2009).

5. **N. Nguyen**, W. Lu, and T. Suzuki, Exchange bias of ferromagnetic/antiferromagnetic in FePt/FeRh bilayers, *J Appl Phys* 105 (7), 07D708 (2009).

6. W. Lu, **N. Nguyen**, and T. Suzuki, Effect of Pt Doping on the Structure, Magnetic, and Magneto-Optical Properties of Ordered FeRh-Pt Thin Films, *IEEE T Magn* 45 (6), 2716–2719 (2009).

7. W. Lu, **N. Nguyen**, and T. Suzuki, First-order magnetic phase transition in FeRh-Pt thin films, *J Appl Phys* 105 (7), 07A904 (2009).

8. W. Lu, **N. Nguyen**, and T. Suzuki, Magnetic Properties and Phase Transition Kinetics of Fe-50($Rh_{1-X}Pt_X$)(50) Thin Films, *IEEE T Magn* 45 (10), 4011–4014 (2009).

9. H. Y. Y. Ko, T. Suzuki, **N. Nguyen**, N. N. Phuoc, J. Cao, and Y. Hirotsu, Magnetic and structural characterizations on nanoparticles of FePt, FeRh and their composites, *J Magn Magn Mater* 320 (22), 3120–3123 (2008).

10. H. Y. Y. Ko, S. Inoue, **N. Nguyen**, T. Suzuki, and Y. Hirotsu, Magnetic Properties of Nanocomposite Particles of FePt/FeRh, *IEEE T Magn* 44 (11), 2780–2783 (2008).

11. S. Inoue, **N. Nguyen**, N. N. Phuoc, J. Cao, H. Y. Y. Ko, and T. Suzuki, Magnetic and magneto-optical properties of FeRh thin films, *J Magn Magn Mater* 320 (22), 3113–3116 (2008).

12. S. Inoue, N. N. Phuoc, J. Cao, **N. Nguyen**, H. Y. Y. Ko, and T. Suzuki, Structural and magneto-optical properties of FeRh thin films, *J Appl Phys* 103 (7), 07B312 (2008).

13. J. W. Cao, **N. Nguyen**, S. Inoue, H. Y. Y. Ko, N. N. Phuoc, and T. Suzuki, Magnetization behaviors for FeRh single crystal thin films, *J Appl Phys* 103 (7), 07F501 (2008).

14. **N. Nguyen**, NP Thuy, NA Tuan, NN Phuoc, T Suzuki "Giant parallel and perpendicular exchange biases in MnPd/Co bilayers" , phys. stat. sol. (c)., 4, 4384 (2007).

15. **N. Nguyen**, N. P. Thuy, N. A. Tuan, N. N. Phuoc, and T. Suzuki, Giant exchange bias in MnPd/Co bilayers, *J Magn Magn Mater* 315 (2), 82-88 (2007).

16. N. P. Thuy, N. A. Tuan, N. N. Phuoc, **N. Nguyen**, T. D. Hien, and N. H. Hai, The exchange bias in MnPd/$Co_{1-X}Fe_X$ bilayers, *J Magn Magn Mater* 304 (1), 41–45 (2006).

17. N. N. Phuoc, N. P. Thuy, N. A. Tuan, L. T. Hung, N. T. Thanh, and **N. Nguyen**, Coexistence of positive and negative exchange bias in CrMn/Co bilayers, *J Magn Magn Mater* 298 (1), 43–47 (2006).

Acknowledgements

I wish to express most sincerely my gratitude to Prof. Dr. Friedrich Theodor Reinert at Physikalisches Institut, Experimentelle Physik VII, Universität Würzburg, for giving me a chance to receive the Marie Curie fellowship from EU-FP7 and to study in his group. During my Ph.D research, with his opened mind, I have an opportunity to work in multidimensional areas without limited boundary. Like electrons in the surface state of metal surfaces, I have a lot of freedoms for creativity and getting the best results which I can get.

My sincere thanks go to Dr. Takao Suzuki, who was a principal professor and Vice president at the Toyota Technological Institute in Nagoya, Japan for taking me as a member of ISML (**I**nformation **S**torage **M**ataerials **L**aboratory or **I**ntellectually **S**ignificant **M**eaningful **L**ife as he said) from 2006 to 2009. Dr. Takao Suzuki always told me that "Do your best! hard-working is a key of success. You don't know what will happen to you in near future, so don't waste yours time". I still remember he always came to the lab at 3:00 AM. It was the really great opportunity for me to work with him.

I would like to thank Dr. Mattia Mulazzi for unlimited time discussion and for his passion to answer a lot of my basic and stupid questions. Also another very special thanks for his long time calculation to support my experimental data. I gratefully acknowledges PD. Dr. Achim Schöll for valuable discussions and suggestions. He always opens the office door and gives me the time to discuss even though he is very busy.

The financial support from the European Community Seventh Framework Programme [FP7 (2007-2013)] under grant agreement n. 215723 is gratefully acknowledged. I also would like to thank especially Dirk Ehm, Maarten van Kampen and Gerold Alberga for the discussions during the S.P.A.M project meeting. I am thankful to my S.P.A.M project-mates, Deniz, Andrea, Bartosz, Vadim, German, Fernando, Arzu, Sidharam and Sedat to show me how people coming from different domains can work together in one project.

Special thanks to all members in Experimentelle Physik VII, Universität Würzburg. Hiltrud Eaton and Lieselotte Reichert, our group's secretaries, helped me to get through German documents. Marius Ernst and Sina Gusenleitner worked with me in the same S.P.A.M project but in two opposite ways (I am still hope that we can come up something at the end of our journey in the S.P.A.M project as we said in our motivation). Sina always made my travel conference become easy and enjoyable. Holger Wetzstein, my first office-mate, who showed me everything, helped me a lot and tried to convince me to use Linux instead of Windows system. Johannes Ziroff helped me when I just

came to Würzburg and shown me that there are a lot of ways electrons can travel from bulk to surfaces. Tina Graber, the first people taught me the basic XPS and UPS when I do not know anything about photoemission. Hendrik Bentmann, Christoph Seibel, Nuber Andreas and Holger Schwab helped me to measure APRES in the R4000 chamber. Holger Schwab also taught me how to make balloon from liquid helium. Michael Wießner built the SPECS chamber and gave it to me, so I had a chamber to finish my Ph.D. Sophia Huppmann shared the most effective time with me to do experiment in the SPECS chamber. Olivier Copie always told me to focus on writing paper. Lothar Weinhardt, the first people I always met in early morning. Frank Forster always remained me, we all still are student. Dirk Hauschild and Sebastian Fiedler kept the group in a green environment and the way entropy is maximum. Christoph Sauer showed that all electrons are different even though they have same energy level. Patrick Bayersdorfer had long discussion about Ph.D life. Henriette Maass, Peter Lutz, Frank Meyer, Andreas Benkert and Chul Hee Min always had a big smile.

Very special thanks go to Markus Scholz, who welcomed in all aspects, shared the most difficulty time when we started writing the thesis and helped me a lot to finish my Ph.D. I am really grateful for all the time he had for me and helping me to check and made comments to my thesis.

Finally a couple words to my family:
Con cảm ơn bố mẹ đã luôn ủng hộ con, luôn luôn tin tưởng vào khả năng của con, và để con làm những điều con thích. Đấy là bài học lớn nhất con học được từ bố mẹ. Sau này con sẽ dạy con của con theo như cách bố mẹ đã dạy con. Em cảm ơn chị Liên, em Sơn đã giúp đỡ và quan tâm bất kể thời gian nào. Cuối cùng anh xin cảm ơn người vợ tuyệt vời cùng với hai đứa con đã thông cảm và hiểu về công việc của chồng.

Eidesstattliche Erklärung

gemäß - 5, Abs. 2, Satz 2, 3, 4 und 6 der
Promotionsordnung der
Fakultät für Physik und Astronomie der
Julius-Maximilians-Universität Würzburg

Hiermit erkläre ich an Eides statt, dass ich die vorliegende Dissertation eigenständig, d.h. insbesondere selbstständig und ohne Hilfe einer kommerziellen Promotionsberatung angefertigt und keine anderen als die von mir angegebenen Quellen und Hilfsmittel benutzt habe und dass ich die Gelegenheit zum Promotionsvorhaben nicht kommerziell vermittelt bekommen habe und insbesondere nicht eine Person oder Organisation eingeschaltet habe, die gegen Entgelt Betreuer bzw. Betreuerinnen für die Anfertigung von Dissertationen sucht.

Hiermit erkläre ich zudem, dass ich die Regeln der Universität Würzburg über gute wissenschaftliche Praxis eingehalten habe und dass ich die Dissertation in gleicher oder anderer Form nicht bereits in einem anderen Prüfungsfach vorgelegt habe.

Würzburg, den 28. Februar 2015

Thanh Nam NGUYEN